N°d'ordre NNT : 2016LYSEI043

THESE de DOCTORAT **DE L'UNIVERSITE DE LYON**
préparée au sein de
l'**INSA** LYON

Ecole Doctorale N° ED162
(MECANIQUE, ENERGETIQUE, GENIE CIVIL, ACOUSTIQUE)

Spécialité de doctorat :
Discipline : Mécanique -Génie Mécanique - Génie Civil

Soutenue publiquement par :
Lan YAO

Experimental and Numerical Study of Dynamic Crack Propagation in Ice under Impact Loading

---

Devant le jury composé de :

NELIAS Daniel	Professeur des Universités	INSA LYON	Directeur de thèse
MAIGRE Hubert	Chargé de recherche	CNRS	Examinateur
ZHAO Han	Professeur des Universités	LMT	Rapporteur
MONTAGNAT Maurine	Chargé de recherche	CNRS	Rapporteur
DELETOMBE Eric	Maître de Recherche	ONERA	Examinateur
COMBESCURE Alain	Professeur des Universités	INSA LYON	Président

Département FEDORA – INSA Lyon - Ecoles Doctorales – Quinquennal 2016-2020

SIGLE	ECOLE DOCTORALE	NOM ET COORDONNEES DU RESPONSABLE
CHIMIE	**CHIMIE DE LYON** **http://www.edchimie-lyon.fr** Sec : Renée EL MELHEM Bat Blaise Pascal 3e etage secretariat@edchimie-lyon.fr Insa : R. GOURDON	M. Stéphane DANIELE Institut de Recherches sur la Catalyse et l'Environnement de Lyon IRCELYON-UMR 5256 Équipe CDFA 2 avenue Albert Einstein 69626 Villeurbanne cedex directeur@edchimie-lyon.fr
E.E.A.	**ELECTRONIQUE, ELECTROTECHNIQUE, AUTOMATIQUE** **http://edeea.ec-lyon.fr** Sec : M.C. HAVGOUDOUKIAN Ecole-Doctorale.eea@ec-lyon.fr	M. Gérard SCORLETTI Ecole Centrale de Lyon 36 avenue Guy de Collongue 69134 ECULLY Tél : 04.72.18 60.97 Fax : 04 78 43 37 17 Gerard.scorletti@ec-lyon.fr
E2M2	**EVOLUTION, ECOSYSTEME, MICROBIOLOGIE, MODELISATION** **http://e2m2.universite-lyon.fr** Sec : Safia AIT CHALAL Bat Darwin - UCB Lyon 1 04.72.43.28.91 Insa : H. CHARLES Safia.ait-chalal@univ-lyon1.fr	Mme Gudrun BORNETTE CNRS UMR 5023 LEHNA Université Claude Bernard Lyon 1 Bât Forel 43 bd du 11 novembre 1918 69622 VILLEURBANNE Cédex Tél : 06.07.53.89.13 e2m2@ univ-lyon1.fr
EDISS	**INTERDISCIPLINAIRE SCIENCES-SANTE** **http://www.ediss-lyon.fr** Sec : Safia AIT CHALAL Hôpital Louis Pradel - Bron 04 72 68 49 09 Insa : M. LAGARDE Safia.ait-chalal@univ-lyon1.fr	Mme Emmanuelle CANET-SOULAS INSERM U1060, CarMeN lab, Univ. Lyon 1 Bâtiment IMBL 11 avenue Jean Capelle INSA de Lyon 696621 Villeurbanne Tél : 04.72.68.49.09 Fax :04 72 68 49 16 Emmanuelle.canet@univ-lyon1.fr
INFOMATHS	**INFORMATIQUE ET MATHEMATIQUES** **http://infomaths.univ-lyon1.fr** Sec :Renée EL MELHEM Bat Blaise Pascal 3e etage infomaths@univ-lyon1.fr	Mme Sylvie CALABRETTO LIRIS – INSA de Lyon Bat Blaise Pascal 7 avenue Jean Capelle 69622 VILLEURBANNE Cedex Tél : 04.72. 43. 80. 46 Fax 04 72 43 16 87 Sylvie.calabretto@insa-lyon.fr
Matériaux	**MATERIAUX DE LYON** **http://ed34.universite-lyon.fr** Sec : M. LABOUNE PM : 71.70 –Fax : 87.12 Bat. Saint Exupéry Ed.materiaux@insa-lyon.fr	M. Jean-Yves BUFFIERE INSA de Lyon MATEIS Bâtiment Saint Exupéry 7 avenue Jean Capelle 69621 VILLEURBANNE Cedex Tél : 04.72.43 71.70 Fax 04 72 43 85 28 Ed.materiaux@insa-lyon.fr
MEGA	**MECANIQUE, ENERGETIQUE, GENIE CIVIL, ACOUSTIQUE** **http://mega.universite-lyon.fr** Sec : M. LABOUNE PM : 71.70 –Fax : 87.12 Bat. Saint Exupéry mega@insa-lyon.fr	M. Philippe BOISSE INSA de Lyon Laboratoire LAMCOS Bâtiment Jacquard 25 bis avenue Jean Capelle 69621 VILLEURBANNE Cedex Tél : 04.72 .43.71.70 Fax : 04 72 43 72 37 Philippe.boisse@insa-lyon.fr
ScSo	**ScSo*** **http://recherche.univ-lyon2.fr/scso/** Sec : Viviane POLSINELLI Brigitte DUBOIS Insa : J.Y. TOUSSAINT viviane.polsinelli@univ-lyon2.fr	Mme Isabelle VON BUELTZINGLOEWEN Université Lyon 2 86 rue Pasteur 69365 LYON Cedex 07 Tél : 04.78.77.23.86 Fax : 04.37.28.04.48

*ScSo : Histoire, Géographie, Aménagement, Urbanisme, Archéologie, Science politique, Sociologie, Anthropologie

Acknowledgment/Remerciements

Pursuing a Ph. D likes walking in the desert. You do not know how far you have come and where you are going although you have the destination in the beginning. But in this journey, I am not alone, many people inspired, helped and accompanied me. Before I finish my thesis, I am delighted to give my heartfelt acknowledgements.

First of all, I acknowledge the help, support and guidance of my supervisor, NELIAS Daniel, with the utmost gratitude. I appreciate that he gave me the opportunity to study in LaMCoS as a Ph.D student. It's a new world for me. Living in a different culture, studying with knowledgeable teachers, working with excellent colleagues, all of these, make me different.

Meanwhile, I am grateful to my co-supervisor MAIGRE Hubert. He taught me the knowledge on fracture mechanics and shared his experiences on SHPB experiments. Most of all, I want to thank him for persistent supporting me. Thanks to his guidance, encouragement and patience, when I failed in experiments, made no progress in simulations, I never give it up. Without his help, I couldn't finish my thesis.

Appreciation should be also going to CHAUDET Philippe, GUILHERMOND Jean-Pascal, VALVERDE Paul for their help on my experimental studies such as specimen machinery, apparatus installation.

I appreciate the support from my colleagues. ROUX Louis and LION Nicolas exchanged the SHPB experimental experience to me. HABOUSSA David, CHEMIN Alexandre and JAN Yannic shared the knowledge of the software EUROPLEXUSE with me. The discussion with ZHAO Lv about the problem on dynamic fracture mechanics inspired me.

I also appreciate LACROIX Samy, BOUCLLIER Robin, ZHANG Yancheng, XIE Jing, ROUX Clément, AZEGGAGH Nacer, LU Ye, ZHU Wenqi, FEKAK Fatima-Ezzahra etc. I spent joyful days with them in LaMCoS.

I acknowledge the financial support provided by China Scholarship Council (CSC).

I am eternally indebted to my parents for their infinite love since I was born. And I am also indebted to my husband, for his company and support.

Abstract

The phenomena relating to the fracture behaviour of ice under impact loading are common in civil engineering, for offshore structures, and de-ice processes. To reduce the damage caused by ice impact and to optimize the design of structures or machines, the investigation on the dynamic fracture behaviour of ice under impact loading is needed.

This work focuses on the dynamic crack propagation in ice under impact loading. A series of impact experiments is conducted with the Split Hopkinson Pressure Bar. The temperature is controlled by a cooling chamber. The dynamic process of the ice fracture is recorded with a high speed camera and then analysed by image methods. The extended finite element method is complementary to evaluate dynamic fracture toughness at the onset and during the propagation.

The dynamic behaviour of ice under impact loading is firstly investigated with cylindrical specimen in order to obtain the dynamic stress-strain relation which will be used in later simulation.

We observed multiple cracks in the experiments on the cylindrical specimens but their study is too complicated. To better understand the crack propagation in ice, a rectangular specimen with a pre-crack is employed. By controlling the impact velocity, the specimen fractures with a main crack starting from the pre-crack. The crack propagation history and velocity are evaluated by image analysis based on grey-scale and digital image correlation. The main crack propagation velocity is identified in the range of $534 \pm 83 m/s$. It slightly varies during the propagation, first increases and keeps constant and then decreases.

The experimentally obtained parameters, such as impact velocity and crack propagation velocity, are used for simulations with the extended finite element method. The dynamic crack initiation toughness and dynamic crack growth toughness are determined when the simulation fits the experiments. The results indicate that the dynamic crack growth toughness is linearly associated with crack propagation velocity and seems temperature independent in the range $-15 \sim -1^{\circ}$C.

KEYWORDS: crack propagation, dynamic stress intensity factor, ice, split Hopkinson pressure bar, extended finite element method

Résumé

Les phénomènes liés au comportement à la rupture de la glace sous impact sont fréquents dans le génie civil, pour les structures offshore, et les processus de dégivrage. Pour réduire les dommages causés par l'impact de la glace et optimiser la conception des structures ou des machines, l'étude sur le comportement à la rupture dynamique de la glace sous impact est nécessaire.

Ces travaux de thèse portent donc sur la propagation dynamique des fissures dans la glace sous impact. Une série d'expériences d'impact est réalisée avec un dispositif de barres de Hopkinson. La température est contrôlée par une chambre de refroidissement. Le processus dynamique de la rupture de la glace est enregistré avec une caméra à grande vitesse et ensuite analysé par des méthodes d'analyse d'images. La méthode des éléments finis étendus complète cette analyse pour évaluer la ténacité dynamique.

Au premier abord, le comportement dynamique de la glace sous impact est étudié avec des échantillons cylindriques afin d'établir la relation contrainte-déformation dynamique qui sera utilisée dans les simulations numériques plus tard.

Nous avons observé de multi-fissuration dans les expériences sur les échantillons cylindriques mais son étude est trop difficile à mener. Pour mieux comprendre la propagation des fissures dans la glace, des échantillons rectangulaires avec une pré-fissure sont employés. En ajustant la vitesse d'impact on aboutit à la rupture des spécimens avec une fissure principale à partir de la pré-fissure. L'histoire de la propagation de fissure et de sa vitesse sont évaluées par analyse d'images basée sur les niveaux de gris et par corrélation d'images. La vitesse de propagation de la fissure principale est identifiée dans la plage de $534 \pm 83 m/s$. Elle varie légèrement au cours de la propagation, dans un premier temps elle augmente et se maintient constante ensuite et diminue à la fin.

Les paramètres obtenus expérimentalement, tels que la vitesse d'impact et la vitesse de propagation de fissure, sont utilisés pour la simulation avec la méthode des éléments finis étendus. La ténacité d'initiation dynamique et la ténacité dynamique en propagation de fissure sont déterminées lorsque la simulation correspond aux expériences. Les résultats indiquent que la ténacité dynamique en propagation de fissure est linéaire vis à vis de la vitesse de propagation et semble indépendante de la température dans l'intervalle $-15 \sim -1°\mathrm{C}$.

MOTS CLÉS : propagation de fissure, facteur d'intensité des contraintes dynamique, glace, Barres de Hopkinson, méthode des éléments finis étendue

Contents

List of Figures

List of Tables

General introduction

The phenomena relating to the fracture behaviour of ice under impact loading are common in civil engineering, for offshore structures, and de-ice processes. To reduce the damage caused by ice impact and to optimize the design of structures or machines, the investigation on the dynamic fracture behaviour of ice under impact loading is needed.

The different failure modes such as fragment, spalling, crushing were observed and studied. Since the mechanism of these failures is complicated, it is tough to study the fracture behaviour of ice with multiple cracks.

The main objective of this work is to study the crack propagation in ice under impact loading. To better understand the fracture behaviour of ice under impact loading, the simplest case is chosen, i.e., a main crack propagating along a straight line. A main crack propagation in ice under impact is a fundamental study for other multiple fractures.

A series of impact experiments is conducted with the Split Hopkinson Pressure Bar. The temperature is controlled by a cooling chamber. The dynamic process of the ice fracture is recorded with a high speed camera and then analysed by image methods. The extended finite element method is complementary to evaluate dynamic fracture toughness.

The thesis is structured in four main parts :

I- The first chapter is devoted to a general literature review regarding the various field considered in this work : first, we recall the major concepts in linear elastic fracture mechanics and dynamic fracture mechanics. Next, the mechanical properties of ice and the influence factors are addressed. Finally, the experimental and numerical approaches commonly used in this field are pointed up.

II- The second chapter describes the experimental procedure used in this work in detail and presents the main results. The impact experiments is conducted by the Split Hopkinson Pressure Bar with different dimensions of specimens. The temperature is controlled by a cooling chamber. The dynamic process of the ice fracture is recorded with a high speed camera. The stress-strain curves from the SHPB measurement identify the dynamic behaviour

of ice under impact loading. The images captured by the high speed camera shows the crack propagation path.

III- The third chapter presents the image analysis methods used in this work and describes the crack propagation in ice under impact loading more accurately than naked-eyes. The concepts of grey scale and digital image correlation are introduced first. Then two methods are used to locate the crack tip, observe the crack path and measure the crack propagation velocity. Next, we try to use the displacement fields extracted by DIC to calculate the stress intensity factor. Due to the bad image quality, the results are not accurate enough.

IV- The last chapter is dedicated to the numerical method used in this work. Due to bad conditions of illumination, it is hard to get high resolution images for DIC to estimate SIFs. The eXtended Finite Element Method(XFEM) is used to assess dynamic crack propagation criteria in this work. When the simulation fits the experiment, the crack initiation toughness and the crack growth toughness can be evaluated from the simulation results. The factors that influence the fracture toughness are found, and the relationship between the crack growth toughness and crack propagation velocity is established.

The thesis ends with a summary of the main results obtained and an overview of some perspectives.

Chapter 1

State of the art

In this first chapter, we address a brief bibliographic review regarding the various fields considered in this work. First, the major concepts of fracture mechanics used in this work are reviewed. Then, the mechanical properties of ice especially the fracture behaviour are recalled. Finally, the experimental and the numerical method used to study the fracture behaviour of ice are introduced.

Contents

1.1 Major concepts of Fracture mechanics

1.1.1 A Brief history

Fracture mechanics originates from the investigation on the failure under a stress lower than the strength of a material at the beginning of the 20th century.

The symbolic work is contributed by Inglis [Inglis, 1913] who studied the stress distribution in an infinite plate with a crack simplified as an elliptic hole under tension, and determined stress concentration around the hole. The stresses tend toward infinity when distance from the crack tip tends toward zero. It explains the puzzled for years problem that the actual strength of the material is much lower than the theoretical strength. It is regarded as the firstly presentation of fracture mechanics.

In order to evaluate the crack propagation, the fracture criteria are developed base on energy, stress, displacement and new parameters.

Griffith [Griffith, 1921] studied crack propagation in glass ceramics and other brittle materials, and described the failure with an energy release rate criterion rather than a maximum stress for brittle material crack propagation. And then Irwin [Irwin, 1948] and Orowan [Orowan, 1949] extended the energy theory to a crack tip with a small scale yield in metallic material independently. Dugdale [Dugdale, 1960] and Barenblatt [Barenblatt, 1962] studied the plastic zone close to the crack tip and developed D-B model which is an energy approach considering non-linear aspects.

Irwin [Irwin, 1957] studied stress field near the crack tip, proposed a new fracture parameter, stress intensity factor, to evaluate the intensity of the singularity in the vicinity of a crack tip, and established the stress intensity factor criterion. And the critical value is called fracture toughness which represents the potential ability of a material to withstand a given stress field in the vicinity of a crack tip.

Wells [Wells, 1965] proposed crack opening displacement criterion to determine crack initiation under elastoplastic condition on the basis of a large number of experiments and engineering experiences. But it is not a strict characterization parameters for elastoplastic crack tip stress and strain field.

Rice [Rice, 1968] proposed J integral which using the path-independent integral loop around crack tip as an average parameter to express strain concentration characteristic near crack tip avoids calculating elastoplastic stress-strain field near the crack tip directly.

Then fracture mechanics is expanded to dynamic conditions. Mott [Mott, 1948] conducted a quantitative calculation of rapid crack propagation velocity and introduced kinetic energy to Griffith energy criterion. Yoffe [Yoffe, 1951] proposed a model of a crack that propagates from a fixed length at a constant velocity. Broberg [Broberg, 1960] considered a crack that propagates from zero initial length at constant velocity. Bluhm [Bluhm, 1969] proposed an important crack

arrest issue which is identified through the crack tip equation of motion. Kostrov [Kostrov, 1966] found the first exact stress intensity factor solution for transient crack growth under mode III crack propagation.

Here, we only give a brief review and some major concepts of fracture mechanics for good understanding of the following.

1.1.2 Fracture mode

Consider a three-dimensional medium containing a crack plane (O,x,z), the crack front will be the line (O,z). The fracture can be divided into three elementary types according to the stress systems in the vicinity of the crack and the associated displacements shown in FIG.1.1.

Mode I – Opening mode (a tensile stress normal to the plane of the crack).

Mode II – Sliding mode also called in-plane shear mode (a shear stress acting parallel to the plane of the crack and perpendicular to the crack front).

Mode III – Tearing mode also called out-of-plane shear mode (a shear stress acting parallel to the plane of the crack and parallel to the crack front).

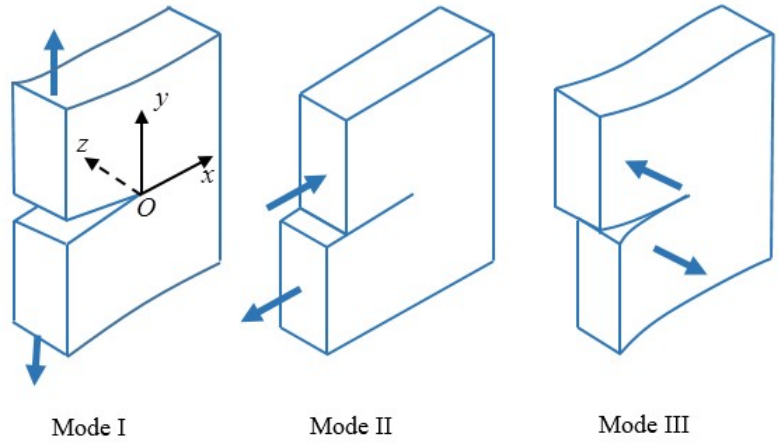

FIGURE 1.1: Three modes of crack stress and displacements

1.1.3 Asymptotic solutions

For a homogeneous, isotropic and linearly elastic solid, the magnitude of the stress field in the vicinity of the crack can be described by a parameter K_i , the subscript correspond to each elementary mode.

The stress and displacement expressions are known as Westergaard's asymptotic solutions [Westergaard, 1939]. The crack tip coordinate system is illustrated in FIG.1.2, the center O is the crack tip, X-axis is the crack propagate direction, Y-axis is normal to the crack plane. The

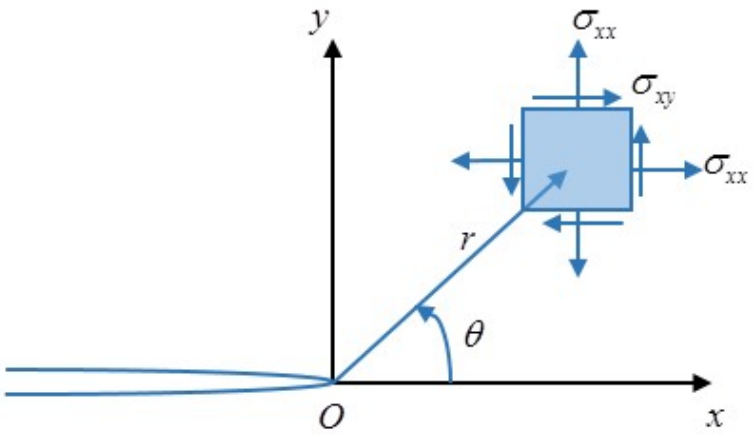

FIGURE 1.2: Crack tip coordinate system

Cartesian components of stress are written in terms of the polar coordinates. E is the modulus of elasticity, ν is Poisson's ratio, λ, μ are Lamé coefficients.

1.1.3.1 The asymptotic solution in Mode I

The stress field is given by :

$$\begin{cases} \sigma_{xx}(r,\theta) = K_I \frac{1}{\sqrt{2\pi r}} \cos(\frac{\theta}{2})(1 - sin(\frac{\theta}{2})sin(\frac{3\theta}{2})) \\ \sigma_{yy}(r,\theta) = K_I \frac{1}{\sqrt{2\pi r}} \cos(\frac{\theta}{2})(1 + sin(\frac{\theta}{2})sin(\frac{3\theta}{2})) \\ \sigma_{xy}(r,\theta) = K_I \frac{1}{\sqrt{2\pi r}} \cos(\frac{\theta}{2})sin(\frac{\theta}{2})sin(\frac{3\theta}{2}) \\ \sigma_{xz}(r,\theta) = 0 \\ \sigma_{yz}(r,\theta) = 0 \\ \sigma_{zz}(r,\theta) = \nu(\sigma_{xx} + \sigma_{yy}) \qquad \text{in plane strain} \\ \sigma_{zz}(r,\theta) = 0 \qquad \text{in plane stress} \end{cases} \tag{1.1}$$

The displacement field is given by :

$$\begin{cases} u_x(r,\theta) = \frac{K_I}{2\mu}\sqrt{\frac{r}{2\pi}} \cos(\frac{\theta}{2})(\kappa - cos(\theta)) \\ u_y(r,\theta) = \frac{K_I}{2\mu}\sqrt{\frac{r}{2\pi}} \sin(\frac{\theta}{2})(\kappa - cos(\theta)) \\ u_z(r,\theta) = 0 \qquad \text{in plane strain} \end{cases} \tag{1.2}$$

1.1.3.2 The asymptotic solution in Mode II

The stress field is given by :

$$\begin{cases} \sigma_{xx}(r,\theta) = -K_{II}\frac{1}{\sqrt{2\pi r}}\sin(\frac{\theta}{2})(2+cos(\frac{\theta}{2})cos(\frac{3\theta}{2})) \\ \sigma_{xy}(r,\theta) = K_{II}\frac{1}{\sqrt{2\pi r}}\sin(\frac{\theta}{2})cos(\frac{\theta}{2})cos(\frac{3\theta}{2}) \\ \sigma_{yy}(r,\theta) = K_{II}\frac{1}{\sqrt{2\pi r}}\cos(\frac{\theta}{2})(1-sin(\frac{\theta}{2})sin(\frac{3\theta}{2})) \\ \sigma_{xz}(r,\theta) = 0 \\ \sigma_{yz}(r,\theta) = 0 \\ \sigma_{zz}(r,\theta) = \nu(\sigma_{xx}+\sigma_{yy}) \qquad \text{in plane strain} \\ \sigma_{zz}(r,\theta) = 0 \qquad \text{in plane stress} \end{cases} \tag{1.3}$$

The displacement field is given by :

$$\begin{cases} u_x(r,\theta) = \frac{K_{II}}{2\mu}\sqrt{\frac{r}{2\pi}}\sin(\frac{\theta}{2})(2+\kappa-cos(\theta)) \\ u_y(r,\theta) = \frac{K_{II}}{2\mu}\sqrt{\frac{r}{2\pi}}\cos(\frac{\theta}{2})(2-\kappa-cos(\theta)) \\ u_z(r,\theta) = 0 \qquad \text{in plane strain} \end{cases} \tag{1.4}$$

1.1.3.3 The asymptotic solution in Mode III

The stress field is given by :

$$\begin{cases} \sigma_{xx}(r,\theta) = 0 \\ \sigma_{xy}(r,\theta) = 0 \\ \sigma_{xx}(r,\theta) = 0 \\ \sigma_{xz}(r,\theta) = -K_{III}\frac{1}{\sqrt{2\pi r}}\sin(\frac{\theta}{2}) \\ \sigma_{yz}(r,\theta) = 0 \\ \sigma_{zz}(r,\theta) = 0 \\ \sigma_{zz}(r,\theta) = 0 \end{cases} \tag{1.5}$$

The displacement field is given by :

$$\begin{cases} u_x(r,\theta) = 0 \\ u_y(r,\theta) = 0 \\ u_z(r,\theta) = \dfrac{2K_{III}}{\mu}\sqrt{\dfrac{r}{2\pi}}\sin(\dfrac{\theta}{2}) \end{cases} \tag{1.6}$$

1.1.4 Fracture Criterion

In order to evaluate the crack propagation, the fracture criteria are developed based on energy, stress, displacement, J-integral and other new parameters. Here, we only introduce the fracture criterion based on the stress intensity factor and J-integral which will be used in the following section.

1.1.4.1 Stress intensity factor

The stress fields in the vicinity of the crack tip has the singularity of type $\frac{1}{\sqrt{r}}$. The stresses tend toward infinity when r tends toward zero. It means that the stress can be no longer used as a criterion in crack propagation. Since K_i can be used to describe the magnitude of the stress field in crack tip, it is called stress intensity factor which is an extremely important fracture mechanics parameter.

The stress intensity factor expressions can be described by the stress and displacement fields as Eq.1.7 and Eq.1.8.

$$\begin{cases} K_I = \lim\limits_{r\to 0}\sqrt{2\pi r}\sigma_y(r,0) \\ K_{II} = \lim\limits_{r\to 0}\sqrt{2\pi r}\tau_{xy}(r,0) \\ K_{III} = \lim\limits_{r\to 0}\sqrt{2\pi r}\tau_{yz}(r,0) \end{cases} \tag{1.7}$$

$$\begin{cases} K_I = \dfrac{2\mu}{\kappa+1}\sqrt{2\pi}\lim\limits_{r\to 0}\dfrac{u_y(r,\pi)}{\sqrt{r}} \\ K_{II} = \dfrac{2\mu}{\kappa+1}\sqrt{2\pi}\lim\limits_{r\to 0}\dfrac{u_x(r,\pi)}{\sqrt{r}} \\ K_{III} = \dfrac{2\mu}{2}\sqrt{2\pi}\lim\limits_{r\to 0}\dfrac{u_z(r,\pi)}{\sqrt{r}} \end{cases} \tag{1.8}$$

The fracture criterion is established by Irwin [Irwin, 1957] based on the stress intensity factor expressed as Eq.1.9. The crack will grow when the stress intensify factor has increased to a critical value which is called fracture toughness commonly denoted by K_{IC} for mode I. The mode II and mode III have the same expressions. It represents the potential ability of a material to withstand a given stress field in the vicinity of a crack tip.

$$K_I \geq K_{IC} \tag{1.9}$$

1.1.4.2 J-integral

The concept of J-integral was developed by Cherepanov [Cherepanov, 1967] and Jim Rice [Rice, 1968] independently. It is a way to calculate the strain energy release rateor work (energy) per unit fracture surface area in a material [Meyers and Chawla, 2009] and characterize the stress-strain field at a crack tip by an independent integration path around the crack as shown in FIG.1.3.

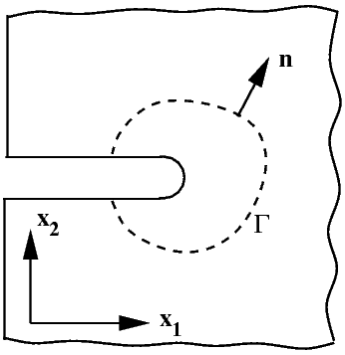

FIGURE 1.3: J-integral path around a crack tip

Consider a crack in a plate subjected to an arbitrary remote loading with an arbitrary closed contour Γ around the crack tip. Then the J-integral is defined in the absence of any body forces as

$$J_{x_k} = \int_{\Gamma} Q_k d\Gamma \tag{1.10}$$

where $k = 1,2$ and

$$Q_k = \left[W_{n_k} - \sigma_{ij} \frac{\partial u_i}{\partial x_k} n_j \right] \tag{1.11}$$

W is the total strain-energy density defined as

$$W = \int_0^{\varepsilon_{ij}} \sigma_{ij} d\varepsilon_{ij} \tag{1.12}$$

The critical J-integral denoted as J_{IC} in Mode I is reached when the crack extension is happened. J-integral is a widely used criterion to assess quantitatively the toughness of a material.

1.1.5 Dynamic fracture mechanics

1.1.5.1 Inertial effect

Dynamic fracture mechanics focuses on the fracture processes in which the material inertia effects cannot be ignored. The inertial effect can be caused by high rate loading or high speed crack propagation. The inertial effects depend on the loading conditions, the material properties and the geometrical configuration.

In our work, the impact is at a high rate loading, the rate of the dynamic stress intensity is in the magnitude of $10^5 \sim 10^6 kPa \cdot \sqrt{m}/s$ and the crack propagation velocity is also high, about $500 m/s$. Both aspects cannot be ignored. Therefore the crack propagation in ice under the impact should be taken as a dynamic fracture mechanics problem.

1.1.5.2 Dynamic fracture toughness

In analogy with the static fracture mechanics, the crack tip stress field is described by dynamic stress intensity factor in dynamic fracture mechanics. The dynamic fracture toughness is a function of temperature, loading rate and crack propagation velocity [Freund, 1998] expressed in Eq.1.13.

$$\sigma_{ij} = \frac{K}{\sqrt{r}} f_{ij}(v, \theta, T, \dot{K}_I) \tag{1.13}$$

Where, v is the crack propagation velocity, r is the distance, θ is the angle, T is temperature, $\dot{K}_I$ is the rate of the dynamic stress intensity factor used to present the rate of loading.

The dynamic fracture criterion is separated in crack initiation, growth and arrest. The dynamic fracture toughness are determined through experiments, unfortunately until now there is no standard for dynamic fracture tests. The experiments should be conducted at interested range of temperatures and rates of loading.

The instantaneous stress intensity factor is denoted as $K_I(t)$. The dynamic stress intensity factor when the crack initiates is identified as the dynamic crack initiation toughness, denoted as $K_{ID}^{initiation}$. If t_f is the crack initiation time, the dynamic crack initiation criterion is described as :

$$K_I(t_f) = K_{ID}^{initiation}(T, \dot{K}_I) \tag{1.14}$$

Once a crack has initiated, the crack propagation velocity must be considered. The dynamic crack growth criterion is expressed as :

$$K_I(t, v) = K_{ID}^{growth}(v, T, \dot{K}_I) \tag{1.15}$$

A commonly accepted view is that the dynamic crack growth toughness has a relationship

with the crack propagation velocity. Based on linear elastodynamic theory, the crack propagation velocity is limited only by the rate of the stored elastic energy transferred to the crack tip, the terminal value is taken as the Rayleigh wave velocity along a free fracture surface [Freund, 1998]. The experimental values measured by investigators in different materials are much lower than the Rayleigh wave velocity. Many scholars focus on finding the relationship between the instantaneous stress intensity factor and the crack propagation velocity [Freund, 1998] [Grégoire et al., 2007] [Ravi-Chandar, 2004a] [Petrenko and Gluschenkov, 1996]. In this work, we pay much attention on this issue.

It needs to be stressed that the dynamic crack initiation toughness does not belong to the function of the crack growth toughness. It means $K_{ID}^{growth}(v \to 0, T, \dot{K}_I) \neq K_{ID}^{initiation}(T, \dot{K}_I)$. This should be possibly due to the bluntness of the initial crack, the intrinsic rate dependence of the material, or inertial effects[Ravi-Chandar, 2004b].

The dynamic crack arrest toughness is identified as the minimum dynamic stress intensity factor for which a crack keeps on propagating. The criterion is defined as :

$$K_I(t) < K_{ID}^{arrest}(T) \tag{1.16}$$

1.2 Mechanical properties of ice

The mechanical properties of ice have been investigated for decades and applied extensively to various domains, such as civil engineering, offshore structures, de-ice processes and aerospace Engineering.

In the last century, various experiments with different ice types, dimensions, conditions have been conducted. The mechanical properties of ice in the quasi-static loading are investigated extensively and deeply.

Since the crash of the Space Shuttle Columbia in 2003 may be attributed to the potential ice impact, the dynamic behaviour of ice, especially under impact, draws the attention of scholars. The ice behaviour at high strain rate, be impacted or impact on structures are investigated. With the development in experimental and numerical methods, different experiments are conducted and simulation models are established. The failure modes such as fragment, spalling, crushing after impact were observed and studied. The investigations trend to lower temperatures and high loading rates.

1.2.1 Types of ice

Ice possesses 12 crystal structures, as well as 2 amorphous states [Schulson, 1999]. At ordinary pressures, the stable phase is termed ice I which has two closely related variants *Ih* and *Ic*. Ice *Ih*

is hexagonal and is obtained by freezing water ; Ice *Ic* is cubic and is formed by vapour deposition at low temperatures.

In our work, the ice specimen is laboratory-grown ice, belong to Ice *Ih* also called ordinary ice, which is the common terrestrial form.

1.2.2 Elastic modulus

The elastic behaviour of ice is characterized by its structure and is influenced by temperature. At temperatures near the melting point, Young's modulus of single crystals varies from $12GPa$ along the least compliant direction to $8.6GPa$ along the most compliant direction. Along directions within the basal plane Young's modulus is $10GPa$ [Fletcher, 2009]. For polycrystalline ice, at a temperature of $-10°C$ Young's modulus of ice is reported in the range of $9.7 \sim 11.2GPa$ and Poisson's ratio is $0.29 \sim 0.32$ [Petrovic, 2003]. At a temperature of $-5°C$, typical values of Young's modulus and Poission's ratio are reported $9.0MPa$ and 0.33 [Fletcher, 2009].

The scattered values make difficult to determinate the parameters for the simulation. We need to measure the elastic modulus ourselves in the same condition as for the crack propagation test.

1.2.3 Brittle behaviour

Ice exhibits two kinds of inelastic behaviour under compression. At low strain rates, the material is ductile. Its stress-strain curve is characterized by ascending and descending branches. At higher strain rates ice exhibits brittle behaviour as shown in Fig.1.4. Its stress-strain curve is characterized by an ascending branch only, and failure occurs after inelastic strains < 0.003 [Schulson, 2001].

Fig.1.5 illustrates the effect of strain rate on the uni-axial compressive strength (C, upper curve) of ice, the tensile strength(T) is shown for comparison. The peak in the compressive strength versus strain rate marks the macroscopic ductile-to-brittle transition which is defined in terms of a specific strain rate $\approx 10^{-4} \sim 10^{-3}s^{-1}$ in small test specimens. And the transition increases with decreasing grain size, increasing salinity, confinement and pre-deformation [Schulson, 2001].

The interested strain rate of our work is in the range $10^{1} \sim 10^{2}s^{-1}$ and in which ice shows a brittle behaviour.

1.2.4 Tensile and compressive strength

When we talk about the strength of ice, two important parameters must be described : the temperature and the strain rate.

Generally, the strength of ice increases with decreasing temperature in both tension and compression as reported by Haynes [Haynes, 1978] and summeried by Petrovic at the temperature

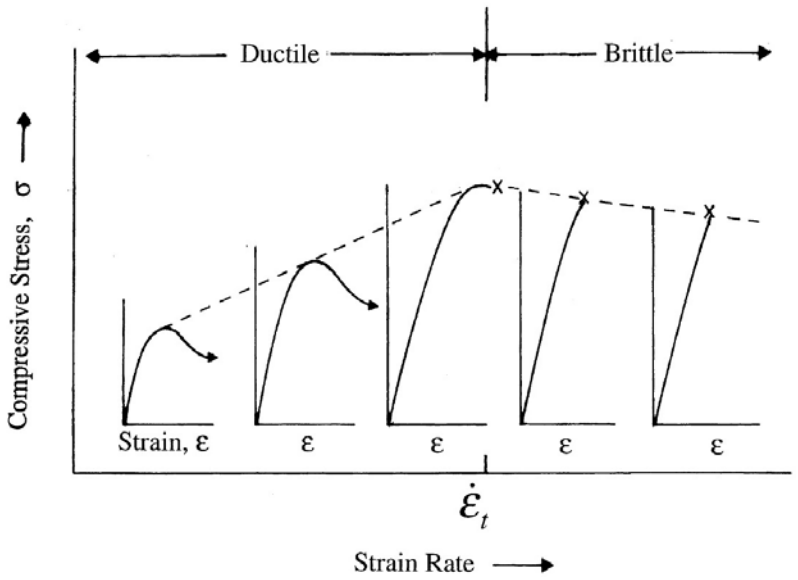

FIGURE 1.4: Ductile to brittle transition [Schulson, 2001]

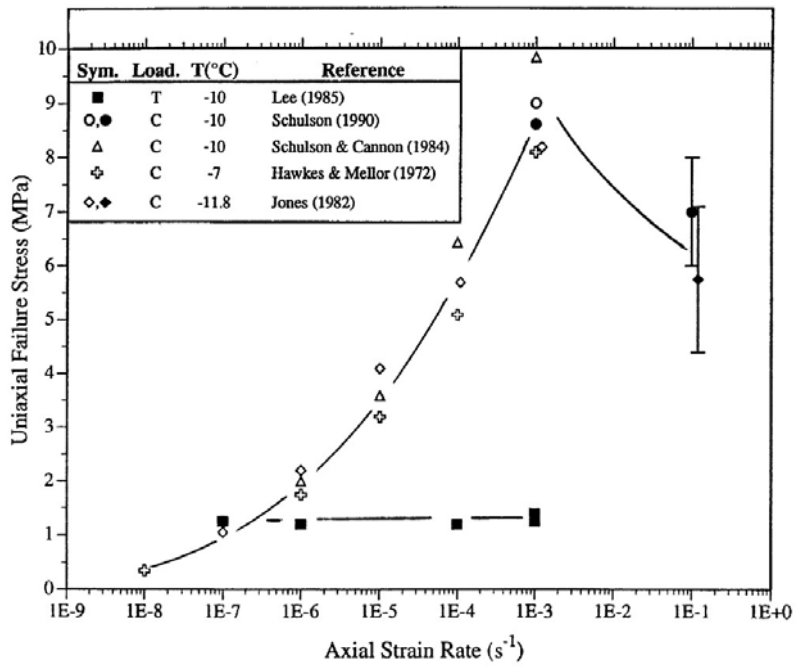

FIGURE 1.5: Uni-axial failure stress versus strain rate [Schulson, 2001]

range of $0 \sim -40°C$ [Petrovic, 2003] as shown in Fig.1.6. And recently, Wu [Wu and Prakash, 2015] conducted the experiments in much lower temperature and observed the same tendency. When the temperatures decrease from $-15°C$ to $-125°C$ the compression strength increases from

$32MPa$ to $112MPa$, and keeps nearly constant in the range $112 \sim 120MPa$ as the temperatures decreases from $-125°C$ to $-173°C$ the corresponding strain rates varies from $272s^{-1}$ to $678s^{-1}$. At the temperature ranges between $-10 \sim -20°C$, the tensile strength of ice is in a wide range of $0.7 \sim 3.1MPa$ [Petrovic, 2003].

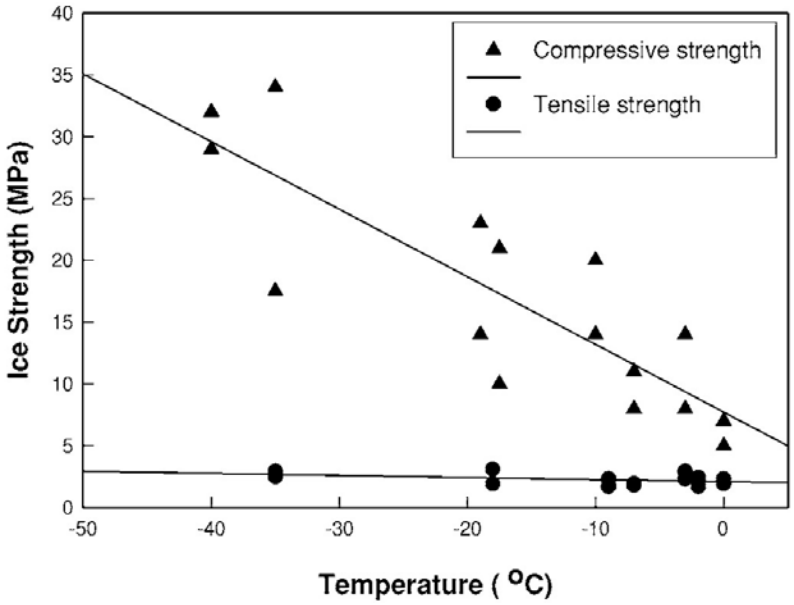

FIGURE 1.6: Tensile and compressive strength of ice as a function of temperature [Petrovic, 2003]

The tensile strength is essentially independent of strain rate, and is only slightly dependent upon temperature, increasing by $< 25\%$ upon cooling from $-50°C$ to $-15°C$, and is heavily affected by grain size [Schulson et al., 1984]. While the compressive strength is strain rate sensitive, it increases from $2MPa$ to $10MPa$ as the strain rate increase from $10^{-7}s^{-1}$ to $10^{-2}s^{-1}$ at the temperature ranges between $-10 \sim -20°C$ [Schulson, 2001].

Equiaxed and randomly oriented aggregates of fresh-water ice fail under uni-axial tension via transgranular cleavage at applied stresses around $1MPa$ [Schulson et al., 1989].

As stated above, the strength of ice is sensitive to the temperature, strain rate which reminded us to carefully control when we conduct the experiments.

1.2.5 Fracture behaviour

The fracture behaviour of ice can be characterized by fractured size as sliding, fragment, spalling and crushing.

The fracture toughness of ice is reported in a large range, from $50kPa \cdot \sqrt{m}$ to $400kPa \cdot \sqrt{m}$ [Liu and Miller, 1979] [Bentley et al., 1989] [Dempsey, 1991] [Petrovic, 2003]. It depends on the variables of temperature, loading rate and ice grain size.

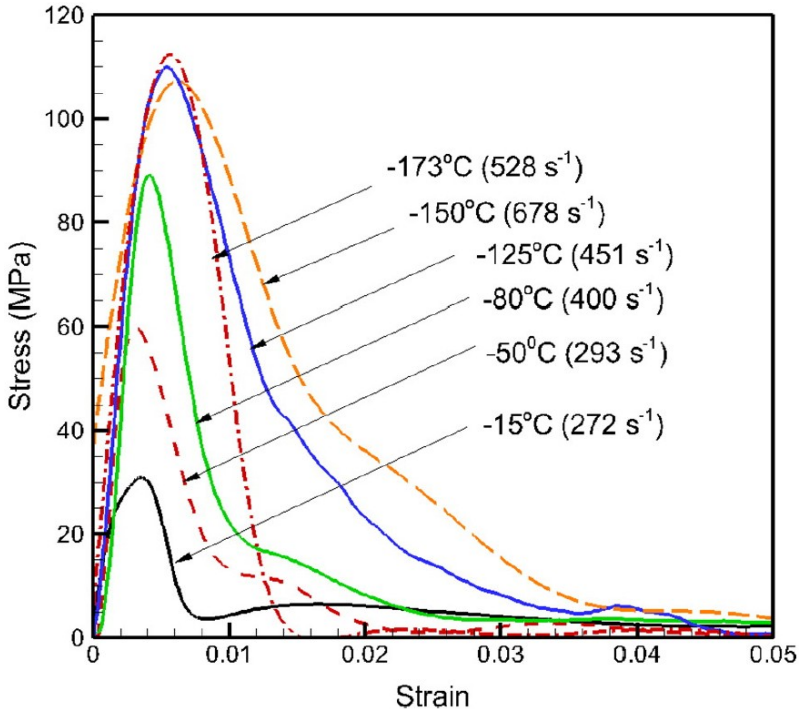

FIGURE 1.7: Dynamic stress versus strain curves at cryogenic temperatures [Wu and Prakash, 2015]

Generally, the fracture toughness of ice increases with decreasing temperature in the range $-1°C$ to $-46°C$ [Liu and Miller, 1979].

The fracture toughness of ice increases with the loading rate in the range $10^{-1}kPa \cdot \sqrt{m}/s$ to $10^{4}kPa \cdot \sqrt{m}/s$ reported by Bentley [Bentley et al., 1989] as shown in Fig. 1.8.

Loading rate was varied from $0.04kPa \cdot \sqrt{m}/s$ to $40.0kPa \cdot \sqrt{m}/s$, and over this range the fracture toughness was observed to decrease from $201kPa \cdot \sqrt{m}$ to $109kPa \cdot \sqrt{m}$ [Nixon and Schulson, 1988]. The fracture toughness exhibits a decrease with increasing grain size as shown in Fig.1.9 [Petrovic, 2003].

1.3 Experimental study on ice

1.3.1 Quasi-static experiment

The conventional specimens in the fracture experiments are CT, CCP, Single Edge Notched Plate (SENT), DECP, 3PT and 4PT whose geometries are illustrated in Fig.1.10. In which, a is the pre-crack length, W is the specimen width and $2H$ is the specimen length [Standard et al., 2004]. These specimens are widely used in metallic materials, ceramics, polymers and composite materials.

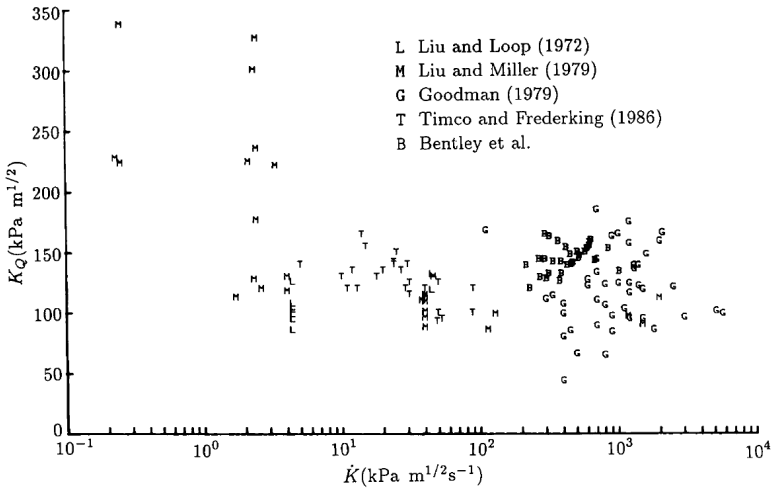

FIGURE 1.8: Fracture toughness of ice over loading rate [Bentley et al., 1989]

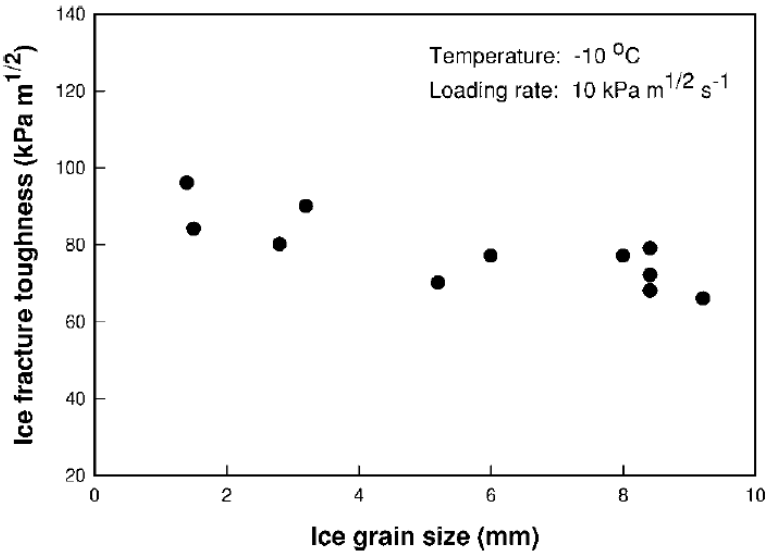

FIGURE 1.9: Fracture toughness of ice over ice grain size [Petrovic, 2003]

But for ice, the standard for fracture toughness measurement are not yet established. With more restrictions of keeping the geometries, three-point-bending Fig.1.10e and four-point-bending Fig.1.10f loading configurations are widely used, and other geometries are also developed. Since the measured values can be compared only with the same standard geometry [Liu, 2005]. The obtained values must be introduced with the geometries.

Bentley [Bentley et al., 1989] used large scale double cantilever beam (DCB) specimens with wedge-loading configuration to investigate the fracture toughness of ice. Fischer [Fischer et al., 1995] used the modified ring test to study the fracture toughness of ice.

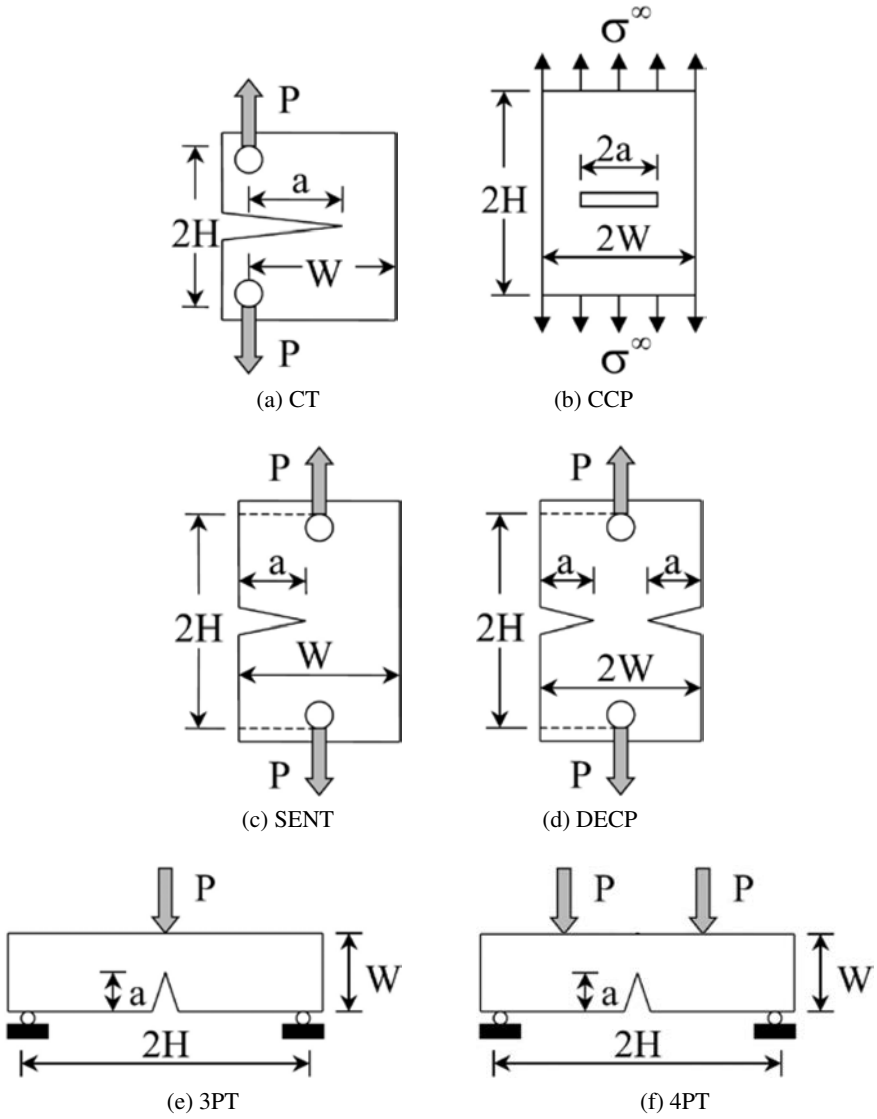

(a) CT (b) CCP

(c) SENT (d) DECP

(e) 3PT (f) 4PT

FIGURE 1.10: Conventional fracture specimen geometries

Dempsey summarised the fracture toughness tests on $S1$ and $S2$ ice with different specimen geometries and experimental conditions[Dempsey, 1991]. The fracture toughness are measured in the range of $50 \sim 300kPa\sqrt{m}$. Most the experiments are conducted in a low loading rate, the rate of the increase of the stress intensity factor is in the magnitude of $10^{-1} \sim 10^{2}kPa \cdot \sqrt{m}/s$.

1.3.2 Dynamic experiment

The phenomena relating to the fracture behaviour of ice under impact are common in various domains, such as ice formed in the high sky and potential impacts on air-plane, hail storm impacts

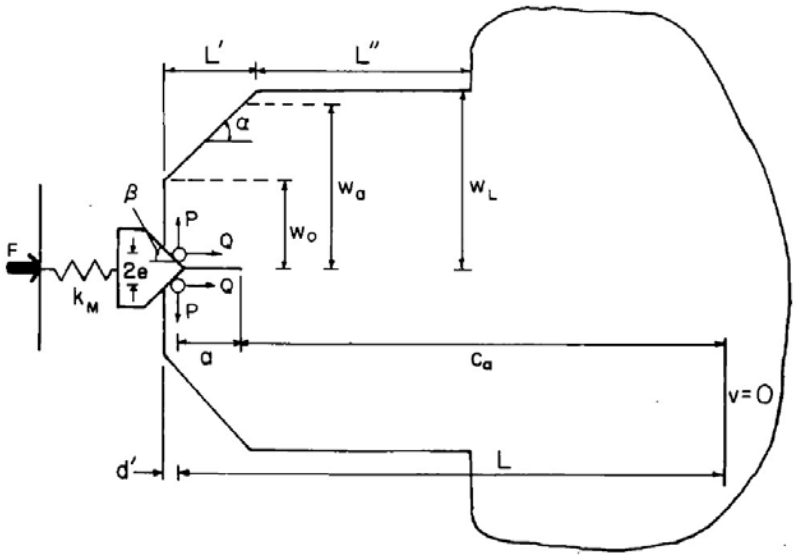

FIGURE 1.11: DCB specimens with wedge-loading configuration [Bentley et al., 1989]

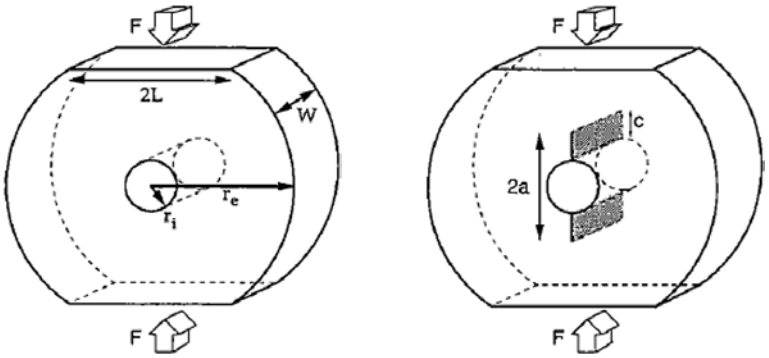

FIGURE 1.12: Modified ring-test specimens [Fischer et al., 1995]

on auto-mobiles and buildings, icebreakers open fairways and machines de-ice on highways as shown in Fig.1.13. To avoid or reduce the damage caused by ice impact, the force generated by ice impact should be estimated. To optimize design of machines used in ice area, the dynamic fracture behaviour of ice under impact loading is studied. A great deal of work has been done by NASA [Pereira et al., 2006] [Melis et al., 2009] [Fasanella et al., 2006] [Chamis et al., 1994] [Reddy et al., 1991] [Lange and Ahrens, 1982]. Two main kinds of experiments are conducted to study the dynamic fracture behaviour of ice : impact and be impacted.

FIGURE 1.13: Phenomena relating to the fracture behaviour of ice

1.3.2.1 Impact directly experiments

The first type of the experiment is to measure the forces on rigid structures upon high speed impact of ice. Combescure [Combescure et al., 2011] study the high-velocity ice fracture mechanisms with the experiments of ice impacting on rigid supports. The fragmentation modes and the deformation are observed and strain response on the impacted plate are measured during the impact. The failure process of the ice specimen is shown in Fig.1.14. The measured crack propagation velocity is about $500m/s$ which can be used to verify our work.

Tippmann [Tippmann et al., 2013] observed the failure progression of an ice sphere during impact with a high speed video and measured the spherical ice impact forces.

1.3.2.2 Be impacted experiment conducted by Split Hopkinson bars

The second type is a rigid structure impacting on ice at different strain rates. Usually Split Hopkinson Pressure Bars (SHPB) are used in this case.

Dutta [Dutta et al., 2004] conducted experiments with S2 freshwater ice at $-10°$C and $-40°$C and a strain rate in the range of 0 to $20s^{-1}$ and indicated the specimens failed progressively in a brittle manner by axial splitting.

Shazly [Shazly et al., 2009] study the dynamic response of ice at a higher strain rates from $60s^{-1}$ to $1400s^{-1}$ at the initial test temperatures of $-10°$C and $-30°$C and indicated the positive strain-rate sensitivity and ice behaving stronger at the lower test temperature over the interested range of strain rates.

Kim [Kim and Keune, 2007] measured the compressive strength of ice at high strain rates range of $400 \sim 2600s^{-1}$ and reported a trend of continuously increasing strength for strain rates beyond $10^1 s^{-1}$ can be observed that is to say ice is a rate sensitive material .

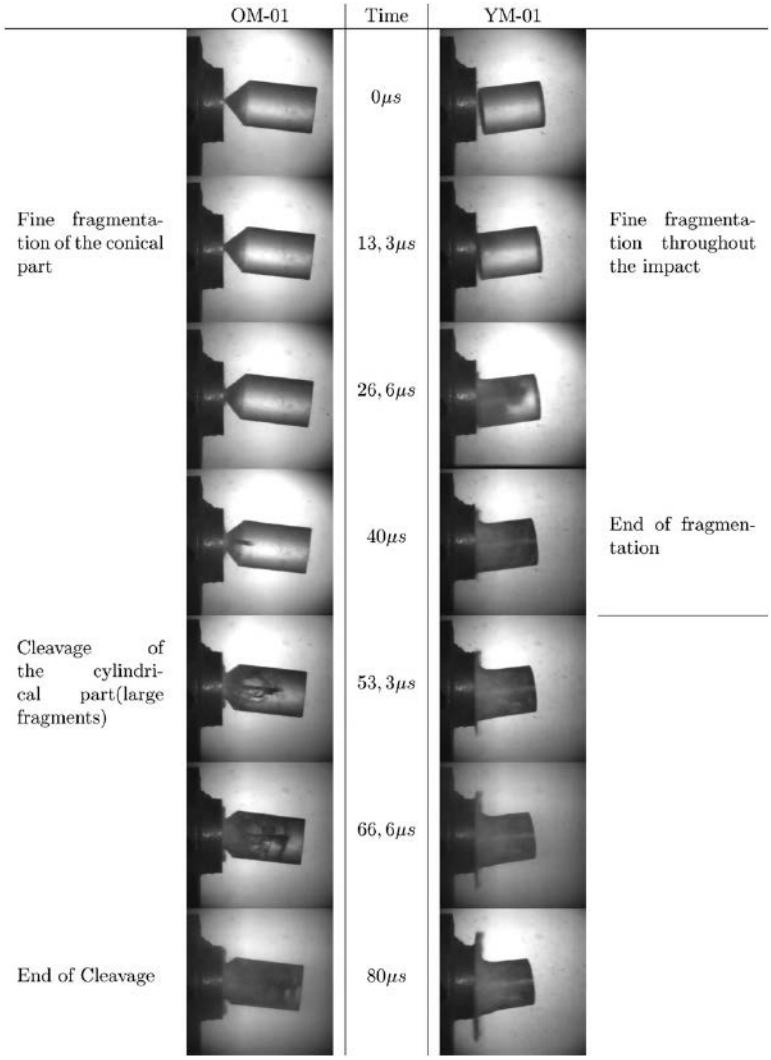

FIGURE 1.14: Failure history of a conic and a cylindrical specimen impacting on a rigid plate [Combescure et al., 2011]

The range of temperature is extended by Wu [Wu and Prakash, 2015] who studied the dynamic behaviour of distilled water ice at temperatures from $-15°C$ to $-173°C$ and at strain rates in the range of $100s^{-1}$ to $1350s^{-1}$. He reported the peak compressive strength increase from $32MPa$ to $112MPa$ as the test temperatures are decreased from $-15°C$ to $-125°C$ and remain nearly constant in the range of $110 \sim 120MPa$ in test temperature from $-125°C$ to $-173°C$.

From above dynamic experiments, we have got the force generated by the ice impact, the approximate crack propagation velocity, the mean strain-stress curves, the fracture process. But we do not know the fracture mechanism of ice under impact loading, such as the critical conditions of the fracture appearance, the intensity factor of the crack initiation and propagation. The multiple cracks make difficult to study the crack tip local information. To better understand the fracture

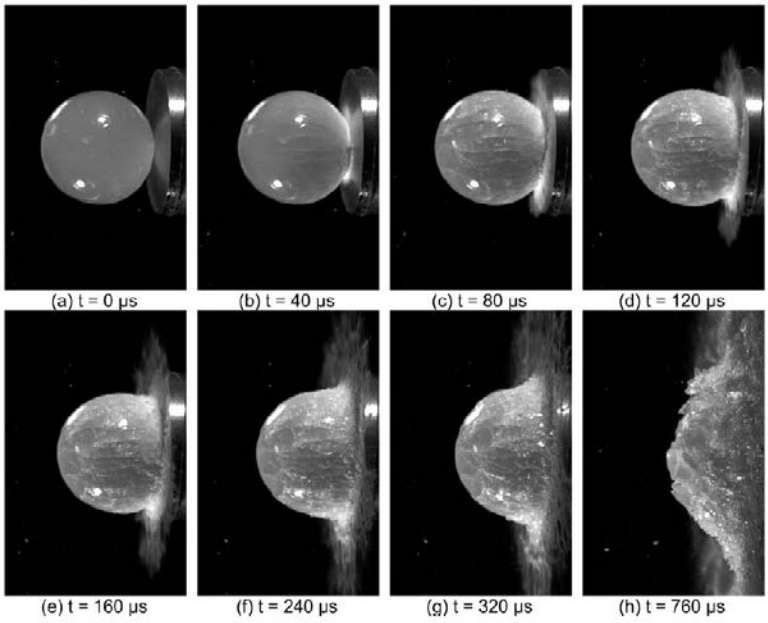

FIGURE 1.15: Failure history of a spherical specimen impacting on a rigid plate [Tippmann et al., 2013]

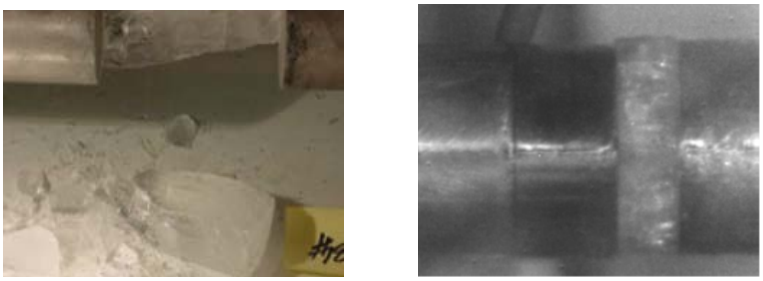

(a) [Dutta et al., 2004] (b) [Shazly et al., 2009]

FIGURE 1.16: Multiple fracture specimen after impacted by SHPB

behaviour of ice under impact loading, the simplest case is chosen in this work, i.e., a main crack propagating along a straight line. A main crack propagation in ice under impact is a fundamental study for other multiple fractures.

1.4 Numerical method for dynamic fracture problem

The numerical method is a complementation of the experimental method. Because of the advantage of high efficiency and low cost, it is widely used and intensively studied. Here, we introduce the significant development in numerical method for dynamic fracture problem briefly.

1.4.1 Finite element method

The finite element method has been widely used for fracture problems for decades. New ideas and techniques are developed to complement the disadvantages of meshing during crack propagation.

Swenson presented a finite element model of mixed-mode dynamic crack propagation in which the discrete cracks are allowed to propagate through the mesh in arbitrary directions[Swenson and Ingraffea, 1988]. Nishioka incorporated the Delaunay automatic triangulation into an automatic moving finite element method which are used to simulate mixed-mode impact fracture tests with fracture-path prediction mode [Nishioka et al., 2001]. Réthoré presented a stable numerical scheme for the finite element simulation of dynamic crack propagation with remeshing using an energy approach [Rethore et al., 2004].

1.4.2 Meshless methods

The meshless methods have two main advantages in fracture problem that it is possible to model arbitrary and complex propagation of cracks without remeshing and adaptive refinement at the crack tip is easily accomplished [Fleming et al., 1997].

Because it does not rely on a mesh but rather on an aggregation of points. Each point has a domain of influence on which interpolation functions are built. These functions are null on the boundary and outside the domain of influence. This is why the influence domain is generally called the support. Enrichment functions can be inserted on these supports and used to model a crack tip [Fleming et al., 1997] [Belytschko et al., 1996].

Element-free-Galerkin(EFG) methods is one of the meshless methods which are based on moving least-square(MLS) interpolates. It is applied to study static and dynamic fracture, wave propagation and the mixed-mode dynamic crack propagation in concrete [Belytschko et al., 1995b] [Belytschko et al., 1995a] [Belytschko and Tabbara, 1996] [Belytschko et al., 2000][Lu et al., 1995]. Then it is developed to 3-D problem[Krysl and Belytschko, 1999].

1.4.3 The partition of unity

The partition of unity method (PUM) is developed for the solution of problems where the classical FEM approaches fail or are prohibitively expensive. One of problems is the crack propagation. It allows for the construction of conforming ansatz spaces with local properties determined by the user [BABUŠKA and MELENK, 1997].

Duarte presented a partition of unity method for the simulation of three-dimensional dynamic crack propagation in which the approximation spaces are constructed using a partition of unity and local enrichment functions. It allows for modelling of arbitrary dynamic crack propagation

without any remeshing of the domain[Duarte et al., 2001].

1.4.4 Extended finite element method

The extended finite element method (XFEM) is a versatile tool for the crack propagation problems which has enormous advantages than the other numerical methods mentioned above. First, the crack surface and crack front are completely independent of the mesh. When the crack propagates, remeshing is not needed. Second, the crack surface is constructed in terms of nodal values by additional basis functions especially combined with level sets. The the crack surface do not must to be placed on element edges. It can be put inside an element and cut the element. It simplifies the model. Furthermore, the singular stress field in the vicinity of crack tip is solved with enrichment functions, the requirement of refinement is reduced [Belytschko et al., 2009].

Belytschko presented a new enrichment technique with loss of hyperbolicity to avoid the difficulties encountered with the original XFEM in time-dependent problems and enable both the crack speed and crack direction to be determined for a given material model [Belytschko et al., 2003].

Réthoré proposed an energy-conserving scheme for dynamic crack growth using the extended finite element method [Réthoré et al., 2005].

Menouillard introduced an explicit formulation of the extended finite element method with a lumped mass matrix for enriched elements. They also reported the critical time step of the extended element is of the same order as the corresponding element without extended degrees of freedom [Menouillard et al., 2006].

Grégoire simulated a mixed-mode crack propagation with extended finite element method which consisted with a dynamic crack initiation toughness, a crack orientation along the maximum principal stress and a simple equation for the calculation of the crack speed [Grégoire et al., 2007].

Bui [Bui and Zhang, 2013] used the extended finite element method integrated with Newmark time integration scheme and the level set method to accurately capture the crack geometry to study the generalized dynamic intensity factors of cracked homogeneous and linear magnetoelectroelastic solids considering the effects of dynamic impact loads, time-step sizes, material polarization directions and interaction cracks.

1.5 Conclusion and recommendations

The objective of this work is to study the crack propagation under impact loading and to evaluate the fracture criteria. According the above literature review, we designed the work implementation process with matters needing attention.

I- The dynamic Young's modulus of ice is scattered reported in the literature. It is depended by the strain rate and the experimental condition. It is difficult to chose the suitable value. Therefore, we need to measure the elastic modulus ourselves in the same condition with the crack propagation test.

II- The dynamic behaviour of ice is complicated. We try to study the crack propagation in ice under impact loading with the simplest case, a main crack propagating along a straight line. A main crack propagation in ice under impact is a fundamental study for other multiple fractures.

III- The behaviour of ice is sensitive to the ice type, the specimen geometry, the test temperature and strain rate which reminded us to control them carefully when we conduct the experiments.

IV- Compared to the other criteria, the stress intensity factor is accustomed used. We also chose this parameter to evaluate the crack propagation.

V- The fracture happens very quickly, we need to observe the process with the help of a high speed camera and image analysis methods.

VI- Compared to the other numerical methods, the extended finite element method has enormous advantages. It is chosen to simulate the experimental process.

Chapter 2

Experimental study on dynamic behaviour of ice

This second chapter is devoted to the presentation of the experimental procedure used in this work. It is divided into five sections : (i) the technique and apparatus to process the experiments ; (ii) specimens and their fabrication ; (iii) the signal analysis with SHPB measuring technique ; (iv) the experimental results evaluated by SHPB measuring technique and the observation of the crack propagation ; (v) conclusions from experiments and recommendation for the future work.

Contents

2.1 Introduction

The mechanical properties of ice are sensitive to the structure of ice, the configuration of specimen, the experimental condition. The strength and Young's modulus of ice were reported in a large range in different literature. Precise values were needed for the following simulation in evaluating the fracture toughness. In order to obtain the strength and dynamic Young's modulus in the same condition with the crack propagation experiment, three groups of experiments were designed firstly :

1) A group of experiments with the cylindrical specimen of a diameter of 50mm was conducted with different impact velocity to obtain the range of strength and Young's modulus.

2) A group of experiments with the cylindrical specimen of a diameter of 50mm with confinement was conducted to investigate the confinement effect. Since the ice specimen in the crack propagation experiment was in an intermediate state between with and without confinement.

3) A group of experiments with the cylindrical specimen of a diameter of 20mm was conducted with a critical impact velocity to obtain the critical strength and Young's modulus of specimen fracture.

Then, with the purpose of investigating the crack propagation in ice under impact loading, two groups of experiments were designed :

1) A group of experiments with the rectangular specimen with a wedge and a pre-crack was conducted with different impact velocity to obtain a main crack propagation.

2) A group of experiments with the rectangular specimen with a hold and a pre-crack was conducted with different impact velocity to obtain a main crack propagation.

For the specimen with wedge, the waves transferred and reflected complicatedly on interface of the wedge and the specimen. It was hard to do signal analysis. Such a problem could be avoided with the rectangular specimens with hole. In this type specimen, the input bar impact on the specimen directly. But the stress distribution was more complex near the hole. So both types of specimens were used.

2.2 SHPB experiment

2.2.1 Test apparatus

The Split Hopkinson Pressure Bar is a mechanical testing apparatus designed specifically to study dynamic mechanical properties of materials at high strain rates from 10^1 to 10^4 s^{-1}. The apparatus has been designed and developed a century ago. Hopkinson [Hopkinson, 1914] firstly measured the pulse induced by an impact on a long bar. Then Davies [Davies, 1948] done a critical work and established the measurement technique. After, Kolsky [Kolsky, 1949] developed the

apparatus into two long bars and a short specimen between them. Since then, SHPB are widely used to investigate the dynamic behaviour of materials.

In our work, the impact tests were performed with the Split Hopkinson Pressure Bar which comprised a striker bar, a long input bar and an output bar with a short specimen between them. The pressure was supplied by an air pump. When the striker bar sustained the pressure and went through the tube, the optical sensors glued on the tube recorded signals which were used to estimate the velocity of the striker bar. A longitudinal compressive stress wave $\varepsilon_i(t)$ was produced into the input bar by the striker bar impacting on. Once the wave arrived at the interface of the input bar and the specimen, a portion was reflected as the reflected wave $\varepsilon_r(t)$, the other went through the specimen and transfers into the output bar called the transmitted wave $\varepsilon_t(t)$. The strains caused by the stress wave were measured with gauges on the input and output bar respectively as voltage signals.

Since the mechanical properties of ice are sensitive to the temperature, especially under dynamic loading. A cooling chamber with a liquid Nitrogen tank was used to control the temperature of the specimen.

The experimental process was recorded with a high speed camera connected to a computer and enlightened with two high brightness low heat lamps. The signals from the optical sensors and the strain gauges were collected by an acquisition card connected to the computer. A Multi-Channel Data Link (MCDL) box was used to establish the synchronization between the SHPB signals and high speed camera videos. A schematic view of the experimental system is shown in FIG.2.1 .

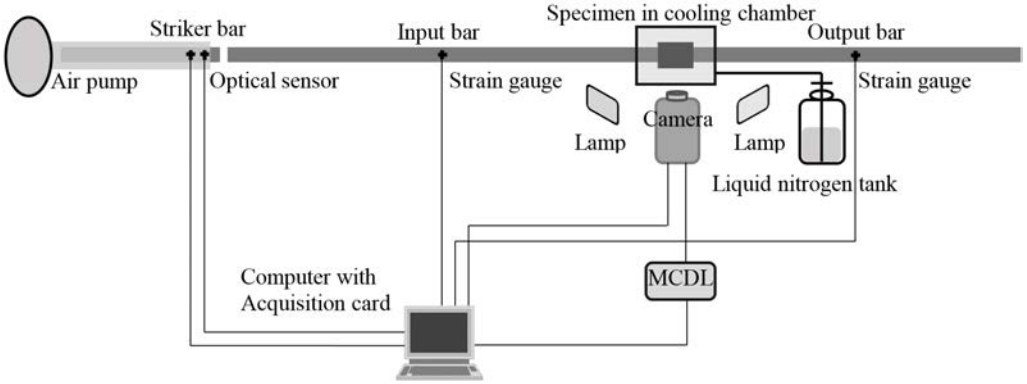

FIGURE 2.1: System of impact experiment for ice

Since the high speed photography method was chosen to study the crack propagation, obtaining high quality images became an important issue. FIG.2.2 is a picture of the cooling chamber. Even equipped with the high brightness lamps, it was still dark inside. Despite the window was made of three-layer glasses, the formation of fog between the glasses and the reflective action affected the image quality seriously. Only few tests supplied clear enough images to be analysed correctly.

FIGURE 2.2: Cooling chamber

2.2.2 SHPB measurement

The SHPB measurement technique is based on three basic assumptions. First, the wave propagates in the bars can be described by one-dimensional wave propagation theory. Second, the stress and strain fields in the specimen are homogeneous in its axial direction. Third, the specimen inertia effect and the friction effect in the compression test are negligible [Zhao, 2003].

FIGURE 2.3: SHPB measuring technique

The incident, reflected and transmitted waves were shifted to the bar-specimen interfaces as shown in FIG.2.3. In a first approximation, one-dimensional elastic wave propagation theory and superposition principle were used to estimate forces and velocities on both bar-specimen interfaces following Eqs.2.1.

$$\begin{aligned} F_{input} &= S_B E(\varepsilon_i(t)+\varepsilon_r(t)) \\ F_{output} &= S_B E\varepsilon_t(t) \end{aligned} \quad \textit{and} \quad \begin{aligned} V_{input} &= C_0(\varepsilon_i(t)-\varepsilon_r(t)) \\ V_{output} &= C_0\varepsilon_t(t) \end{aligned} \tag{2.1}$$

where $F_{input}, F_{output}, V_{input}, V_{output}$ are the forces and velocities on the bar-specimen interfaces. S_B is the cross-section of the bars, C_0 is the longitudinal wave speed in the bars.

With an assumption of homogeneous stress and strain fields, the mean strain, mean stress and strain rate of the specimen were obtained by Eqs.2.2 and then converted to Eqs.2.3 by substituting the stress waves into forces and velocities.

$$\sigma_S = \frac{F_{input} + F_{output}}{2S_S}$$

$$\dot{\varepsilon}_S = \frac{V_{output} - V_{input}}{L_S} \tag{2.2}$$

$$\varepsilon_S = \int_0^t \frac{V_{output}(\tau) - V_{input}(\tau)}{L_S} d\tau$$

$$\sigma_S = \frac{ES_B}{2S_S}[\varepsilon_t(t) + \varepsilon_r(t) + \varepsilon_r(i)]$$

$$\dot{\varepsilon}_S = \frac{C_0}{L_S}[\varepsilon_i(t) - \varepsilon_r(t) - \varepsilon_t(t)] \tag{2.3}$$

$$\varepsilon_S = \int_0^t \frac{[\varepsilon_t(t) + \varepsilon_r(t) - \varepsilon_i(t)]C_0}{L_S} d\tau$$

In equation 2.2 and 2.3, ν is the Poisson's ratio and E the Young's modulus of nylon bars. S_S is the cross-section and L_S is the length of the specimen.

2.2.3 Experimental conditions

As known difficulties in dynamic experiments, especially for ice, most of the experiments fails for various reasons, such as multiple cracks occurrence, bad image quality, incident signals overlap with reflected signals, or the presence of unavoidable defects in the tested specimen. Only a few experiments can be used to supply useful information. The experimental conditions will be presented in details in the following sections. The dynamic fracture behaviour depends on the test temperature and the loading rate. Well controlled experimental conditions are essential to study it.

2.2.3.1 Temperature [$-15°$C, $-1°$C]

The temperature range investigated in our work was from $-15°$C to $0°$C. Although the melting point of ice is one of the most interesting temperature, it was hard to maintain a speckle pattern on the surface of the specimens at $0°$C.

At first, the experiments were conducted at indoor temperature without the cooling chamber. The temperature of the specimen during the experiment needed to be measured. Before the ex-

periment, the specimen was stored in refrigerator at $-15°C$. After the specimen was brought out, the variations in temperature inside and outside the cylindrical specimen of diameter $50mm$ were measured with a temperature sensor. The temperature versus time is shown in FIG.2.4. The experiment would be conducted in 2 minutes. Therefore the temperature when the ice specimen fails should be about $-14°C$.

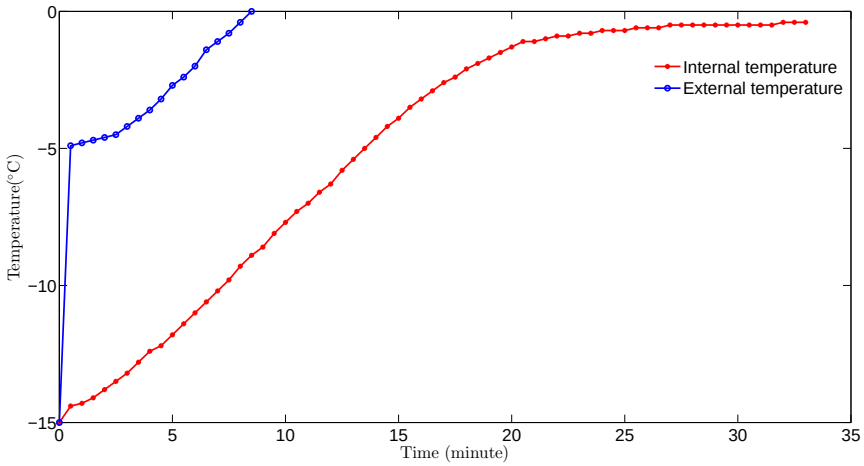

FIGURE 2.4: Internal and external temperature of the specimen vs. time

Then, we used a cooling chamber to control the temperature accurately. After the specimen was brought out of the refrigerator, the specimen was stored in the cooling chamber for 10 minutes until the temperature reached the required value. The experiments were conducted at the temperatures of $-15°C$, $-7°C$ and $-1°C$.

2.2.3.2 Impact velocity [1m/s, 5m/s]

The impact velocity was another key factor for the experiments. Two kinds of impact velocity were measured. One velocity was the striker bar impacting on the input bar measured by two optical sensors glued on the tube. The distance between the two sensors was $50mm$, the time was determined by $signal1$ and $signal3$. Therefore, this velocity was determined. Another velocity was the input bar impacting the specimen determined by the incident signal with Eq.2.4. This kind of impact velocity is more meaningful. It is the velocity at which the input bar impacts the specimen.

To distinguish them, the first kind is called the striker velocity, and the second one the impact velocity in the following section.

$$V_{impact} = C_0 \varepsilon_i(t) \tag{2.4}$$

From experiments, the impact velocity that guarantees a main crack generation was in the

range $1 \sim 5m/s$. If the impact velocity was less than $1m/s$, no crack initiated. If the velocity was larger than $5m/s$, multiple fracture happened. From a large number of experiments, the critical impact velocity of the specimen fracture was about 2m/s.

2.2.3.3 Strain rate [$10s^{-1}$, $100s^{-1}$]

The strain rate is depending on the properties of the bars and the impact velocity. At the beginning, the input and output bars made of nylon with a diameter of $50mm$ were used and which crushed the ice specimens completely. Then, the diameter of the bar was reduced to $20mm$ in order to obtain one main crack. With the purpose of controlling the impact velocity and duration precisely, striker bars made of PVC, PMMA and nylon with different lengths and diameters were tried. The best results were obtained with a PMMA bar of diameter $12mm$ and length $470mm$.

Under the previous impact velocity, the strain rate was in the range of 10-$100s^{-1}$. And the experiments indicated the strain rate increased with the length of specimen decrease.

2.2.4 Selection of bars

2.2.4.1 Selection of the input and output bars

In order to guarantee a good wave transmission on the bar-specimen interfaces, the impedances of the bars and the specimen should be taken into account. Nylon was used for the bars because of the similar impedance with ice. The impedance Z is described by Eq.2.5, S is the section, ρ is the density, E is the Young's modulus, and the subscripts B and S present the bar and the specimen, respectively. The mechanical properties of ice and nylon are listed in TAB.2.1. Some values are collected from literatures, and others are measured by experiments.

$$Z_B = S_B\sqrt{\rho_B E_B} \quad and \quad Z_S = S_S\sqrt{\rho_S E_S} \tag{2.5}$$

Mechanical properties	Nylon	Ice
Density (kg/m^3)	1100	900
Dynamic Young's modulus (GPa)	3.6[Karimzada and Maigre, 2000]	4.0
Poisson's ratio	0.41 [Karimzada and Maigre, 2000]	0.3[Petrovic, 2003]
Velocity of compressive waves (m/s)	1600	

TABLE 2.1: The mechanical properties of Nylon bars compare to ice

For experiments with cylinders, the diameter of the specimen was the same than for bars. For rectangular specimens, the width of the specimen was the same the one of bars, and the section

were designed with a restrictive condition of $Z_B \sim Z_S$. At first, the bars with diameter of 50mm were used. After an impact, the ice specimen was crushed totally even controlling the pressure to the minimum value. Then the diameter of bars were changed to 20mm. By controlling the impact velocity, the cylindrical specimens did not break and the rectangular specimens fractured with a main crack.

2.2.4.2 Selection of the striker bar

To perform the SHPB measurement, the first thing is extracting the incident, reflected and transmission signals. When the stress waves go through the strain gauge on the bar, the voltage signal sharply increases. The pulse is taken as the impact signal. The first pulse in the input bar is the incident signal, and the second is the reflected signal in opposite direction. The first pulse in the output bar is the transmission signal.

But sometimes the end of incident signal overlaps the begin of the reflected signal as shown in Fig.2.5a which makes separation the incident and reflected signals impossible. A good input signal should be as shown in Fig.2.5b, a period equals to zero exists between the incident and reflected signals in which the input bar at the strain gauge location does not sustain stress wave. The end of the incident signal and the begin of the reflected signal can be clearly identified. To achieve it, the impact pulse should be short and the input bar should be long enough. The length of the input bar is restricted to the size of the laboratory. The shape of the impact pulse is determined by the striker bar. Therefore, selection a suitable striker bar is a solution easier to implement which guarantees the separation of the incident signal and the reflected signal.

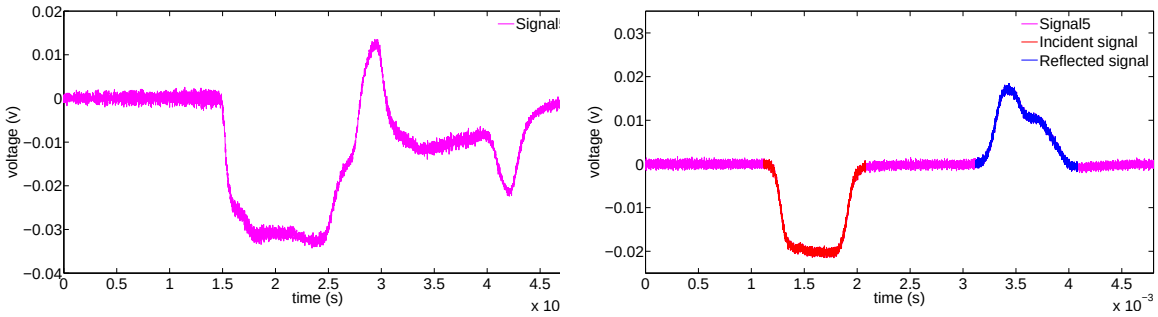

(a) Unseparated incident and reflected signals

(b) Separated incident and reflected signals

FIGURE 2.5: Distinguish the incident and reflected signal

Usually, the striker, input and output bars are of same material and diameter but with different lengths. The chosen diameter was first 50mm. When the diameter of the striker is less, two rings made of nylon are needed to maintain the position to make the three bars in a straight line.

In the case of 20mm bars, the partial superposition of the incident signal and the reflected signal

made the signal analysis impossible. Different striker bars and rings were tried. Three factors were considered : the length and the material of the striker bar, and the material of the ring. The bars made of Nylon, PMMA and PVC are shown from left to right in FIG.2.6.

FIGURE 2.6: Nylon, PMMA, PVC striker bars

First, nylon bars of diameter 20*mm* and different lengths were tried. The detailed data on the tests are listed in TAB.2.2. As shown in FIG.2.7, decreasing the length of the striker bar up to 400*mm* was not enough to separate the incident and reflected signals.

Number	Material	Diameter (mm)	Length (mm)	Pressure (kPa)	Ring
2014092301	Nylon	20	400	80	Nylon
2014092305	Nylon	20	500	80	Nylon
2014092307	Nylon	20	800	80	Nylon

TABLE 2.2: Data for tests conducted by nylon striker bars with different lengths

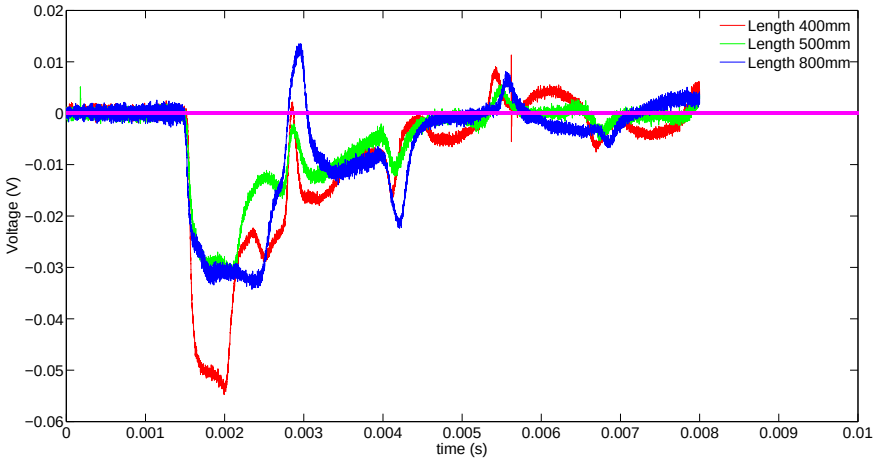

FIGURE 2.7: Input signal of nylon striker bars with different lengths

Then, PVC pipes with a cross section, 12*mm* in diameter with different length were tried. The detailed data on the tests are listed in TAB.2.3. As shown in FIG.2.8, the reflected signal can not be distinguished either. It was concluded that strike bars made of PVC are not suitable to conduct the test.

Number	Material	Diameter (mm)	Length (mm)	Pressure (kPa)	Ring
2014092309	PVC	12	400	80	Nylon
2014092311	PVC	12	800	70	Nylon

TABLE 2.3: Data for tests conducted by PVC pipe striker bars with different lengths

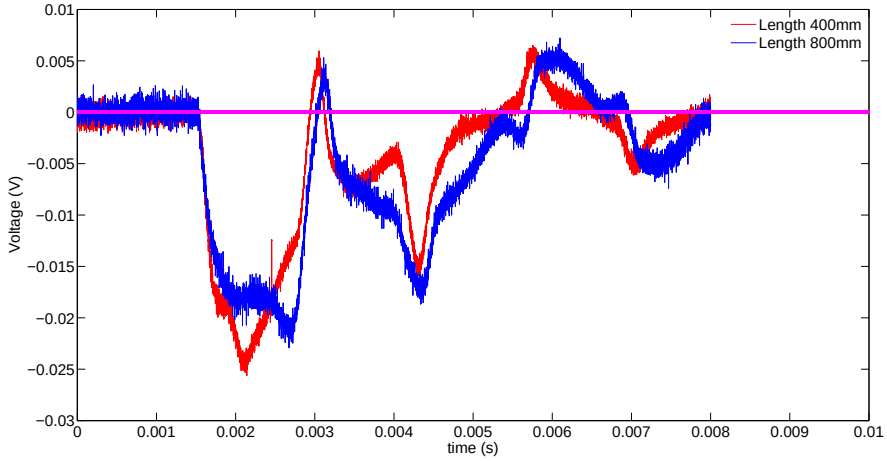

FIGURE 2.8: Input signals of PVC pipe striker bars with different lengths

Third, PMMA bars 12*mm* in diameter with different lengths were tried. The detailed data on the tests are listed in TAB.2.4. As shown in FIG.2.9, the striker bar made of PMMA with the lengths of 470*mm* and 650*mm* both avoid the superposition of the incident signal and reflected signal. In addition shorter is the bar, better is the signal.

Number	Material	Diameter (mm)	Length (mm)	Pressure (kPa)	Ring
2014092601	PMMA	12	470	60	Foam
2014092608	PMMA	12	650	56	Foam

TABLE 2.4: Data for tests conducted by PMMA striker bars with different lengths

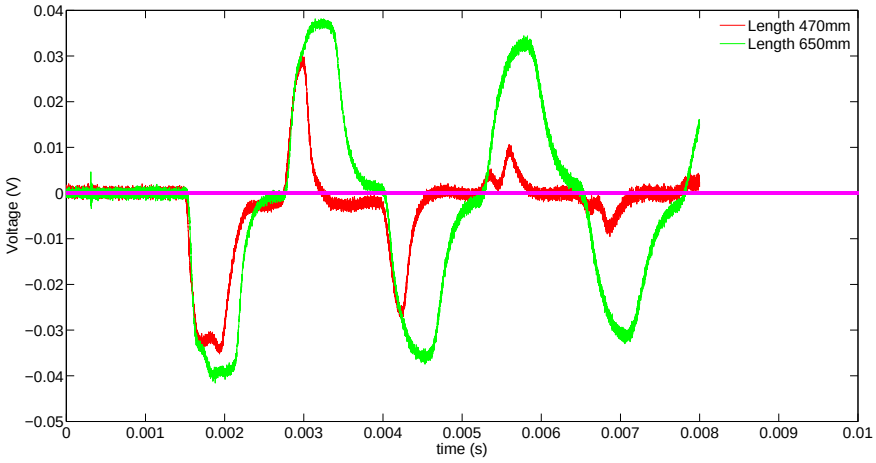

FIGURE 2.9: Input signals of PMMA striker bars with different lengths

For PMMA striker bar, the rings were made of foam. Therefore the effects of rings should be taken into account. The PVC pipe with different rings were tried. The detailed data on the tests are listed in TAB.2.5. As shown in FIG.2.10, the superposition of the signals is less in one nylon ring case than two nylon rings. And the foam ring avoids the superposition of the signals.

The theoretical duration of the impact pulse is given by the length of the striker bar. With rings, the mass increases and the duration also increases. And the mass of the foam rings can be ignored, but the nylon rings can not.

Number	Material	Diameter (mm)	Length (mm)	Pressure (kPa)	Ring
2014092309	PVC	12	400	80	2 Nylon
2014092312	PVC	12	400	70	1 Nylon
2014092315	PVC	12	400	85	1 Foam

TABLE 2.5: Data for tests conducted by PVC pipe striker bars with different rings

In order to sustain the striker bar well, two foam rings were used. Three materials of striker bars with two foam rings were tried. The detailed data on the tests are listed in TAB.2.6. As shown in FIG.2.11, the striker bar made of PMMA with two foam rings provides the best signals.

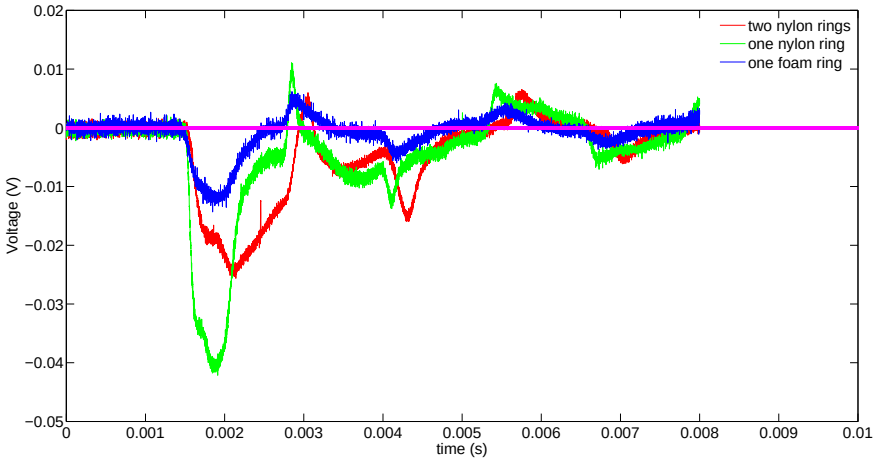

FIGURE 2.10: Input signals of PVC pipe striker bars with different rings

Number	Material	Diameter (mm)	Length (mm)	Pressure (kPa)	Ring
2014092501	PVC	12	400	60	Foam
2014092502	PVC	12	400	60	Foam
2014092510	Nylon	20	400	50	Foam
2014092511	Nylon	20	400	50	Foam
2014092512	PMMA	12	470	50	Foam
2014092601	PMMA	12	470	60	Foam

TABLE 2.6: Data for tests conducted with different striker bars with foam rings

2.3 Ice specimens and their fabrications

2.3.1 Ice specimens

The ice type, the specimen geometry and its preparation have all some effects on the dynamic fracture behaviour. In our experiments, laboratory-grown specimens was ordinary ice, which were prepared by running water with few bubbles. Deionized water and boiled water were also tried, they showed same results. The density of the ice specimens was about $907 Kg/m^3$. It is much easier and cheaper to prepare such ice than trying to reproduce a particular one knowing that impact experiments failed very often.

Two main kinds of specimens were tested. First cylindrical specimens were used for observing the failure mode of the ice under impact loading and studying the constitutive laws of the material

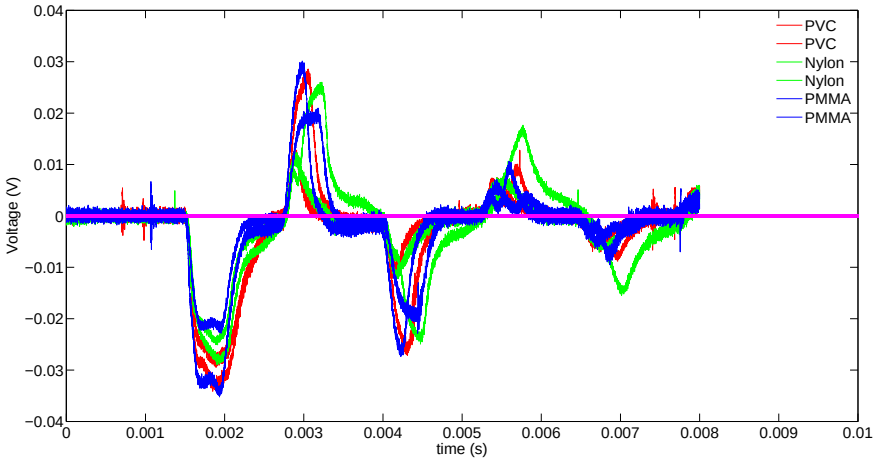

FIGURE 2.11: Input signals of different striker bars with foam rings

at high strain rates and then extracting the parameters for the following simulations. The cylindrical specimens were also tested with a tube to study the confinement influence on the dynamic behaviour of ice. At the beginning, the cylindrical specimens had the same diameter than the bars of 50*mm* and the length were 100*mm*. Then the diameter of specimens was changed to the one of the bars, i.e. 20*mm* and the length set to 45*mm*.

Second rectangular specimens were used for observing the crack propagation in ice under impact and investigating the dynamic fracture criteria. Three different geometries were used : i)rectangular specimen of 230*mm* long with a hole and a pre-crack, ii) rectangular specimen with a hole, but of half-length to get higher strain rate, and iii) rectangular specimen of length 230*mm* with a notch and a pre-crack. The rectangular specimen geometry is shown in Fig.2.12.

For the rectangular specimen with notch, the waves transferred and reflected in a complex manner at the interface between the wedge and the specimen. It is hard to do signal analysis. Such a problem can be avoided with the rectangular specimen with hole. But the stress distribution is more complex near the hole. So both of specimens were used.

2.3.2 Fabrications of ice specimen

2.3.2.1 Cylindrical ice specimens

Cylindrical specimens of diameter 50*mm* and length 100*mm* were prepared in a metallic tube with two metallic caps. The caps could slide in the tube and well sealed with the tube. The inside water did not leak.

Cylindrical specimens of diameter 20*mm* and length 45*mm* were prepared in a metallic tube with two rubber caps. The rubber cap at the bottom of the tube could hold the water and prevent

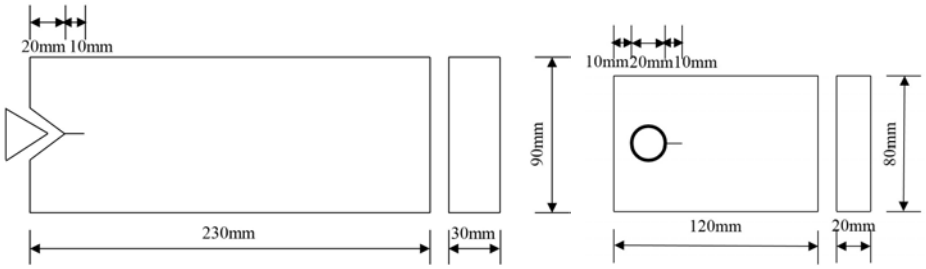

(a) Specimen with notch (b) Specimen with hole

FIGURE 2.12: Dimensions of two types of rectangular specimens

leakage.

Then the specimen with the tube and caps was put into a fridge for 20 hours at $-15°C$.

Afterwards, two ends were polished to ensure a good contact with the bars.

2.3.2.2 Rectangular ice specimens

The fabrication of the rectangular specimens was complicated due to the wedge or hole and the pre-crack. They were prepared with the following procedure :

1. The rough specimens were obtained by pouring water into a cuboid box whose inner surfaces were covered with foam to provide space for volume expansion during freezing. And then the box was put into a fridge for 20 hours at $-15°C$.

2. The specimen was polished until the bubbles at the bottom of the specimen were scarce and both short ends were smooth to ensure a good contact with the bars.

3. The triangular notch was made by putting a metallic cube on a short side of the specimen until the local ice melted and formed a notch. The hole was made by a thread drill. The pre-crack was made by a saw blade.

4. After processing, the specimen was put back into the fridge until the water surface was refrozen.

5. Random speckles on the specimen surface for image analysis were prepared by sprinkling toner uniformly. Attention must be paid to avoid internal cracks and prevent ice forming again in the pre-crack.

It is important to note that during the preparation, melting is unavoidable, especially at the pre-crack tip. Therefore, the slight changed dimensions of the specimens cause a difficulty of guaranteeing uniform size and stable quality.

2.4 Signal processing

2.4.1 Signal extraction

Because of the instantaneous impact, the recorded length and trigger point are important. In our experiment, we recorded about $0.1s$ in total and the interval was $0.8\mu s$. The signal trigger point was determined by the suddenly increasing *Signal*3 which was caused by the striker bar going through the tube. The pre-trigger and post-trigger sizes were pre-defined. Four channels of the signals with the trigger point are shown in Fig.2.13.

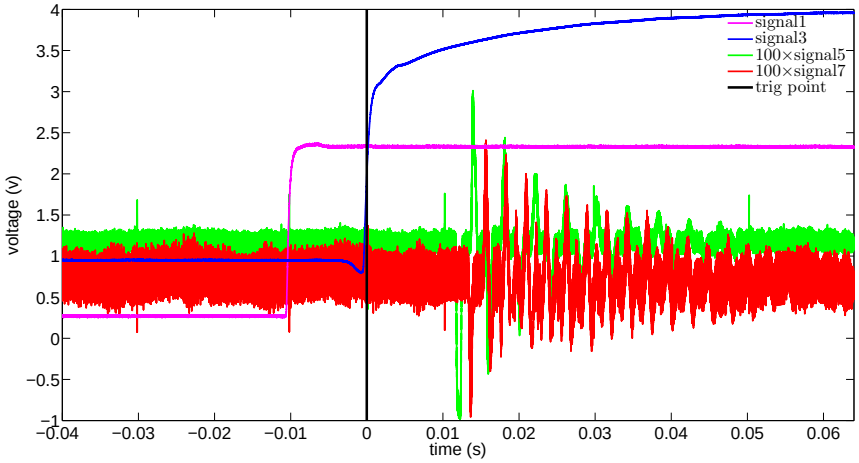

FIGURE 2.13: Signals from a typical experiment

In which, *Signal*1 and *Signal*3 were collected from the optical sensors glued on the tube, *Signal*5 and *Signal*7 were collected from the strain gauges glued on the input bar and output bar. In order to demonstrate clearly, *signal*5 and *signal*7 are magnified 100 times.

Then the meaningful part of the signal used for measure the strain was zoomed in Fig.2.14a

The correction of the offset voltage was done by vertical shifting the signals to zero as shown in Fig.2.14.

Then the incident, reflected and transmission signals were extracted from the input and output signals and plotted after horizontal shifting as shown in Fig.2.15.

2.4.2 Signal filtering

Since the signal was noisy, a filter was designed to improve the quality of the signal by reducing the frequencies of the noise. An example of the filtering process with the incident signal is shown in Fig.2.16.

First, the signal expressed by the time domain was converted into the frequency domain by

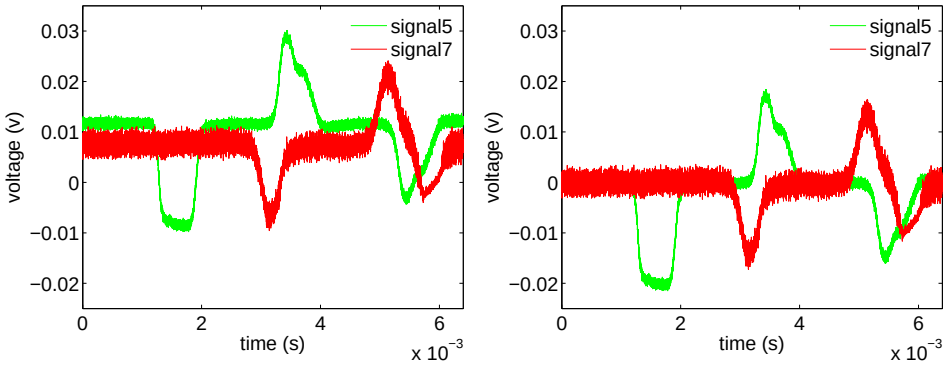

(a) signal before shift (b) signal after shift

FIGURE 2.14: Offset voltage correction

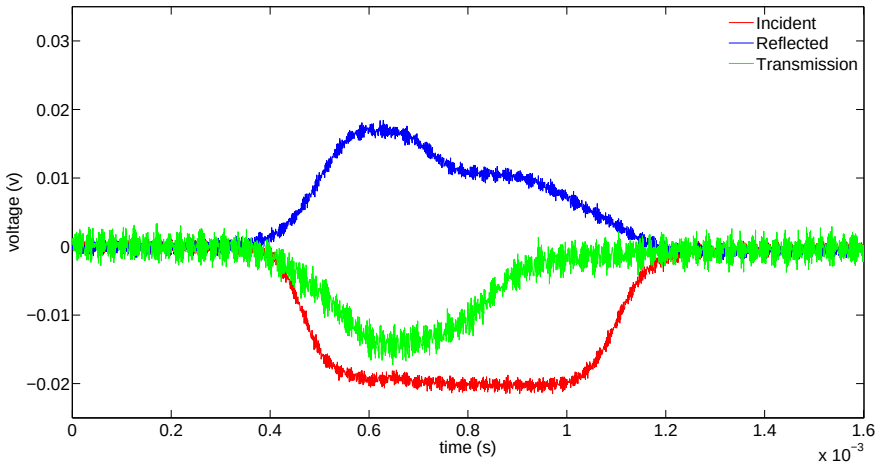

FIGURE 2.15: Incident, Reflected and Transmission voltage signals

Fast Fourier Transform (FFT). Then the signal in time domain was decomposed into real and imaginary components.

As shown in Fig.2.16b, the imaginary components before being filtered is expressed in red. The noise distributed in the high frequency part, of which the frequency is large than $10^4 Hz$. After, a low-pass filter was designed as shown in the Fig.2.16d to attenuate the the high frequency and kept the low frequency part. The blue curve expresses the imaginary components after being filtered. The real component is filtered in the same way as shown in Fig.2.16c. Finally, the complex signal was rebuilt in time domain shown in Fig.2.16a. The curve in blue is the filtered signal, it keeps the same shape with the original signal which validates the design of the filter. If the shape of signal changed, the filter should be changed.

Three signals before and after being filtered are shown in Fig.2.17.

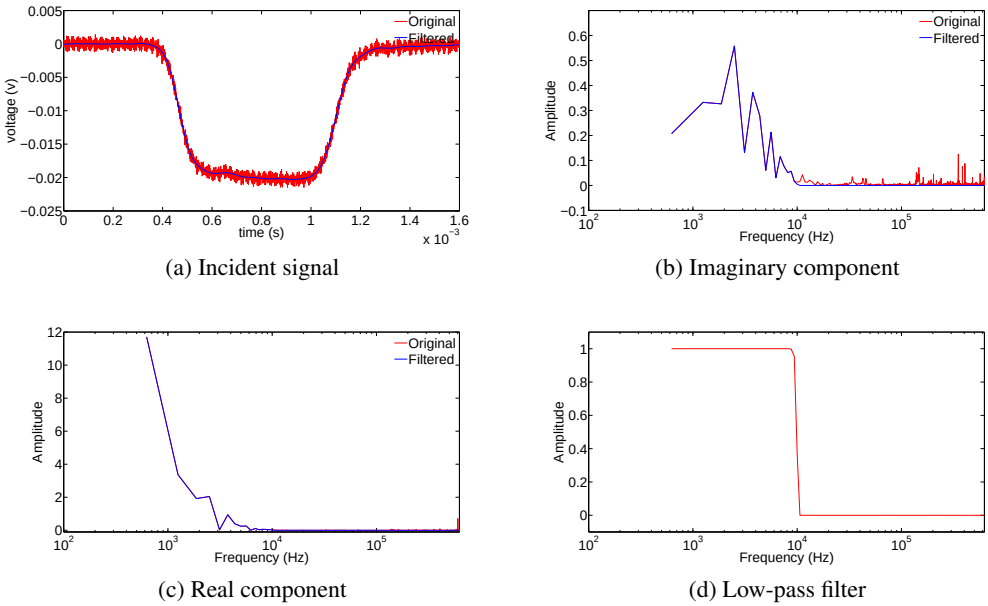

(a) Incident signal

(b) Imaginary component

(c) Real component

(d) Low-pass filter

FIGURE 2.16: Signal filtered with a low-pass filer

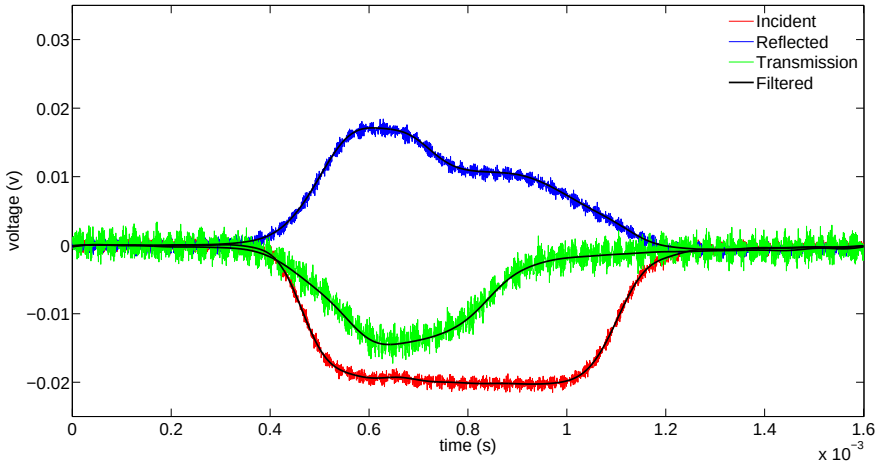

FIGURE 2.17: Signals before and after filter

2.4.3 Signal conversion

The signals collected by strain gauges were voltage signals. They needed to be converted into strain signals before analysis by Eq.2.6 as shown in Fig.2.18.

$$\frac{V_{measure}}{V_{supply}} = \frac{1}{2}(\nu+1)\kappa\varepsilon \tag{2.6}$$

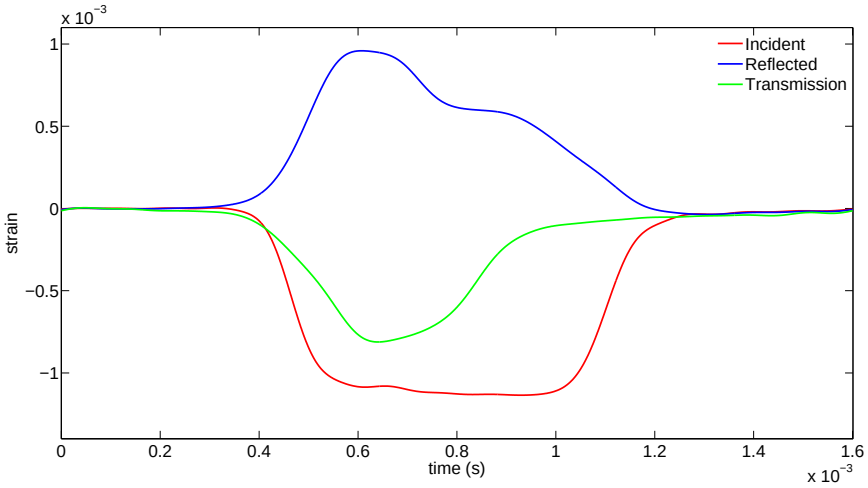

FIGURE 2.18: Strain signals after processing

In equation 2.6, $V_{measure}$ is the voltage signal from gauges, and V_{supply} is the supply voltage. κ is the strain gauge sensitivity factor, ν is the Poison's ratio of the bar. In our work, $V_{supply} = 12V$, $\kappa = 2.11$, and $\nu = 0.41$.

All the signal processing was performed with MATLAB.

2.5 Experiment results

2.5.1 Cylindrical ice specimens

2.5.1.1 Cylindrical ice specimens diameter of 50mm

The specimen in this group had a diameter of 50mm and a length of 95mm, approximately. The experiment was conducted with the 50mm-diameter nylon bars at indoor temperature. As discussed before the temperature when the ice specimen failed was about $-14°$C.

The experimental parameters and results for this group of experiments are listed in appendix A, Tab.A.1 and Tab.A.2,Tab.A.3 and Tab.A.4, respectively.

The impact velocity is a key factor to classify the fracture behaviour.

When the input velocity is larger than 5m/s, the specimen crushed once it was impacted by the input bar. The fracture process of a typical experiment is shown in Fig.2.19, and the parameters of the experiment are listed in Tab.2.7.

Several stress-strain curves belonging to this kind of experiments are plotted in Fig.2.20. The stress increases until reaches a peak value, then decreases quickly. The dynamic Young's modulus measured at the beginning part of the stress-strain curve is in the range of $7.07 \pm 0.80 GPa$, the peak stress is in the range of $7.35 \pm 0.41 MPa$.

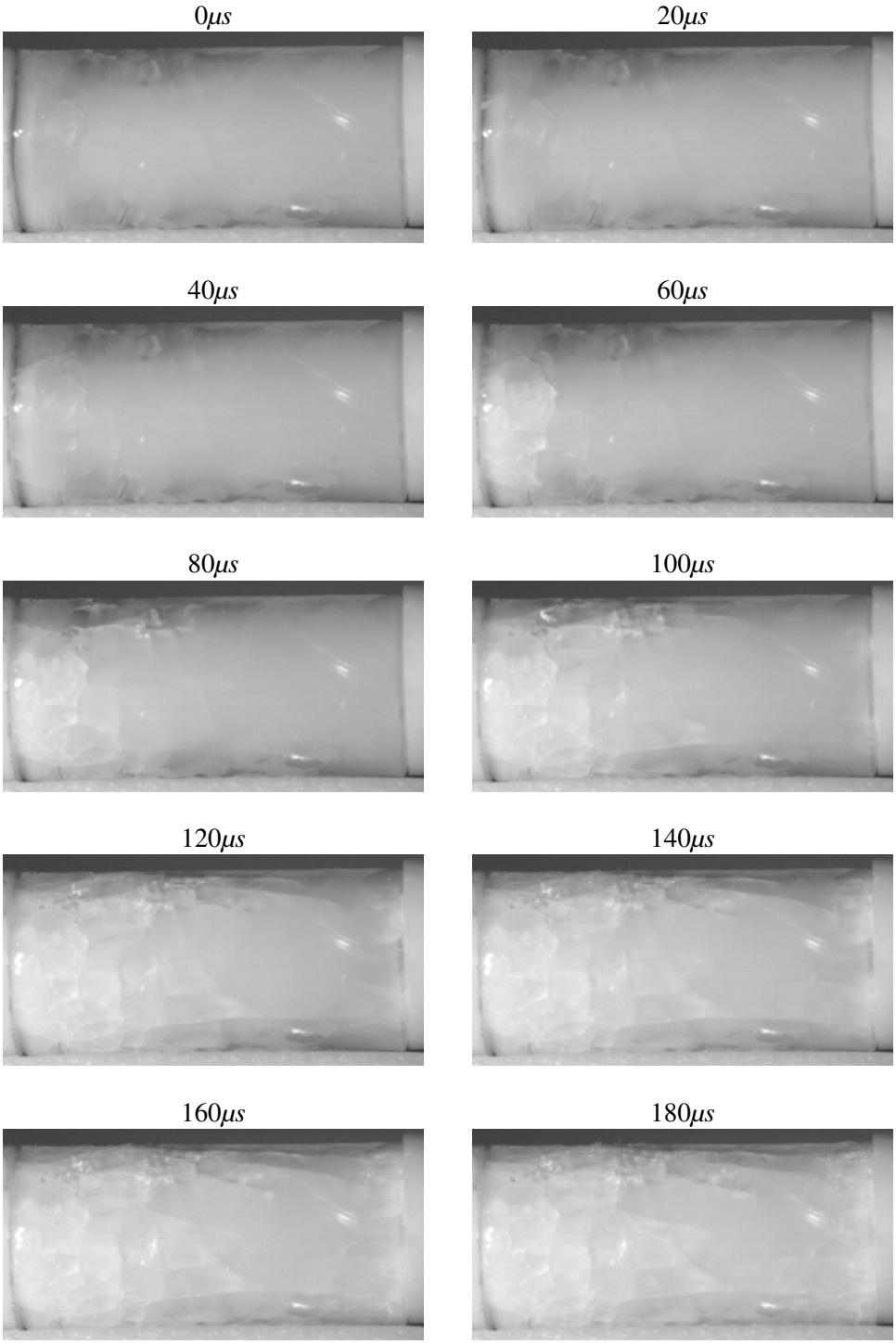

FIGURE 2.19: Cylindrical ice specimen of diameter of 50mm under impact

When the input velocity is in the range of $1.6 \sim 5.0 m/s$, the fracture process of a typical experiment is shown in Fig.2.23, and the parameters of the experiment are listed in Tab.2.8. First,

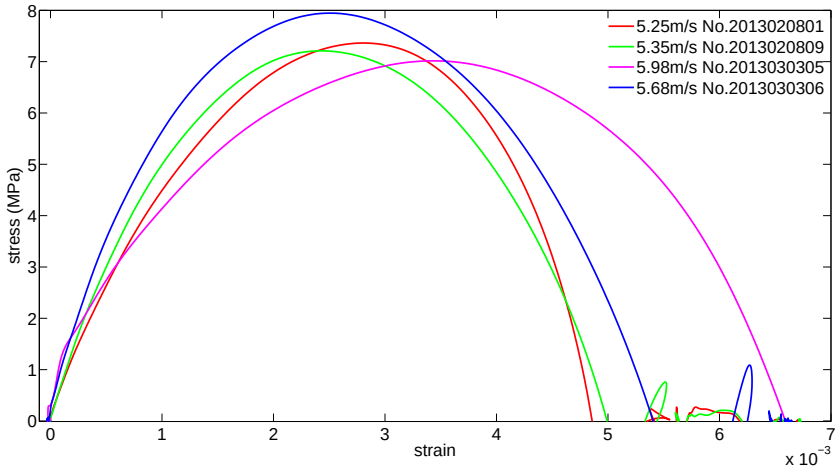

FIGURE 2.20: Stress-strain curves and the evaluated dynamic Young's modulus

Number	Resolution	Interval (μs)	Exposure (μs)	Frame rate (fps)
2013030505	384×288	20	6.9	50000

TABLE 2.7: Image recording parameters for an experiment with a cylindrical ice specimen of diameter of 50mm

several axial cracks generated once the input bar impacted on the specimen. The cracks took about $200\mu s$ to propagate from the left to the right side, the crack propagation velocity was about $500m/s$. In this process, the ice specimen still kept as a whole cylinder but cracks went through inside. Since the stress wave arrived at the interface of the specimen and the output bar, the reflection stress wave generated. Several axial cracks propagated from the right side and reached the middle of the specimen at about $300\mu s$. Then, radial cracks appeared in the middle. The fracture mode could be attributed to the brittle cleavage.

Several stress-strain curves belonging to this kind of experiments are plotted in Fig.2.21. The stress increases quickly in the beginning, then reaches the peak stress, after it decreases slowly which indicates the fragmented ice still sustains the stress. The residual strength can be attributed to the friction between ice fragments. For this kind of experiments, the dynamic Young's modulus is in the range $4.12 \pm 1.72GPa$, the peak stress is in the range of $3.57 \pm 1.05MPa$.

The peak stress values were lower than the result reported by Shazly [Shazly et al., 2009]. The peak stress in his work was reported in the range of $10 \sim 60MPa$ at a high strain rate of $90 \sim 1111s^{-1}$ at $-10°$C. The lower compressive strength can be attributed to unavoidable defects in the laboratory-grown ice specimen. Besides, in our experiment the compressive strength of ice under impact shows a linear association with impact velocity as shown in Fig.2.22. Whereas, Shazly

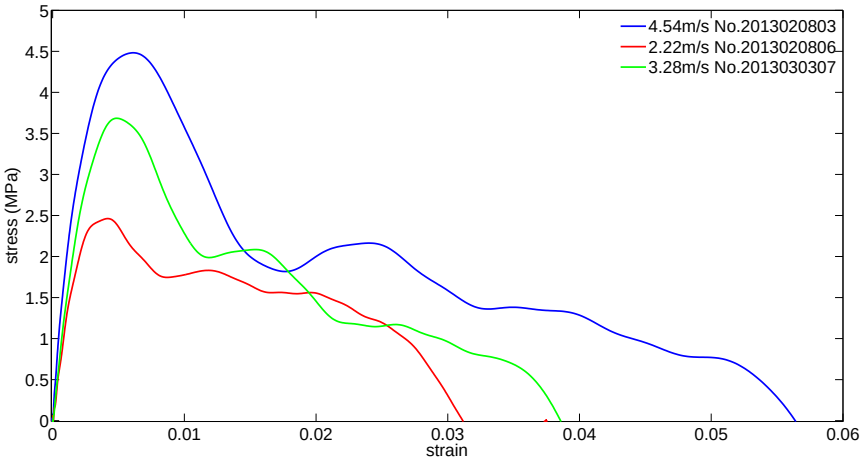

FIGURE 2.21: Stress-strain curves of cylindrical ice specimen diameter of 50mm

Number	Resolution	Interval (μs)	Exposure (μs)	Frame rate (fps)
2013070405	320×160	10,41	5,81	96045

TABLE 2.8: Image recording parameters for an experiment with a cylindrical ice specimen of diameter of 50mm

observed that the strength increases with the strain rate. But in our experiments, this positive sensitivity was not observed. The main reason may be the size effect of the brittle material and the inertial effect.

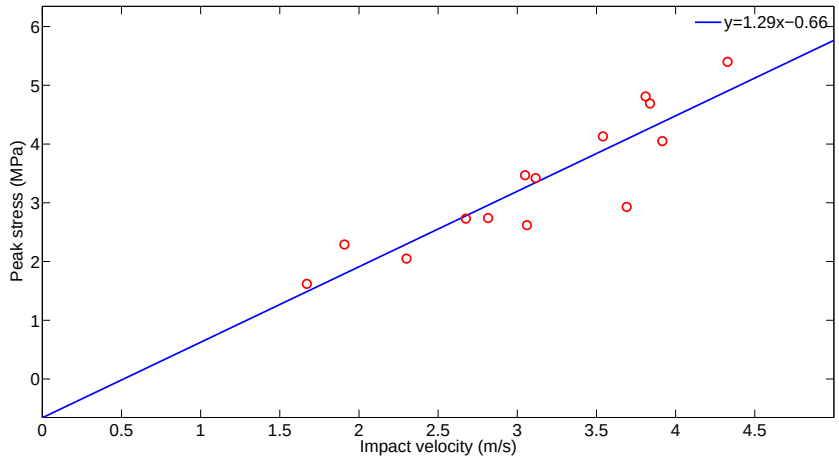

FIGURE 2.22: Impact velocity vs. peak stress

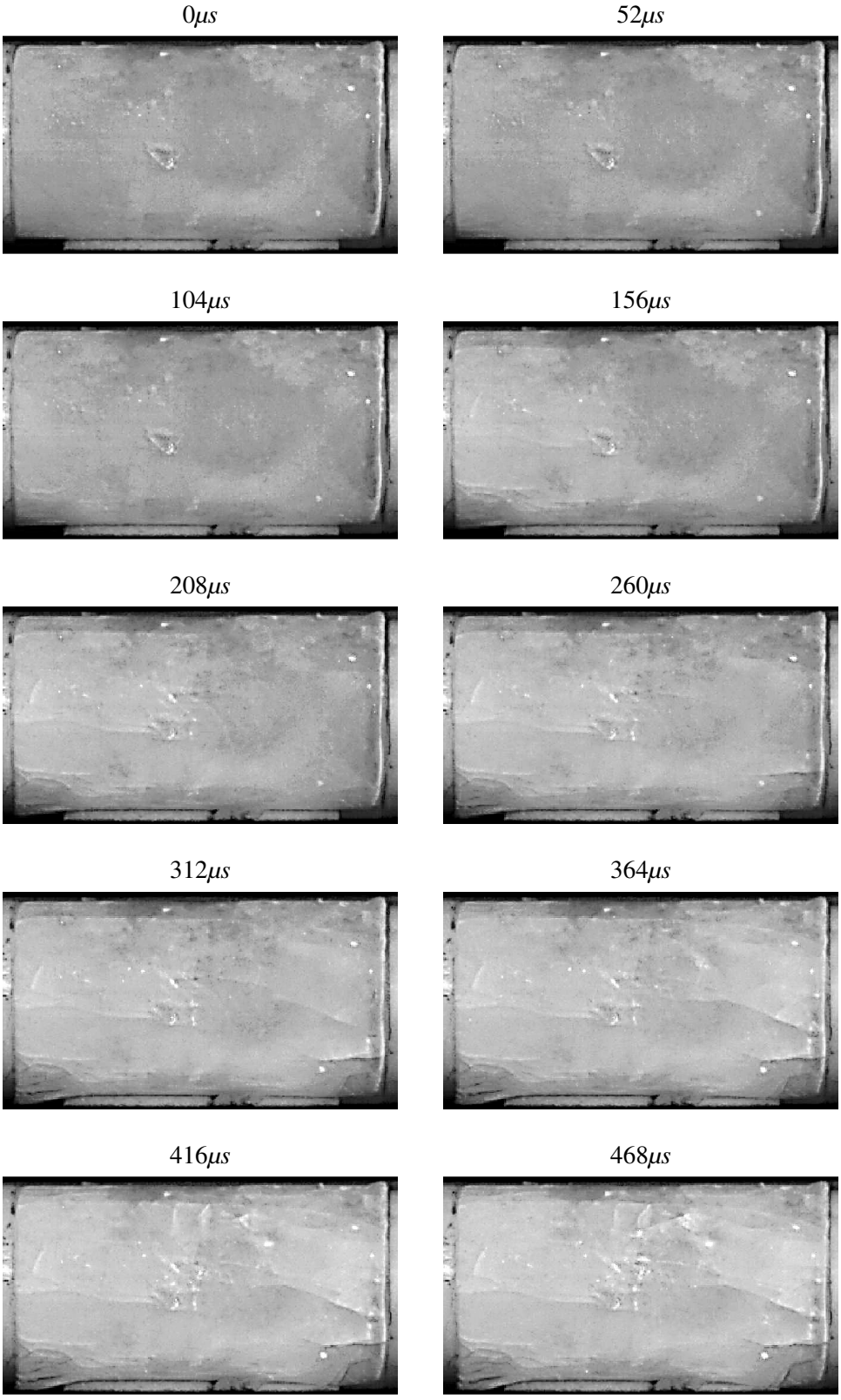

FIGURE 2.23: Cylindrical ice specimen of diameter of 50mm under impact

The unapparent sensitivity between the peak stress and strain rate can be attributed to the scattered strain rates due to the bad propagation into the fractured specimen. Meanwhile, the strain rate is determined by the impact velocity and the length of specimen. In our experiment, the length is almost uniform. Therefore, the impact velocity is linear associate with the strain rate. So basically, the linear association between the compressive strength and the strain rate or impact velocity has the same sense in our case. Both the lower impact velocity and the lower strain rate can explain the lower compressive strength.

2.5.1.2 Cylindrical ice specimens diameter of 50mm with confinement

If the confinement effect would change the strength of ice a lot that is an interesting issue. Furthermore, according to the boundary condition the ice specimen in the crack propagation experiment is in an intermediate state between with and without confinement. Therefore, a group of experiments was designed for investigating the confinement effect on the strength of ice and validating the simulation results.

The confinement was supplied by a rigid metallic tube with a thickness of $8mm$. The specimen in this group had a diameter of $50mm$ and a length of $90mm$ approximately. The experiment was conducted with $50mm$-diameter nylon bars at indoor temperature. The experimental parameters and results for this group of experiments are listed in appendix A Tab.A.5 and Tab.A.6, respectively.

Several typical stress-strain curves are plotted in Fig.2.24. After the peak stress, the stress decreases slightly and then keeps at a plateau value which indicates the fragmented ice still sustains the stress. Then the specimen is compressed. The residual strength can be attributed to the friction of the ice fragments and the radial stress supplied by the confinement. After the impact, most of the specimens fracture but still keep the shape.

The peak stress is in the range of $1.28 \sim 5.12MPa$ with the impact velocity in the range of $1.08 \sim 5.19$. The peak stress increases with the impact velocity. It is close to the results without confinement.

2.5.1.3 Cylindrical ice specimens diameter of 20mm

The specimens with the diameter of $50mm$ fracture with multiple cracks under the impact even if the impact velocity is very low. The critical condition of the fracture happening is interesting but can not be obtained. In order to reduce the impact given to the specimen, the diameter of bars are changed to $20mm$. At the same time, the diameter of the specimen is also changed to $20mm$. The smaller volume has two main influence on the experiment : first, the specimen contains fewer defects which may increase the strength of the specimen. Second, the temperature of the specimen increase quickly after being brought out of the refrigerator. To avoid it, a cooling chamber was used

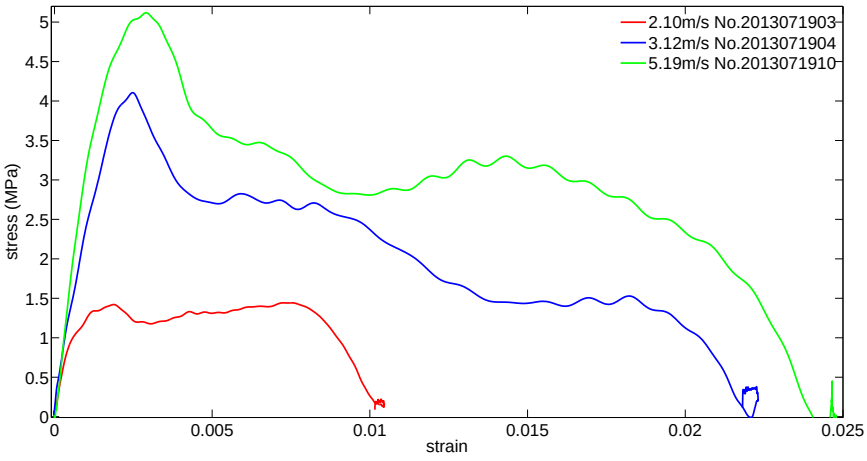

FIGURE 2.24: Stress strain curves for cylindrical ice specimen with confinement

to control the temperature since the behaviour of ice is sensitive to it. The experimental parameters are listed in appendix A, Tab.A.7.

From the video, we can observe the fracture behaviour of 20mm-diameter specimen is different than the one of 50mm-diameter specimen at a lower impact velocity. The axial crack does not happen at the first impact from the input bar. Until the reflected stress generated by the contact with the output bar, the axial cracks initiated from the output bar to input bar. Then the specimen fractures. A typical process is shown in Fig.2.25, and the parameters of the experiment are listed in Tab.2.9.

Number	Resolution	Interval (μs)	Exposure (μs)	Frame rate (fps)
2013053012	384×192	12.5	11.9	80000

TABLE 2.9: Image recording parameters for an experiment with a cylindrical ice specimen of diameter of 20mm

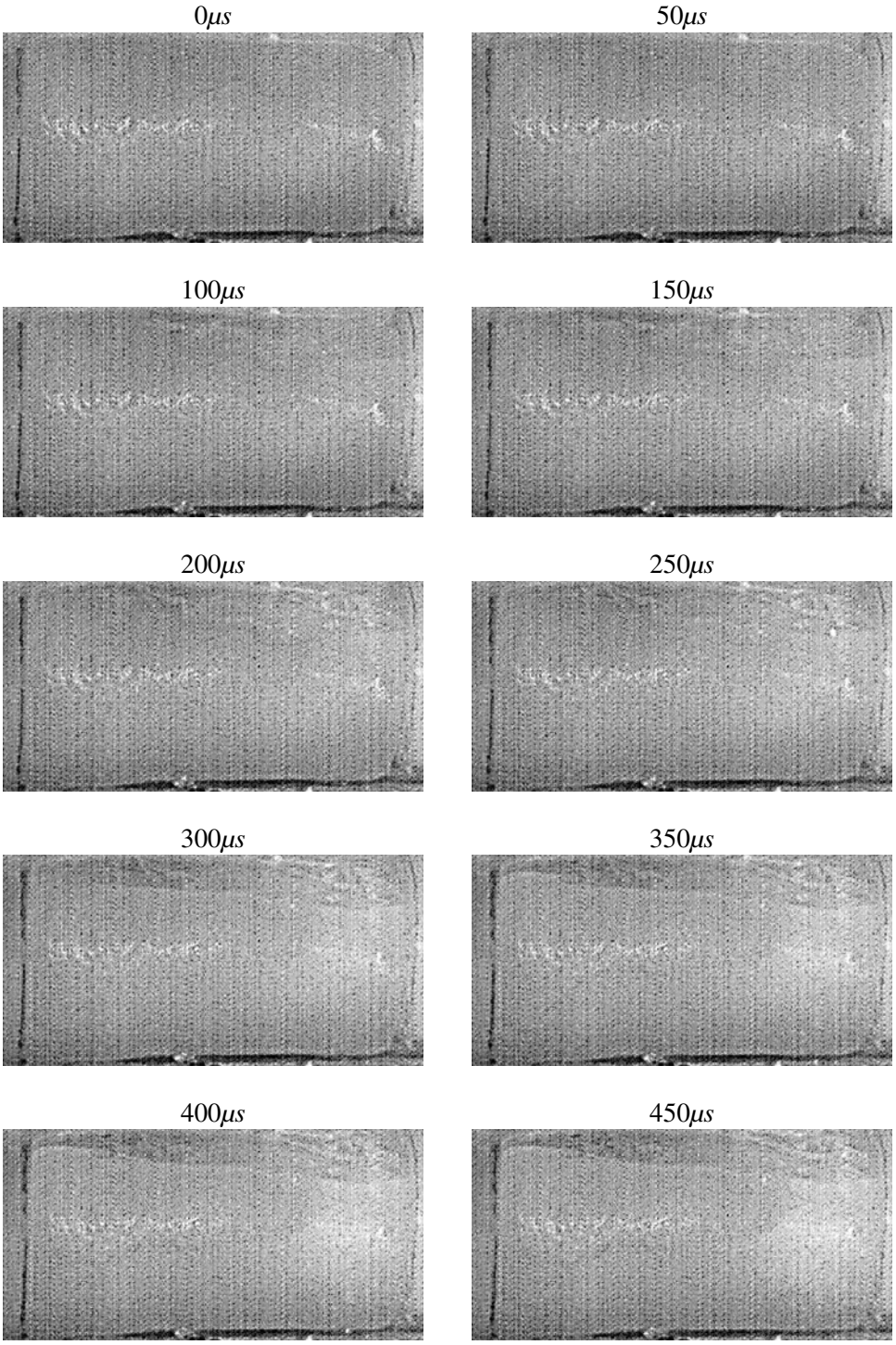

FIGURE 2.25: Cylindrical ice specimen of a diameter of 20mm under impact

The strain rates versus time and the stress-strain relation are plotted in Fig.2.26. The strain rates are in the range of $10 \sim 60s^{-1}$. The dynamic Young's modulus collected from the stress-

strain curves is $3.82 \pm 0.55 GPa$.

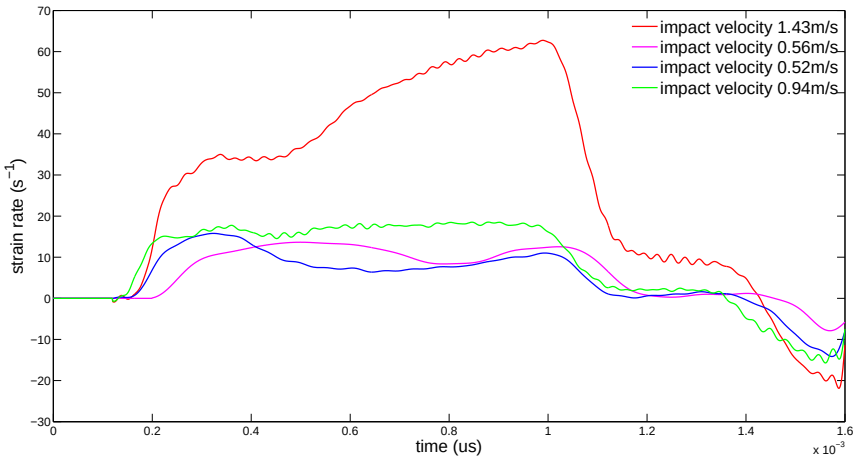

(a) Strain rate

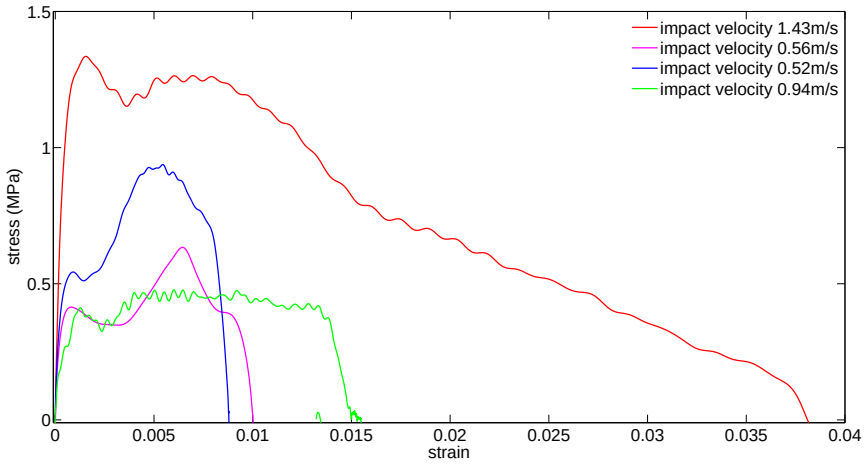

(b) Strain-stress curve

FIGURE 2.26: Mean values for cylindrical ice specimen of diameter $20mm$

2.5.1.4 Validation of dynamic Young's modulus of ice

The Young's modulus of ice is dispersive in a large range in different condition. Roland summarized the range of Young's Modulus and maximum stress values for different strain rates [Ortiz et al., 2015], shown in Fig.2.27. The results indicated from $10 \sim 800 s^{-1}$, the Young's modulus increased with the strain rate increasing.

In our work, the strain rate was in the range of $10 \sim 200 s^{-1}$. The range of Young's modulus

Strain rate (s^{-1})	Young modulus (GPa)	Maximum stress (MPa)
0.01	2–4	8–19
0.1 to 0.4	3.5–5	7–13
10 to 50	2–4	9–13
100 to 800	3–8	11–28

FIGURE 2.27: Range of Young's Modulus and maximum stress values of ice for different strain rates[Ortiz et al., 2015]

could be estimated as $2 \sim 8GPa$ according to Fig.2.27 which confirmed the previous range we obtained $2.4Gpa \sim 7.9Gpa$. But it was still a large range.

The peak stress in our experiment was lower than Roland summarized. This may be caused by unavoidable defects in laboratory-grown specimens, such as small bubbles or micro-cracks.

According to the different fracture types, the previous experiments were divided into three groups : the specimen crushed from the input bar side once being impacted, several axial crack initiated from the input bar side once being impacted, several axial crack initiated from the output bar side after the stress wave arriving at the interface of the specimen and the output bar. The range of the impact velocity, the strain rate, the peak stress and Young's modulus are summarized in Tab.2.10.

Type of fracture	Impact velocity (m/s)	Strain rate (s^{-1})	Peak stress (MPa)	Young's modulus (GPa)
Crush once being impacted	$5.0 \sim 6.0$	66.63 ± 17.42	7.35 ± 0.41	7.07 ± 0.80
Crack initiating input side	$1.6 \sim 5.0$	51.83 ± 47.42	3.57 ± 1.05	4.12 ± 1.72
Crack initiating output side	$0.5 \sim 1.5$	39.25 ± 22.40	0.85 ± 0.38	3.82 ± 0.55

TABLE 2.10: Dynamic Young's modulus, peak stress and impact velocity of ice in different fracture type

For a main crack propagation problem, the fracture type of specimen is in an intermediate state between crack initiating from the input bar side and the crack initiating from the output bar side. Therefore, the dynamic Young's modulus is determined about $4GPa$, this value would be used in the following simulation.

From Tab.2.10, the strain rate is a dispersive feature to classify the experiments. Because for SHPB experiment, the strain rate is decided by impact loading and the length of specimen as expressed in Eq.2.7. Even with the same loading, the different length changes the strain rate. And the peak stress not always appears at the maximum strain rate. For the following rectangular specimen, the stress distribution is not uniform, it is hard to use the strain rate to classify experiments.

$$\dot{\varepsilon}_S = \frac{C_0}{L_S}[\varepsilon_i(t) - \varepsilon_r(t) - \varepsilon_t(t)] \tag{2.7}$$

While, the impact velocity is clear to classify the experiments. For the following experiment, a main crack propagation, the impact velocity should be similar with the type of several axial crack initiating from the input bar side, but a smaller range than $1.6 \sim 5.0 m/s$. The impact velocity is also an easier value to control during the SHPB experiment than the strain rate.

2.5.2 Rectangular ice specimens

The cylindrical specimens were used to investigate the dynamic fracture behaviour of ice under impact loading. The rectangular specimens were used to investigate the crack propagation in ice under impact loading.

2.5.2.1 Rectangular ice specimens with a wedge and pre-crack

First, a rectangular specimen with a wedge and pre-crack was employed to conduct the experiment. The dimensions and fabrication have been introduced before.

A carbon powder was used to plot the random speckles on the surface of the specimen for the image analysis. The temperature needs to be well controlled to avoid melting of the surface of the specimen to maintain the speckles. Another reason is that the dynamic behaviour of ice is sensitive to the temperature.

One key factor for type of specimen is to choose the appropriate wedge to assure an as good as possible contact with the specimen. The refraction and reflection of the stress wave on the interfaces of the wedge and specimen are difficult to analyse. The only useful information from the signals is the impact velocity measured from the incident signal which is not affected by the refraction and reflection.

In order to reduce the refraction and reflection of the stress wave, the same material as the one used for bars, i.e. nylon, was first chosen to make a wedge. The experimental parameters are listed in appendix A, Tab.A.9. Before the impact, the specimen was put into the chamber for 15 minutes until the temperature reached the assigned value. The resolution of the high speed camera was reduced to get the higher interval. Because the crack propagates along the pre-crack, the height of the image could be cut into a narrow band.

After the impact, the ice specimen fractures into several pieces. The crack paths are shown in Fig.2.28. The crack path in experiment *No*.2014022803 is smooth and follows a straight line, the angle between the pre-crack and the crack propagation direction is up to about 7° from the horizontal axis. The others break along lines, and change directions obviously. Especially in experiment *No*.2014022804, the crack path changes direction more than 60°. The difference may be

caused by the impact velocity. The experiment *No*.2014022803 has the minimum value in the five experiments. The angle between the pre-crack and the crack propagation direction can be attributed to the bluntness of the pre-crack and the unbalanced forces on the two wedge surfaces due to the bad contact between the specimen and the wedge.

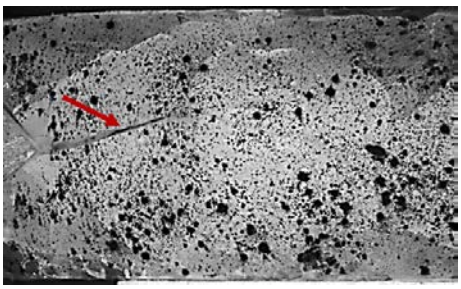

(a) Crack path No.2014022801

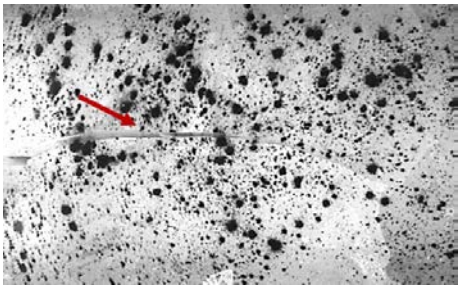

(b) Crack path No.2014022802

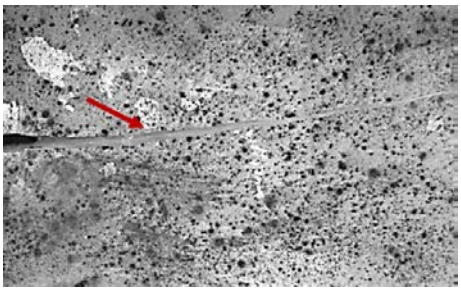

(c) Crack path No.2014022803

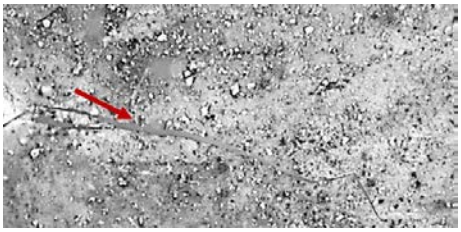

(d) Crack path No.2014022804

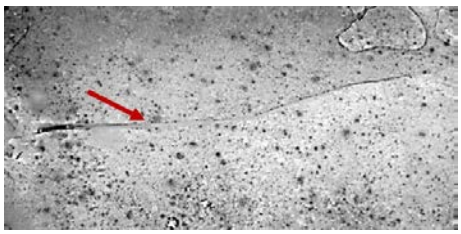

(e) Crack path No.2014022805

FIGURE 2.28: Crack path in rectangular ice specimen with a wedge and pre-crack Group 1

The major drawback of this group of experiments is lacking calibration. In the experiment with the cylindrical specimen, the whole length of the specimen is captured by the high speed camera, and the length is pre-measured. But in this group, in order to increase the interval, the rectangular specimen is only captured a narrow band after the pre-crack and the begin and the end part are not captured. Therefore, the calibration can not be done and the crack path in the image can not be evaluated.

In the second group of the experiment conducted by the specimen with a notch, the wedged is

made by PVC. The purpose of this group is to find the appropriate impact velocity to get a main crack propagation. The experimental parameters are listed in appendix A, Tab.A.11.

After the impact, the ice specimen fractures into several pieces. The crack paths are shown in Fig.2.29. A ruler close to the specimen is also captured in the image used for calibration in image analysis. Multiple cracks happen in this group, and are difficult to analyse. In order to get a main crack propagation, the impact velocity still needs to be reduced.

The major drawback of this group is that the process of the first two experiments are not recorded due to the inappropriate set up trig point.

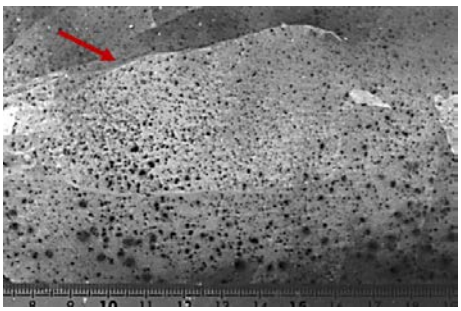

(a) Crack path No.2014030503

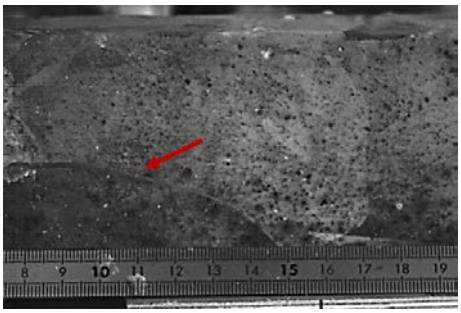

(b) Crack path No.2014030504

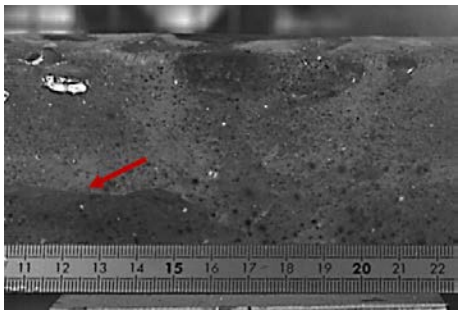

(c) Crack path No.2014030505

FIGURE 2.29: Crack path in rectangular ice specimen with a wedge and pre-crack Group 2

In the third group, a wood wedge was used to transfer the impact to the specimen. The impact velocity was in the range of $1.87 \sim 4.03 m/s$. The experimental parameters are listed in appendix A, Tab.A.13. A main crack is obtained as shown in Fig.2.30.

2.5.2.2 Rectangular ice specimens with a hole and pre-crack

For the rectangular specimens with notch, the waves transferred and reflected complicatedly on interface of the wedge and the specimen. It was hard to do signal analysis. Such a problem could be avoided with the rectangular specimens with hole. But the stress distribution was more complex near the hole where the compression was converted to the traction to make the crack

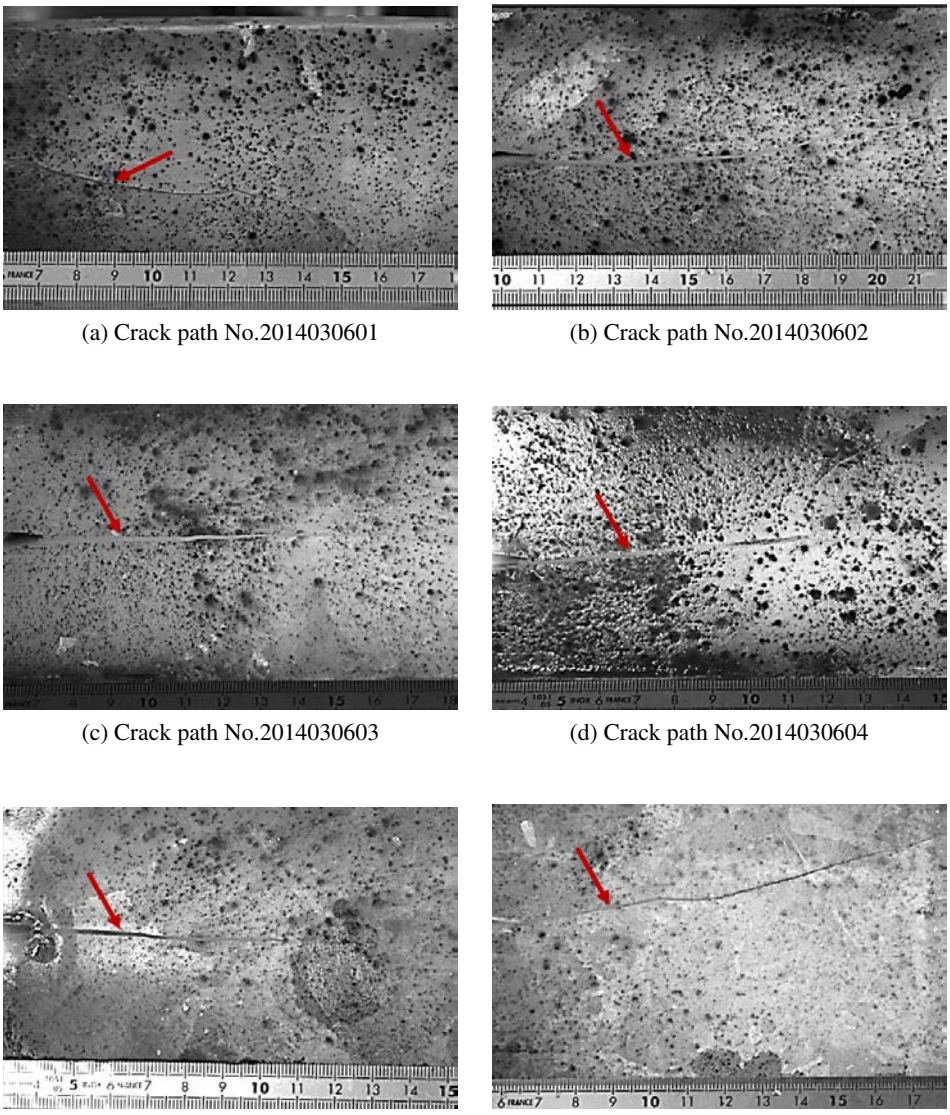

(a) Crack path No.2014030601

(b) Crack path No.2014030602

(c) Crack path No.2014030603

(d) Crack path No.2014030604

(e) Crack path No.2014030605

(f) Crack path No.2014030606

FIGURE 2.30: Crack path in rectangular ice specimen with a wedge and pre-crack Group 3

open. So both types of specimens were used. And the specimens with different lengths in the range of $120 \sim 230mm$ were tried in order to get a higher strain rate. The experimental parameters are listed in appendix A, Tab.A.15. The strain rate increases which the length decreases. Then, another group with the same approximate length $120mm$ is used, the experimental parameters are listed in appendix A, Tab.A.19.

Through the previous practice, the impact velocity was well controlled. $2m/s$ is the critical impact velocity for a main crack initiation and propagation in ice. The small scatter may be due to the micro-structure of the specimen and the bluntness of the pre-crack tip.

The crack propagates along the direction of the pre-crack in five experiments. In the others, the crack propagation direction changes without regularity. For the specimen with a hole, the compression is converted into the traction. During the process, the defects in the specimen affect the stress distribution more strongly than for the specimen with notch.

The drawback of this group experiment is the quality of the images which is too poor to distinguish the crack initiation. The fog which formed between the three-layer glass window reduced the quality of the images dramatically.

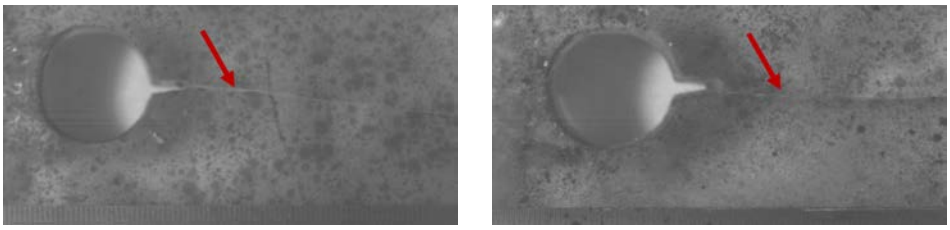

(a) Crack path No.2014102106 (b) Crack path No.2014102107

FIGURE 2.31: Crack path in rectangular ice specimen with a notch and pre-crack

2.6 Conclusion and recommendations

This chapter presented a series of experiments for investigating the dynamic behaviour of ice under impact loading using the Split Pressure Hopkinson bars. Even if the experiments were difficult to perform : in the preparation of specimens, in the control of impact loading to get a unique crack propagation, in the capture of high quality images. We managed to find preliminary results about the dynamic behaviour of ice.

I- With the SHPB signals the dynamic stress-strain behaviour has been obtained. The peak stress is in the range of $1.5MPa \sim 8.0Mpa$ and increases with the impact velocity in the range of $0.5 \sim 6.0m/s$. When the impact velocity is controlled at the critical value the fracture appears, the dynamic Young's modulus is $4GPa$ which is prepared for the following simulation.

II- The cylindrical specimen fracture mode with several axial cracks is observed with the help of the high speed camera. With the impact velocity larger than $2m/s$, the crack initiates once it is impacted by the input bar and propagates from the input bar side, then the opposite direction cracks appear. Finally, the radial cracks may happen. With the impact velocity near to $2m/s$, the crack initiates until the stress wave reach the output bar and reflects and propagates from the output bar side. The crack propagation velocity is about $500m/s$.

III- In the well controlled experiments with the rectangular specimen, a main crack propagates in Mode I along the pre-crack in the horizontal direction, and finally the specimen separates into two main parts. The crack initiation is hard to distinguish by naked-eyes, therefore the image analysis methods will be introduced.

Despite our efforts, most experiments failed due first to bad image quality and also to irregular crack paths.

With the purpose of increasing the image quality, one solution is to employ a larger chamber which can contain the lamps inside it to improve the lightening. The other solution is to design vacuum interlayer window to achieve insulation and prevent frost patterned on the glass when the temperature decreases. The preparation of the speckles used for DIC needs also be improved.

The irregular crack paths may be due to the specimen geometry and its preparation, the contact between bar and specimen. The small change in the specimen geometry and the partial poor contact conditions can unbalance the stress distribution, which may explain why the crack is not propagating along the pre-crack direction. The presence of defects within the ice may also affect the crack propagation.

Chapter 3

Evaluation of crack generation and propagation by image analysis

This chapter will introduce image analysis methods in our investigation. First, the digital image is analysed based on the grey scale. The crack tip position is located, the crack path is observed and the crack propagation velocity is measured. Then the image correlation method is used to extract the displacement and strain fields although it lags behind the grey scale method in evaluating the crack. According to the DIC results, we try to use the J-integrals to calculate the stress intensity factor. However, due to the bad image quality the displacement field is not accurate enough to evaluate the stress intensity factor when the crack is propagating.

Contents

3.1 Introduction

All information from the SHPB measurement technique is based on the assumption of homogeneous stress and strain fields. Unfortunately, for the crack propagation problem, the area of interest is the vicinity of the crack tip where the stress field has singularity. Local displacement and strain fields measurement are needed. The high-speed photography technique as a non-contact method was used to capture the crack propagation process.

From the images, it was hard to observe the crack initiation and propagation by naked eyes. Then, the image analysis method was used to locate the crack tip position and evaluate the crack propagation. The crack path was enhanced by subtracting an image from the previous one, and the crack tip was located and crack propagation velocity was measured.

The digital image correlation was used to extract the displacement and strain field. After, the displacement field was used to estimate the stress intensity factor which is the most important feature to evaluate the crack propagation.

3.2 Digital images

All information from the SHPB measurement technique is based on the assumption of homogeneous stress and strain fields. Unfortunately, for the crack propagation problem, the area of interest is in the vicinity of the crack tip where the stress field has singularity. Local displacement and strain fields measurement are needed. The high-speed photography technique as a non-contact method is used to locate the crack tip position and evaluate the crack propagation.

3.2.1 Image recording parameters

The high speed camera used in our experiment to record the experimental process is a Phantom v710 camera as shown in Fig.3.1. It can deliver 7350 frames per second (fps) in the resolution of 1280×800. A high frame rate is essential for dynamic experiment. It can be obtained by reducing the resolution to a lower value. In our experiment, the crack propagates along the pre-crack in the horizontal direction. Therefore, the height of the area of interest was reduced for obtaining a high frame rate. The trigger signal can be an external TTL pulse (hardware produced). A Multi-Channel Data Link (MCDL) box was used to supply the pulse and then the synchronization between the SHPB signals and camera were established.

3.2.2 Experimental digital images

A typical experiment is presented below. The image recording parameters are listed in Tab.3.1. The high speed camera focused on the specimen and recorded transformations of the specimen

during impact. An example is given in Fig.3.2 where 9 consecutive images show the crack propagation within the ice specimen. The duration of the crack propagation is about 216μs. The main crack propagates in Mode I along the pre-crack in the horizontal direction, and finally the specimen separates into two main parts.

At 216μs, the crack has already propagated to the end of the area of interest, but the crack path is hard to observe with naked-eyes. Therefore, the image analysis are needed to locate the crack tip.

3.3 Grey scale

3.3.1 Principle of grey scale

The image recorded by high speed camera is a grey-scale digital image. It contains a fixed number of rows and columns of pixels. Pixels are the smallest individual element in an image, hold quantized values that represent only intensity information at any specific point varying from black at the weakest intensity to white at the strongest [Johnson, 2006]. Therefore the images can be taken as grey scale matrices carrying out mathematical calculations.

FIGURE 3.1: High speed camera phantom v710

Number	2014030603
Resolution	512×344
Frame rate (fps)	37016
Interval (μs)	27
Exposure (μs)	14

TABLE 3.1: Image recording parameters for a typical experiment No.2014030603

3.3.2 Evaluation crack generation and propagation

The images as grey-scale matrices were used to evaluate the crack tip position and the crack path. The image contrast was enhanced by subtracting the gray-scale matrix of an image from the previous one, if the crack propagated during the interval time of the two images, because of a low level of deformation, a difference appeared and could be taken as a crack path. The results are shown in Fig.3.3. In the first image, nothing is visible. From the second to the eighth image, obvious differences appear which are considered as a crack propagation. The crack tip locations are estimated for each image. The length of the crack propagation at each interval of $27\mu s$ is measured, thereby the crack propagation velocity is evaluated. The whole crack path can be obtained by subtracting the first image from the last one as shown in the 9^{th} image.

3.4 Digital image correlation

3.4.1 Principle of digital image correlation

The digital image correlation method was also used to analyse the images. As a non-contact measurement technique to obtain the displacement and strain fields in an interesting area, it was

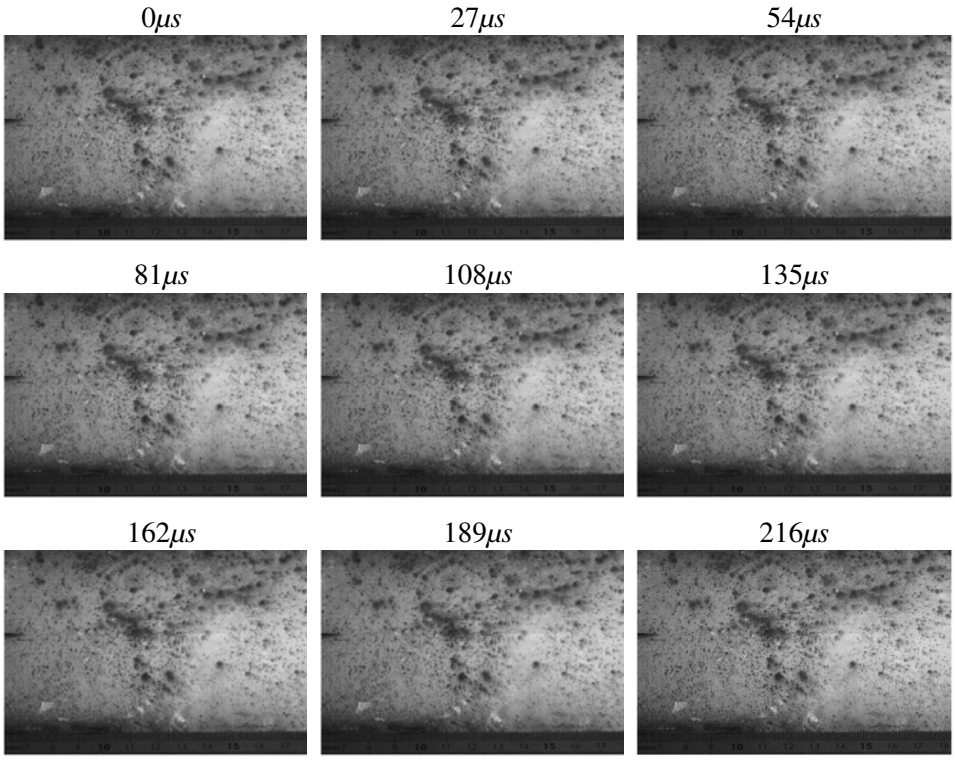

FIGURE 3.2: Crack propagation images from a rectangular ice specimen

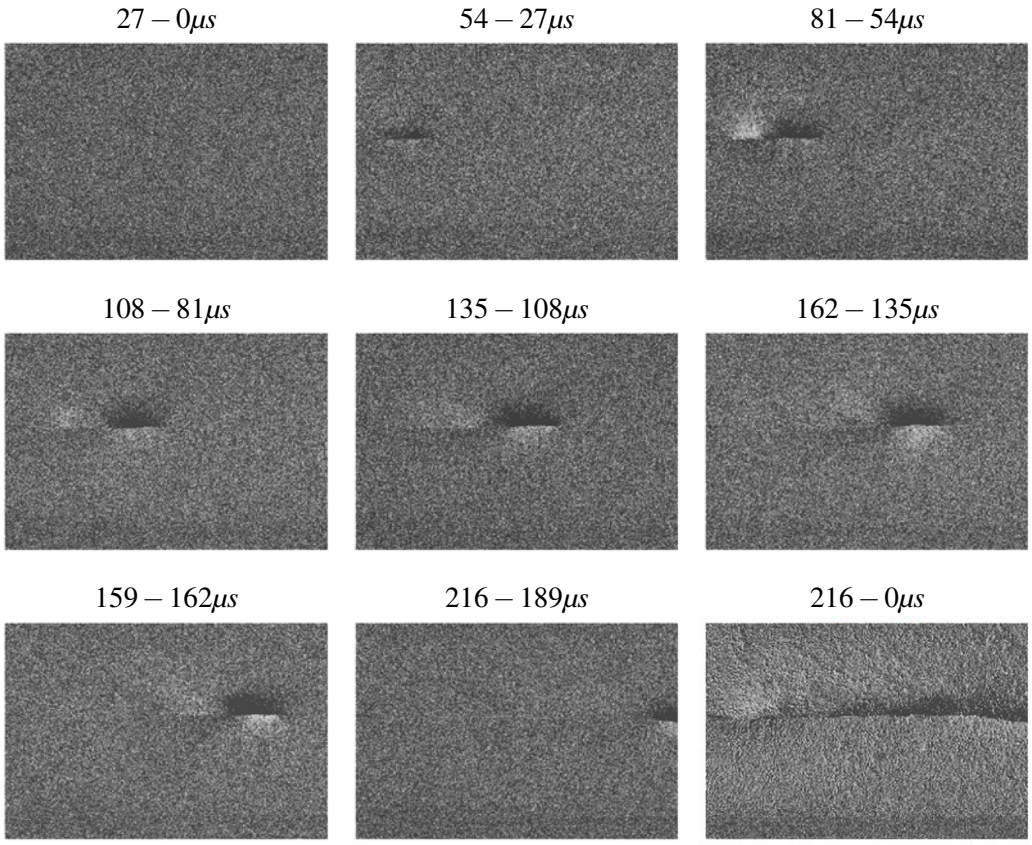

FIGURE 3.3: Crack propagation path extracted by subtracting one image from previous one

firstly introduced by Peters and Ranson [Peters and Ranson, 1982].

Before the experiment, a random speckle pattern on the surface of the specimen was prepared.

During the experiment, an image was captured before loading as the reference image and subsequent images were captured as the deformed images corresponding to the loading process. A series of images is shown in Fig.3.4.

Before analysis, an area was chosen as the interesting area, and a small square subset was defined. The size of the subset was determined by the quality of the image and the speckle pattern on the surface of the specimen. As a general rule, larger subset sizes increase the accuracy whereas a smaller subset increase the resolution.

During the analysis, each subset of the reference image was sought in the deformed images based on the matching the pixel gray scale values [Roux et al., 2009]. Once the same location of a subset in the deformed image was identified, the local displacements could be quantified.

Consider a series of images is recorded by high speed camera. The intensity patterns $f(x,y)$ and $f^*(x^*,y^*)$ correspond to the reference image and the deformed image respectively as described in Eq. 3.1. They are assumed to be one-to-one correspondence in the deformed image.

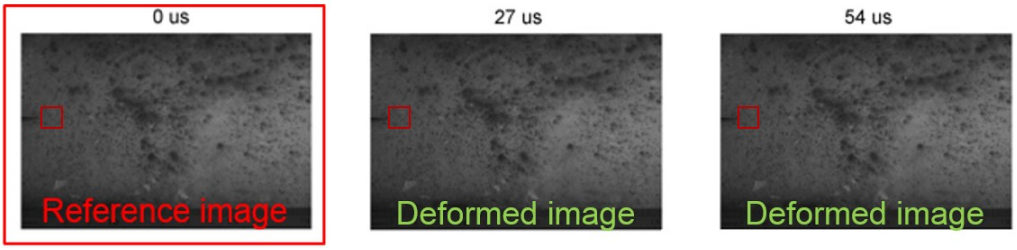

FIGURE 3.4: Reference and deformed images

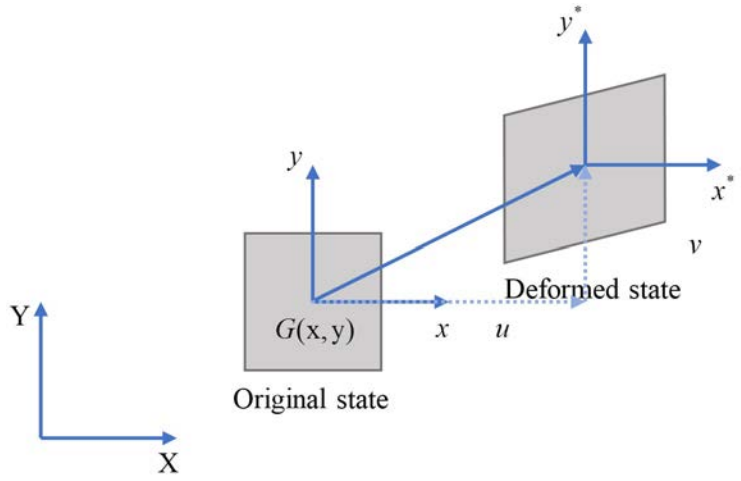

FIGURE 3.5: Concept of digital image correlation

$$f^*(x^*,y^*) - f(x+u(x,y),y+v(xy)) = 0 \tag{3.1}$$

Where $u(x,y)$ and $v(x,y)$ represent the displacement components of the reference subset center in an x and y coordinate system. Assume that point is G. The matching procedure is to find the corresponding subset centered at P^* in the deformed image in the x^* and y^* coordinate system as shown in Fig.3.5. The criterion is the subset in deformed image has the maximum similarity with the reference image. Consequently, two images are corresponding by the two central points G and G^*. The point G^* is expressed by Eq.3.2.

$$x^* = x + u(x,y)$$

$$y^* = y + v(x,y) \tag{3.2}$$

The displacement fields can be approximated using the Taylor series around a point $G(x_0,y_0)$

with Eq.3.3.

$$x^* = x + u + \frac{\partial u}{\partial x}\Delta x + \frac{\partial u}{\partial y}\Delta y + \frac{1}{2}\frac{\partial^2 u}{\partial x^2}\Delta x^2 + \frac{1}{2}\frac{\partial^2 u}{\partial y^2}\Delta y^2 + \frac{\partial^2 u}{\partial x \partial y}\Delta x \Delta y$$

$$y^* = y + v + \frac{\partial v}{\partial x}\Delta x + \frac{\partial v}{\partial y}\Delta y + \frac{1}{2}\frac{\partial^2 v}{\partial x^2}\Delta x^2 + \frac{1}{2}\frac{\partial^2 v}{\partial y^2}\Delta y^2 + \frac{\partial^2 v}{\partial x \partial y}\Delta x \Delta y \tag{3.3}$$

where v and u are the vertical and horizontal displacements, $\Delta x = x - x_0$ and $\Delta y = y - y_0$.

To evaluate the similarity between the reference and the deformed images, a correlation coefficient should be predefined and computed. Here, a correlation coefficient is introduced in Eq.3.4.

$$C = \frac{\sum_S [f(x,y) - f^*(x^*,y^*)]^2}{\sum_S f^2(x,y)} \tag{3.4}$$

Where S is the subset used for calculation, f and f^* are the grey scale light intensities corresponding to all the points in the subset of the reference image and deformed images respectively.

In order to improve the displacement fields, the correlation coefficient is minimized. The optimal displacement field consists with the minimum of the correlation coefficient.

More details about the principle of DIC can be found in the references [Chu et al., 1985] [Pan et al., 2009].

3.4.2 Evaluation crack generation and propagation

The displacement fields from the same experiment were estimated by image correlation as shown in Fig.3.6 and Fig.3.7.

The displacement fields in X direction do not supply useful information. The displacement fields in Y direction shows the specimen is separated into two main parts following the impact loading. The top part is with positive displacement and the bottom part with negative displacement.

Then the strain fields were extracted from the displacement fields. The strain fields ε_{xx} and ε_{yy} during the crack propagation are shown in Fig.3.8 and Fig.3.9, respectively.

The displacement field along X illustrates that no sliding happens between the top and bottom parts, since no discontinuity can be observed. One may conclude that the main crack does not propagate as Mode II.

The crack path can be observed obviously in the strain filed ε_{yy}. It demonstrates that the crack propagates in Mode I.

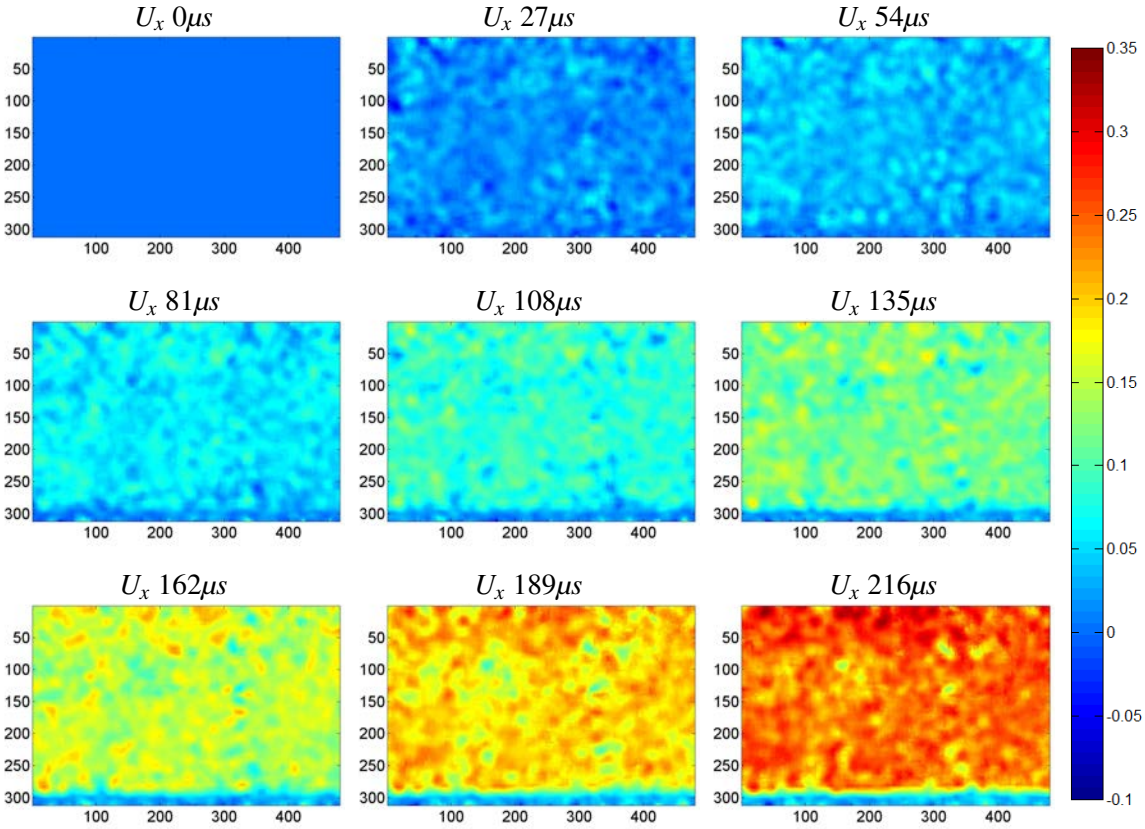

FIGURE 3.6: Horizontal displacement U_x measured by DIC (mm)

It is difficult to identify the crack path from strain field measurement. One possibility consists in plotting strain field discontinuities. Another one is to plot the maximum values, as shown in Fig.3.10, where the crack path is clearly identified.

There the crack path and crack tip can not be evaluated in the first four images. In the image at 27μs and 54μs, it could be supposed there is not deformation on the surface of specimen, but only internal crack. In image after 81μs the dots did not merge into a line, it could be supposed the deformation occurred but hard to identify a recognized crack. After 108μs, a recognized crack appeared, the precise location of the crack tip is still difficult to identify. The most part of crack path can be recognized at 216μs, and confirms that there is only one main crack.

By DIC, the most part of crack path is distinguished, but crack tip location is hard to define at different times. The possible reason is that the speckles on the surface of the specimen was not good enough which makes the displacement field discontinuity.

All the DIC processing was performed with VIC 2D.

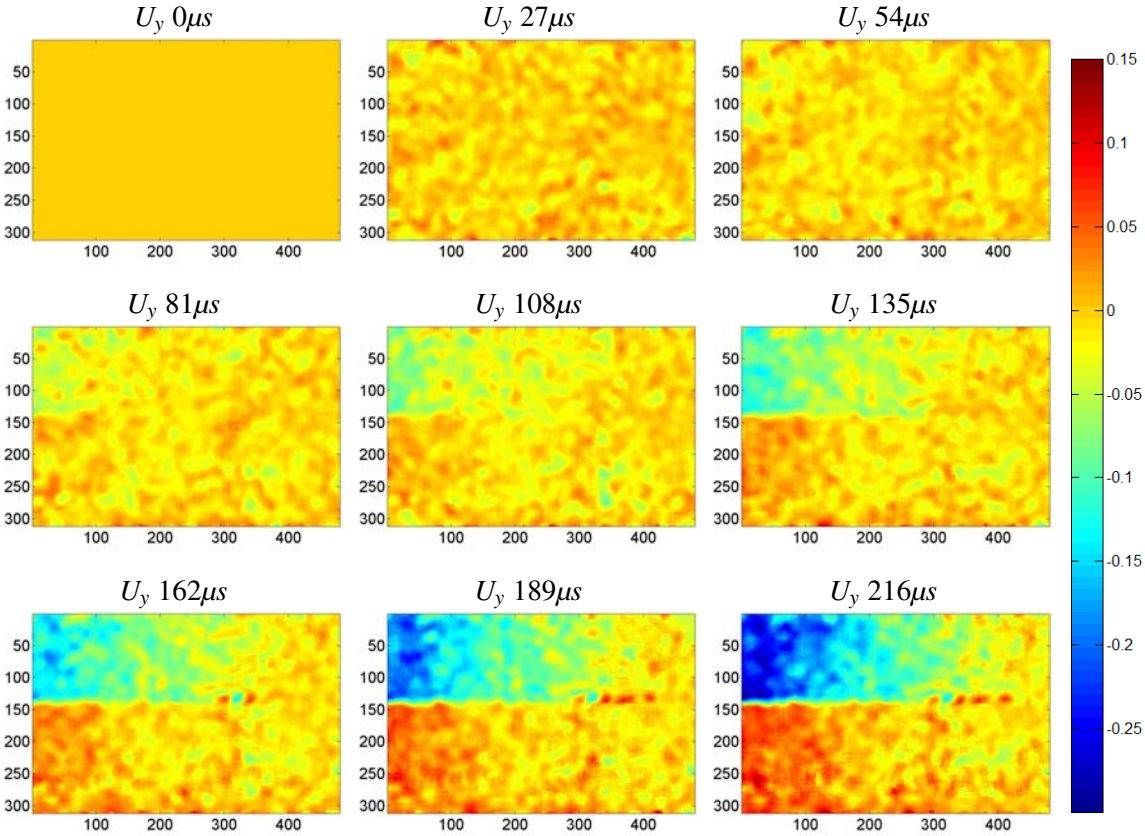

FIGURE 3.7: Vertical displacement U_y measured by DIC (mm)

3.4.3 Evaluation SIFs by the J-integrals

The stress intensity factor is the most important feature to evaluate the crack propagation. In our work, we use the fracture criterion based on the stress intensity factor which was calculated from the displacement field extracted by digital image correlation by the J-integrals using an equivalent domain integral method[Raju and Shivakumar, 1990].

Consider a crack in a plate subjected to an arbitrary remote loading with an arbitrary closed contour Γ around the crack tip. Then the J-integral is defined in the absence of any body forces as

$$J_k = \int_{\Gamma} Q_k d\Gamma \tag{3.5}$$

where $k = 1,2$ and

$$Q_k = \left[W_{n_k} - \sigma_{ij} \frac{\partial u_i}{\partial x_k} n_j \right] \tag{3.6}$$

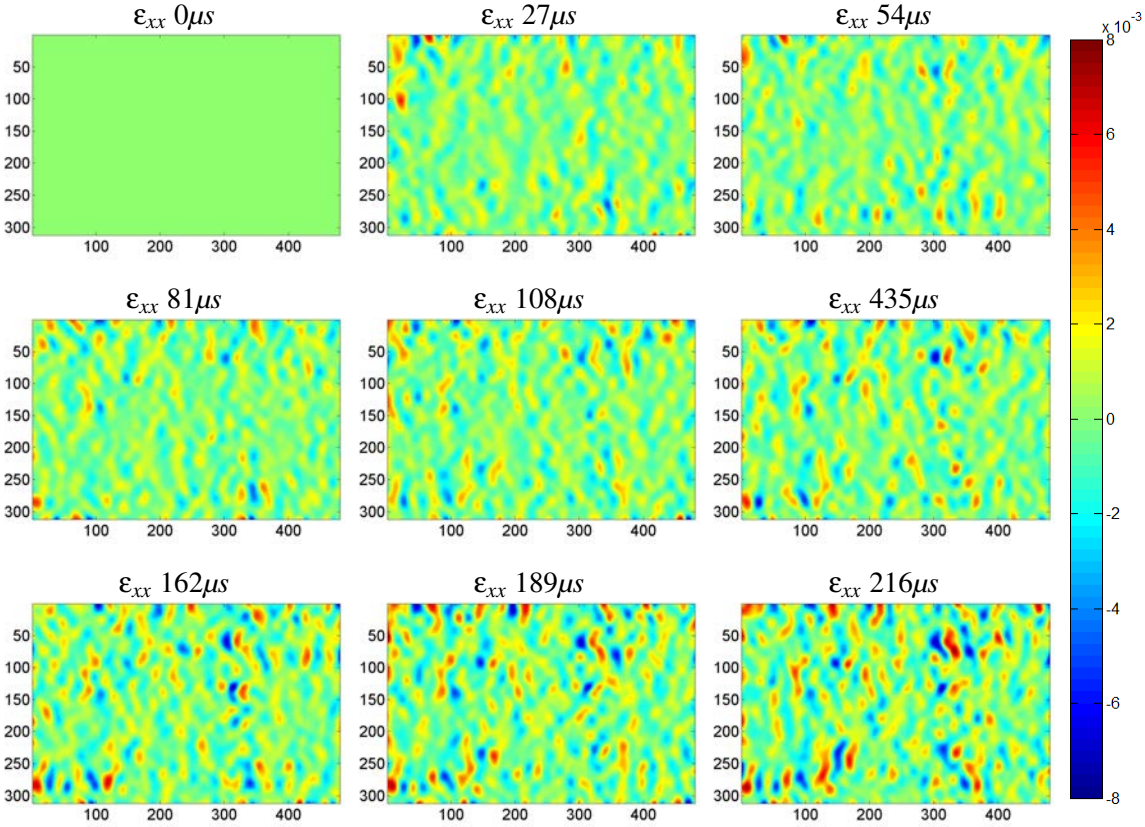

FIGURE 3.8: Strain ε_{xx} measured by DIC

W is the total strain-energy density defined as

$$W = \int_0^{\varepsilon_{ij}} \sigma_{ij} d\varepsilon_{ij} \tag{3.7}$$

An arbitrary but continuous function $S(x_1, x_2)$ is defined with the property

$$S(x_1,\ x_2) = 1 \tag{3.8}$$

$S(x_1, x_2)$ is the coordinate of the node.

on the node inside.

$$S(x_1,\ x_2) = 0 \tag{3.9}$$

on the node outside.

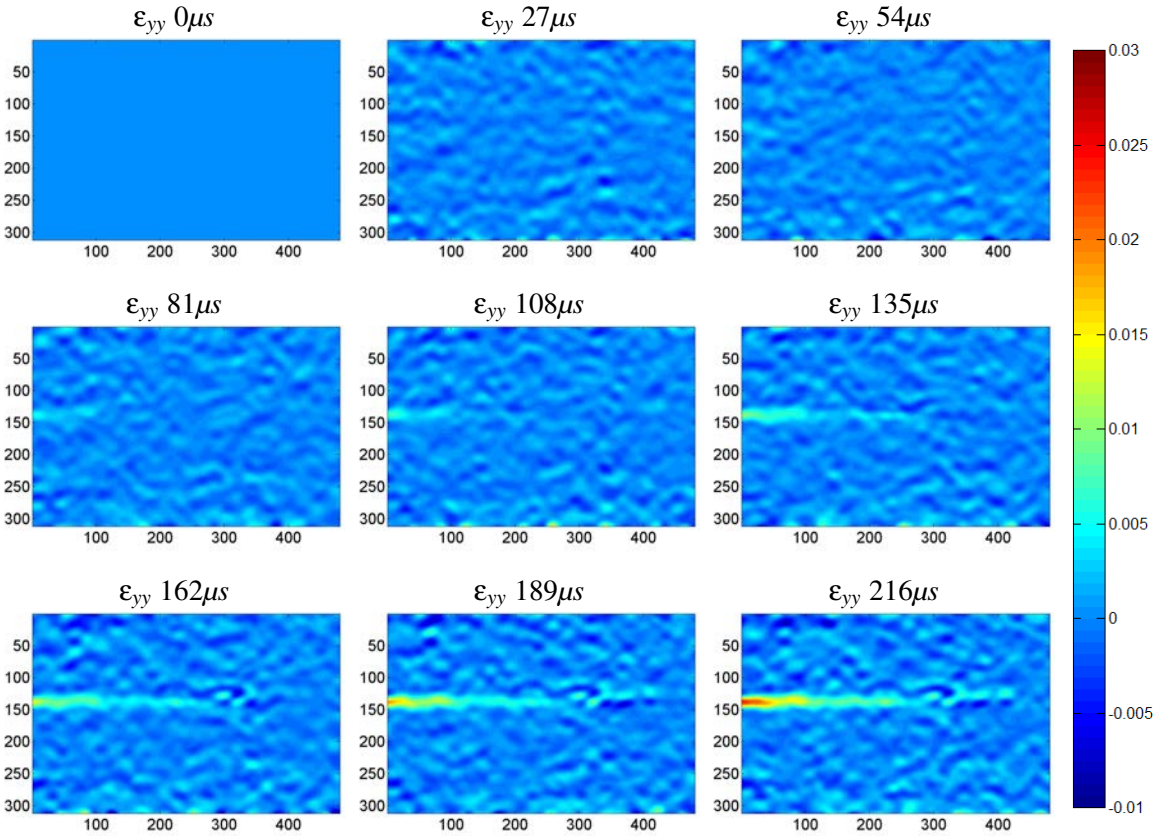

FIGURE 3.9: Strain ε_{yy} measured by DIC

Invoking the divergence theorem,

$$(J_k)_{domain} = -\int_A \left[W \frac{\partial S}{\partial x_k} - \sigma_{ij} \frac{\partial u_i}{\partial x_k} \frac{\partial S}{\partial x_j} \right] dA \tag{3.10}$$

Where A is the J-integral domain.

Rewritten in a form convenient to numerical computation as

$$(J_k)_{domain} = -\int_A \left[W \frac{\partial S}{\partial x_k} - \left\{ u'_{x_k} \right\}^T [\sigma] \left\{ S' \right\} \right] dA \tag{3.11}$$

represents the energy change per unit crack extension.

where

$$\left\{ u'_{x_k} \right\}^T = \left\{ \frac{\partial u_1}{\partial x_k} \quad \frac{\partial u_2}{\partial x_k} \right\} \tag{3.12}$$

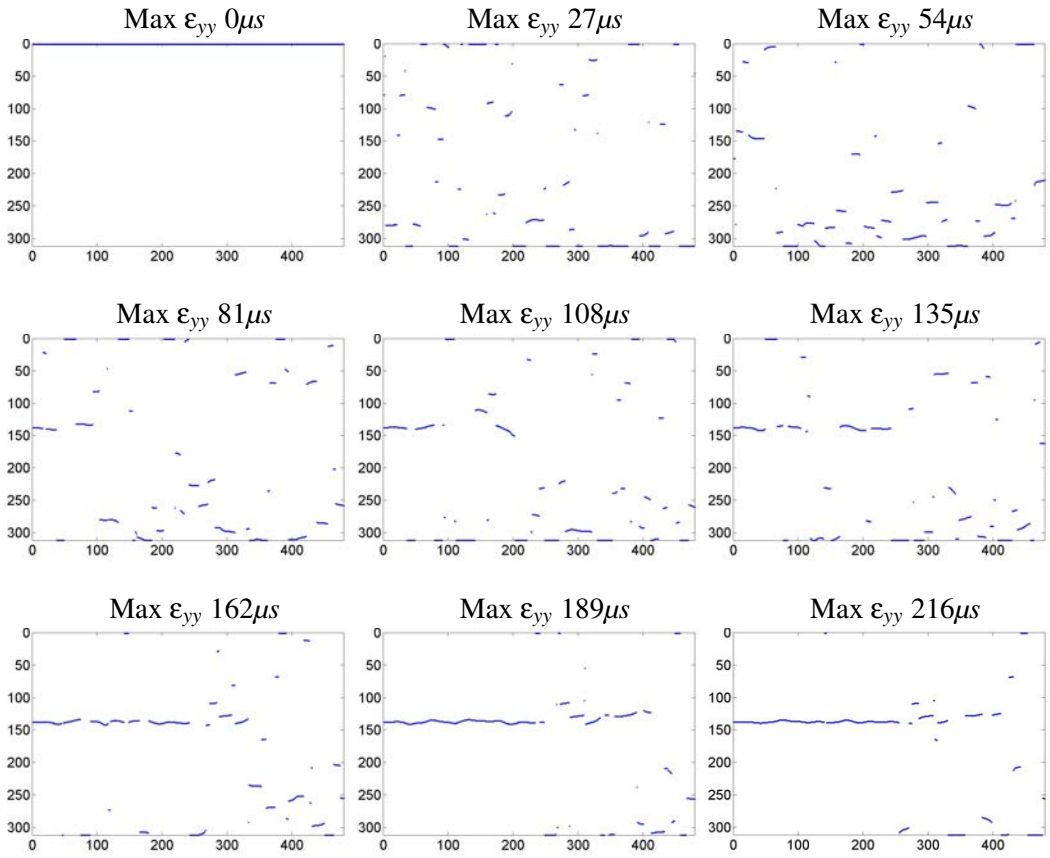

FIGURE 3.10: Maximum strain ε_{yy} measured by DIC

$$[\sigma] = \begin{bmatrix} \sigma_{11} & \sigma_{12} \\ \sigma_{21} & \sigma_{22} \end{bmatrix} \tag{3.13}$$

$$\{S'\}^T = \begin{Bmatrix} \frac{\partial S}{\partial x_1} & \frac{\partial S}{\partial x_2} \end{Bmatrix} \tag{3.14}$$

The strain-energy distribution W is

$$W = \frac{1}{2}\left[\sigma_{11}\varepsilon_{11} + \sigma_{22}\varepsilon_{22} + 2\sigma_{12}\varepsilon_{12}\right] \tag{3.15}$$

The domain integral is

$$(J_k)_{domain} = \sum_i J_{x_{k_i}} \tag{3.16}$$

where J_{k_i} is the area integral over the ith element.

In the isoperimetrical representation, the displacements within the element are defined by the

shape functions N_j and the nodal displacements

$$u_\alpha = N_j (u_\alpha)_j \tag{3.17}$$

where $\alpha = 1,2$, $N_j = N_j(\xi,\eta)$, ξ , η are the parent coordinates and $j = 1$ to the number of nodes on the element.

$$(J_{k_i})_{domain} = -\int_{-1}^{1}\int_{-1}^{1} W \frac{\partial S}{\partial x_k} - \left\{u'_{x_k}\right\}^T [\boldsymbol{\sigma}] \left\{S'\right\} (det\,[\boldsymbol{J}]) d\xi d\eta \tag{3.18}$$

The area integral $J_{x_{k_i}}$ of the ith element can be computed using Gaussian quadrature as

$$(J_{k_i})_{domain} = -\left[\sum_{m=1}^{M_G}\sum_{n=1}^{M_G}\left[W\frac{\partial S}{\partial x_k} - \left\{u'_{x_k}\right\}^T [\boldsymbol{\sigma}]\left\{S'\right\}\right] w_m w_n (\det[\boldsymbol{J}])\right] \tag{3.19}$$

where M_G is the number of Gaussian quadrature points used in each direction ξ and η ,w_m and w_n are the Gaussian weights and det[J] is the determinant of the Jacobian matrix [J].

S function is defined using the element shape functions

$$S(\xi,\eta) = N_j S_j \tag{3.20}$$

In our case, the (x,y,O) coordinate is established according to the image. The crack tip is signed with a red point located by grey scale or image correlation, respectively as shown in Fig.3.11.

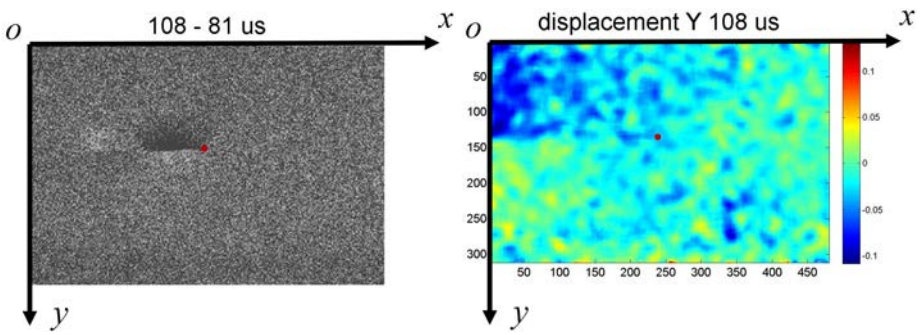

FIGURE 3.11: Coordinate system established by images for J-integral

x^e and y^e are the Cartesian coordinates of each element with 4-nodes. u^e and v^e are the X and the Y displacements. All these values are from digital image correlation results. S^e is S function described as before, at the node (the blue point) inside the integral zone, $S^e = 1$, at the node (the grey point) outside the integral zone, $S^e = 0$ as shown in Fig.3.12.

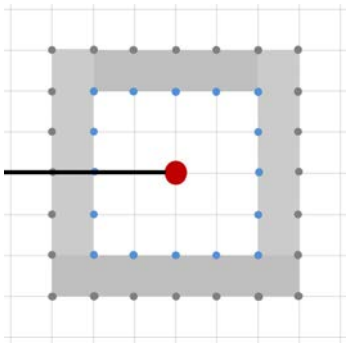

FIGURE 3.12: 6 pixel $\times$ 6 pixel J-integral zone centred with crack tip

$$\boldsymbol{x^e} = \begin{Bmatrix} x_1^e \\ x_2^e \\ x_3^e \\ x_4^e \end{Bmatrix}, \boldsymbol{y^e} = \begin{Bmatrix} y_1^e \\ y_2^e \\ y_3^e \\ y_4^e \end{Bmatrix}, \boldsymbol{u^e} = \begin{Bmatrix} u_1^e \\ u_2^e \\ u_3^e \\ u_4^e \end{Bmatrix}, \boldsymbol{v^e} = \begin{Bmatrix} v_1^e \\ v_2^e \\ v_3^e \\ v_4^e \end{Bmatrix} \tag{3.21}$$

according to the element position to the integral domain, S^e is different.

$$\begin{aligned} S_1^e &= [0.0; 0.0; 1.0; 0.0] \\ S_2^e &= [0.0; 0.0; 1.0; 1.0] \\ S_3^e &= [0.0; 0.0; 0.0; 1.0] \\ S_4^e &= [1.0; 0.0; 0.0; 1.0] \\ S_5^e &= [1.0; 0.0; 0.0; 0.0] \\ S_6^e &= [1.0; 1.0; 0.0; 0.0] \\ S_7^e &= [0.0; 1.0; 0.0; 0.0] \\ S_8^e &= [0.0; 1.0; 1.0; 0.0] \end{aligned} \tag{3.22}$$

The shape function is defined as

$$\begin{aligned} N_1(r,s) &= \frac{1}{4}(1-r)(1-s) \\ N_2(r,s) &= \frac{1}{4}(1+r)(1-s) \\ N_3(r,s) &= \frac{1}{4}(1+r)(1+s) \\ N_4(r,s) &= \frac{1}{4}(1-r)(1+s) \end{aligned} \tag{3.23}$$

Partial derivatives of shape function

$$\begin{aligned} N_{1,\,r} &= -\frac{1}{4}(1-s) \quad N_{1,s} = -\frac{1}{4}(1-r) \\ N_{2,\,r} &= \frac{1}{4}(1-s) \quad\;\; N_{2,s} = -\frac{1}{4}(1+r) \\ N_{3,\,r} &= \frac{1}{4}(1+s) \quad\;\; N_{3,s} = \frac{1}{4}(1+r) \\ N_{4,\,r} &= -\frac{1}{4}(1+s) \quad N_{4,s} = \frac{1}{4}(1-r) \end{aligned} \tag{3.24}$$

$$\begin{aligned} x_r &= \boldsymbol{N_r x^e} \quad x_s = \boldsymbol{N_s x^e} \\ y_r &= \boldsymbol{N_r y^e} \quad y_s = \boldsymbol{N_s y^e} \end{aligned} \tag{3.25}$$

Jacobian matrix $[\boldsymbol{J}]$ defined by

$$\boldsymbol{J^e} = \begin{bmatrix} x_r & x_s \\ y_r & y_s \end{bmatrix} \tag{3.26}$$

$$\boldsymbol{N_x} = \frac{y_s \boldsymbol{N_r} - y_r \boldsymbol{N_s}}{\det(\boldsymbol{J^e})} \tag{3.27}$$

$$\boldsymbol{N_y} = -\frac{x_s \boldsymbol{N_r} + x_r \boldsymbol{N_s}}{\det(\boldsymbol{J^e})} \tag{3.28}$$

Partial derivatives of S function

$$\frac{\partial q}{\partial x} = \boldsymbol{N_x q^e} \quad \frac{\partial q}{\partial y} = \boldsymbol{N_y q^e} \tag{3.29}$$

Thus the strain is

$$\begin{aligned} \varepsilon_{xx} &= \frac{\partial u}{\partial x} = \boldsymbol{N_x u^e} \\ \varepsilon_{yy} &= \frac{\partial u}{\partial y} = \boldsymbol{N_x v^e} \\ \gamma_{xy} &= \frac{\partial v}{\partial x} + \frac{\partial u}{\partial y} = N_x v^e + N_y u^e \end{aligned} \tag{3.30}$$

The stress is

$$\boldsymbol{\sigma} = \boldsymbol{C\varepsilon} \tag{3.31}$$

where

$$\boldsymbol{\sigma} = \begin{Bmatrix} \sigma_{xx} \\ \sigma_{yy} \\ \tau_{xy} \end{Bmatrix}, \quad \boldsymbol{\varepsilon} = \begin{Bmatrix} \varepsilon_{xx} \\ \varepsilon_{yy} \\ \gamma_{xy} \end{Bmatrix} \tag{3.32}$$

for linear elastic plane stress

$$\boldsymbol{C} = \frac{E}{1-\nu^2}\begin{bmatrix} 1 & \nu & 0 \\ \nu & 1 & 0 \\ 0 & 0 & \frac{1-\nu}{2} \end{bmatrix} \tag{3.33}$$

The strain-energy density is

$$w = \frac{1}{2}\boldsymbol{\sigma}\varepsilon^T \tag{3.34}$$

The J integral in an element can be rewritten as

$$J = \int_A \left[\left(\sigma_{xx}\frac{\partial u}{\partial x} + \tau_{xy}\frac{\partial v}{\partial x} - w\right)\frac{\partial S}{\partial x} + \left(\tau_{xy}\frac{\partial u}{\partial x} + \sigma_{yy}\frac{\partial v}{\partial x}\right)\frac{\partial S}{\partial y}\right] dA \tag{3.35}$$

Derivation process :

$$(J_k)_{domain} = -\int_A \left[W\frac{\partial S}{\partial x_k} - \left\{u'_{x_k}\right\}^T [\boldsymbol{\sigma}]\left\{S'\right\}\right] dA \tag{3.36}$$

J_1 is usually termed the J-integral, J_2 is called the product integral. So J-integral only compute J_1. When $k = 1$

$$\begin{aligned}
(J_{x_1})_{domain} &= -\int_A \left[W\frac{\partial S}{\partial x} - \left\{u'_x\right\}^T [\boldsymbol{\sigma}]\left\{S'\right\}\right] dA \\
&= -\int_A \left[W\frac{\partial S}{\partial x} - \left\{\frac{\partial u}{\partial x} \quad \frac{\partial v}{\partial x}\right\}\begin{bmatrix} \sigma_{11} & \sigma_{12} \\ \sigma_{21} & \sigma_{22} \end{bmatrix}\begin{bmatrix} \frac{\partial S}{\partial x} \\ \frac{\partial S}{\partial y} \end{bmatrix}\right] dA \\
&= -\int_A \left[W\frac{\partial S}{\partial x} - \left\{\frac{\partial u}{\partial x}\sigma_{11} + \frac{\partial v}{\partial x}\sigma_{21} \quad \frac{\partial u}{\partial x}\sigma_{12} + \frac{\partial v}{\partial x}\sigma_{22}\right\}\begin{bmatrix} \frac{\partial S}{\partial x} \\ \frac{\partial S}{\partial y} \end{bmatrix}\right] dA \\
&= -\int_A \left[W\frac{\partial S}{\partial x} - \left(\frac{\partial u}{\partial x}\sigma_{11} + \frac{\partial v}{\partial x}\sigma_{21}\right)\frac{\partial S}{\partial x} - \left(\frac{\partial u}{\partial x}\sigma_{12} + \frac{\partial v}{\partial x}\sigma_{22}\right)\frac{\partial S}{\partial y}\right] dA
\end{aligned} \tag{3.37}$$

$$J = \int_A \left[\left(\sigma_{xx}\frac{\partial u}{\partial x} + \tau_{xy}\frac{\partial v}{\partial x} - W\right)\frac{\partial S}{\partial x} + \left(\tau_{xy}\frac{\partial u}{\partial x} + \sigma_{yy}\frac{\partial v}{\partial x}\right)\frac{\partial S}{\partial y}\right] dA \tag{3.38}$$

The J integral in an element is computed with the equation below

$$\bar{J} = \int_{-1}^{1}\int_{-1}^{1} Q(r,s)\,dr\,ds \tag{3.39}$$

$$Q(r,s) = \left[\left(\sigma_{xx}\frac{\partial u}{\partial x} + \tau_{xy}\frac{\partial v}{\partial x} - w\right)\frac{\partial S}{\partial x} + \left(\tau_{xy}\frac{\partial u}{\partial x} + \sigma_{yy}\frac{\partial v}{\partial x}\right)\frac{\partial S}{\partial y}\right]\det(J^e) \tag{3.40}$$

$\bar{J}$ is computed using Gaussian quadrature as

$$\bar{J} \approx Q(r_1,s_1) + Q(r_2,s_2) + Q(r_3,s_3) + Q(r_4,s_4) \tag{3.41}$$

Gaussian quadrature

$$\int_{-1}^{1} f(x)dx = \sum_{i=1}^{n} w_i f(x_i) \tag{3.42}$$

Gauss - Legendre quadrature

Number of points $n = 2$, Points $x_i = \pm\frac{1}{\sqrt{3}}$, weight $w_i = 1$

where,

$$\begin{aligned} r &= \left\{-\frac{1}{\sqrt{3}} \quad \frac{1}{\sqrt{3}} \quad \frac{1}{\sqrt{3}} \quad -\frac{1}{\sqrt{3}}\right\} \\ s &= \left\{-\frac{1}{\sqrt{3}} \quad -\frac{1}{\sqrt{3}} \quad \frac{1}{\sqrt{3}} \quad \frac{1}{\sqrt{3}}\right\} \end{aligned} \tag{3.43}$$

Since the stress intensity factor K_I is a very well known quantity, a relation has been established to convert the volume integral J_I to it with Eq.3.44.

$$K_I = \sqrt{E^* \cdot J} \tag{3.44}$$

Where,

$$\begin{cases} E^* = E & plane\ stress \\ E^* = \dfrac{E}{1-\nu^2} & plane\ strain \end{cases} \tag{3.45}$$

The present problem can be considered a plane stress problem.

The stress intensity factors in a narrow band at different times of the typical experiment *No*.2014030603 are plotted in Fig.3.13.

Due to the difficulty of maintaining speckles on the surface of a specimen and lightening issues in the cooling chamber, the displacement field established by digital image correlation was not accurate enough to evaluate the stress intensity factors when the crack is propagating. The values in different images scattered a lot and were meaningless.

The SIF is estimated by MATLAB with the displacement from VIC 2D .

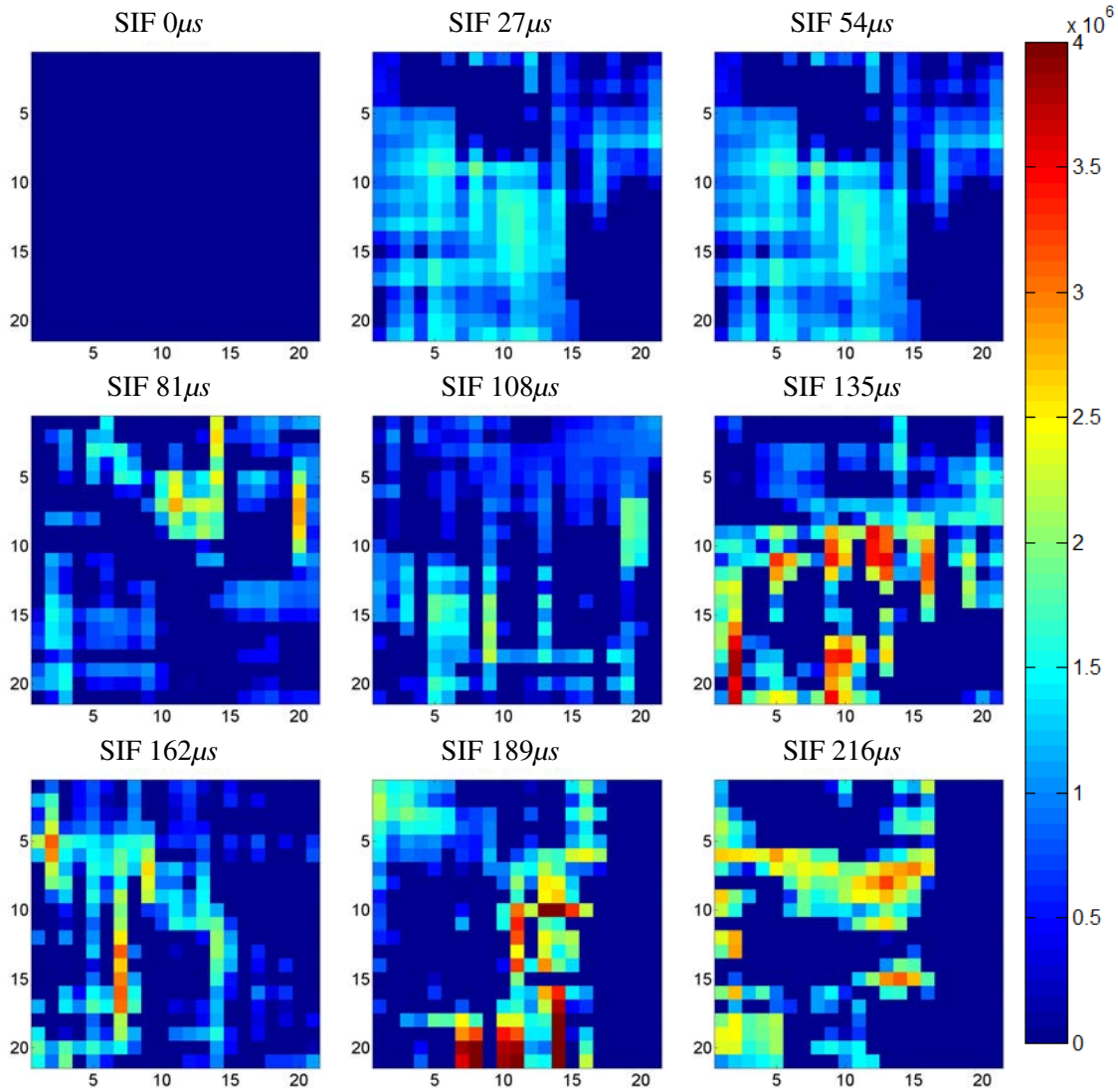

FIGURE 3.13: SIFs evaluated by J-integral, $(Pa \cdot \sqrt{m})$

3.5 Results

3.5.1 Comparison between the two methods

First, two methods are compared in distinguishing the crack tip. The area near to the pre-crack is defined as the area of interest as shown in Fig.3.14. At 54μs, it is hard to observe the change by naked eyes. Then the maximum ε_{yy} strain component obtained by DIC method and the subtracted image are shown in Fig.3.15. The crack tip can be defined in the subtracted image at 54μs, but until 108μs, the similar path appears in the DIC results.

Then, two methods are compared in distinguishing the crack path as shown in Fig.3.16. At

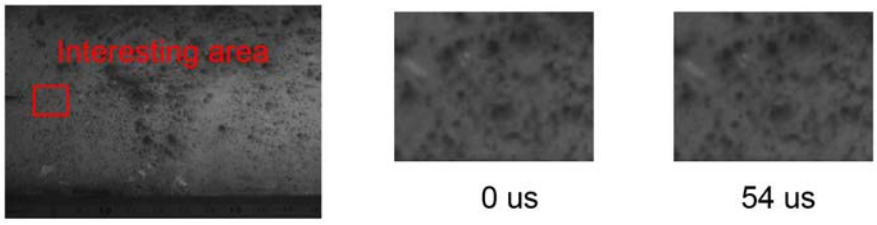

FIGURE 3.14: Area of interest near to pre-crack

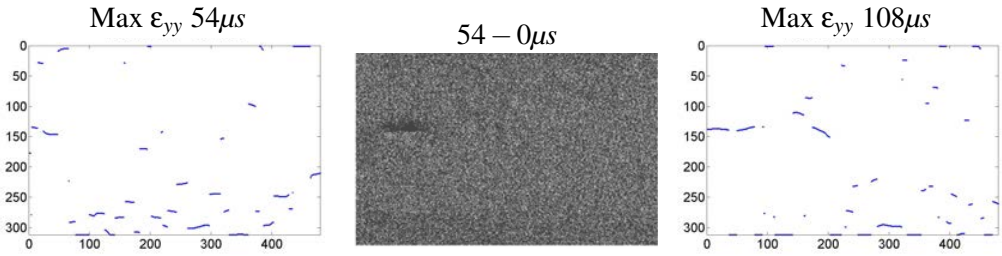

FIGURE 3.15: Evaluation crack tip by strain from DIC and difference from subtracting images

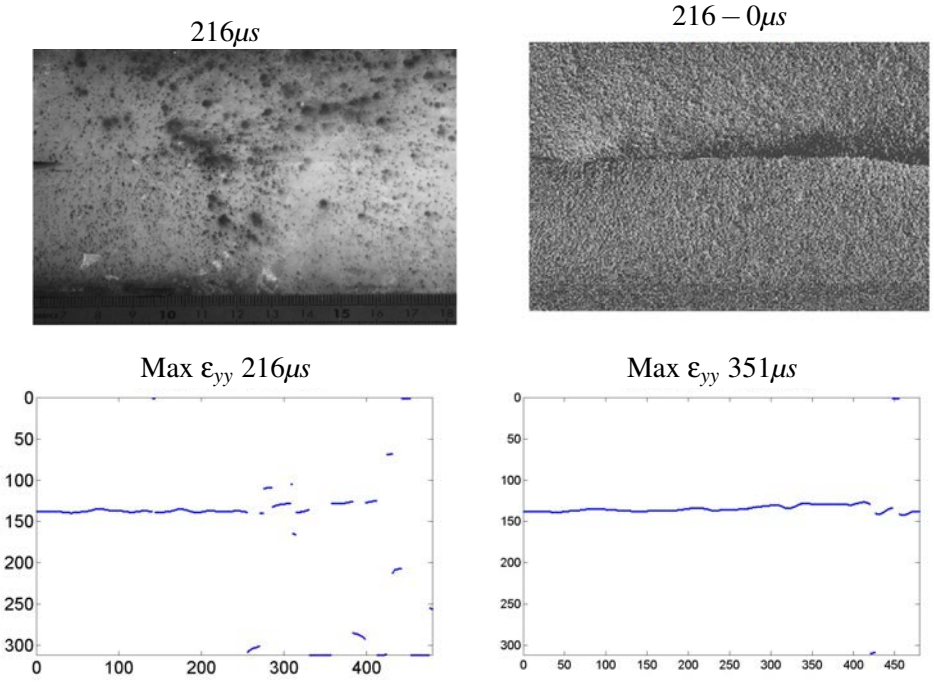

FIGURE 3.16: Evaluation crack path by original image, difference image and maximum strain field

216μs, the crack path is detected by image grayscale subtraction. Until 351μs, the whole crack path is finally distinguished by image correlation. The Crack propagates as Mode I along the pre-crack in horizontal direction.

Number	2014030603	2014030604	2014030605
Length (mm)	230	229	227
Width (mm)	90	90	90
Hight (mm)	33	32	27
Impact velocity (m/s)	2.27	1.89	1.51
Temperature $(^{\circ}C)$	-1	-1	-1

TABLE 3.2: Data for impact tests with rectangular specimens with a notch

The DIC results lag behind the directly subtracted images. It may be attributed to two main reasons.

First, the ice specimen is about $30mm$ in thickness. In the very beginning, the crack initiates internally and does not reach into the surface, no deformation appears or the deformation is too small to be detected. Therefore, the subtracted image can show the difference inside the specimen. But the DIC method is based on the deformation of the surface and it can not give useful results.

Second, due to the bad lightening, the images is not precise enough for distinguish the crack tip by DIC method.

Since the precise location of the crack tip is difficult to identify by DIC method. The attempt to evaluate the stress intensity factor by DIC is irrealizable for the crack propagation in ice under impact loading.

The crack tip can be more easily detected by Image grayscale subtraction.

3.5.2 Crack propagation velocity

Crack propagation velocities measured by image subtraction are shown in Fig.3.17. The experimental conditions are listed in Tab.3.2, Tab.3.3 and Tab.3.4. The crack propagation velocity varies with the crack length. It firstly increases and then keeps at a constant value. Afterwards, it decreases. It reaches $534 \pm 83m/s$, which is about 25% of the Rayleigh wave velocity in ice $(2000m/s)$. This velocity is the crack propagation velocity in the area of interest not the whole specimen. Usually the area is chosen from the end of the pre-crack to the end of the specimen. The interaction between the specimen and the output bar cannot be ignored. Therefore the crack propagation velocity at the end of the specimen is not considered. Meanwhile the crack bifurcation decreases the velocity, the value after the crack bifurcation is also not analyzed.

Petrenko [Petrenko and Gluschenkov, 1996] gave the average crack propagation velocity in laboratory-grown ice in the range of $100 \sim 1320m/s$ with a strain rate of $10^{-3}s^{-1}$. He explained that the large scatter was due to the grain boundaries and crystallographic orientation in ice and

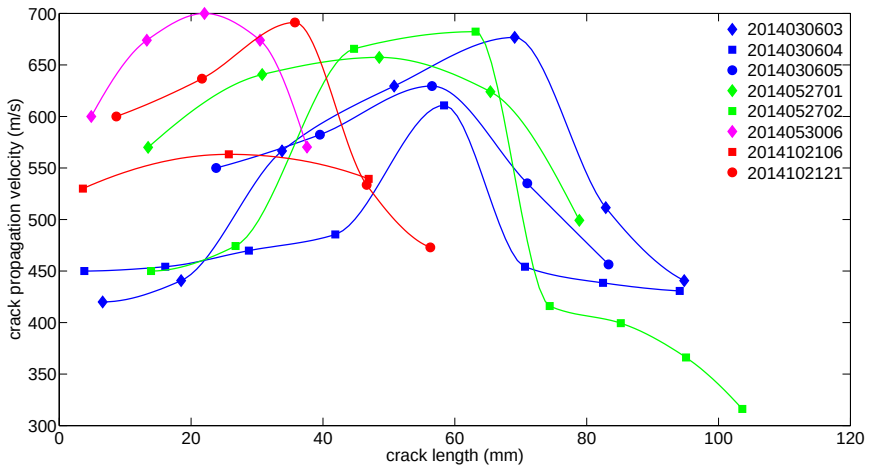

FIGURE 3.17: Crack propagation velocity vs. crack length

Number	2014052701	2014052702
Length (mm)	225	223
Width (mm)	90	90
Hight (mm)	35	30
Impact velocity (m/s)	3.66	3.49
temperature (°C)	-8	-1

TABLE 3.3: Data for impact tests with long rectangular specimens with a hole

Number	2014053005	2014053006	2014102106	2014102121
Length (mm)	118	129	112	111
Width (mm)	90	90	75	73
Hight (mm)	27	29	23	22
Impact velocity (m/s)	2.86	2.87	2.60	3.77
temperature (°C)	-1	-1	-15	-15

TABLE 3.4: Data for impact tests with short rectangular specimens with a hole

indicated that the non-uniform propagation velocity in crack growth was noticeable but much less pronounced. In our experiments, the crack propagation velocity over the crack length are reported. Due to the quality of the images, the crack propagation length in each interval is not very accurate, however it is sufficient enough to demonstrate the tendency over the crack length.

Combescure [Combescure et al., 2011] reported the crack propagation velocity in cylindrical ice projectile slowed down between $300 \pm 75 m/s$ with a mean strain rate around $30 s^{-1}$ and indicated the deceleration was due to the bifurcation. Comparing with our experiments, the mean strain rate is in the same magnitude $(10 \sim 40 s^{-1})$, the higher crack propagation velocity can be caused by keeping only one main crack propagating and avoiding the bifurcation.

Gagnon [Gagnon, 2003] measured the crack propagation velocity in the $0 \sim 550 m/s$ range in a thick-edge-loaded freshwater ice sheet and indicated the crack jump velocities were generally the highest at the beginning of the test. Due to the fact that our dimensions are much smaller, our value can be taken as the beginning one. The crack propagation velocity in ice measured from our experiments is close to the value reported by Gagnon.

3.6 Conclusion and recommendations

This chapter introduced two image analysis methods used in our investigation to evaluate the crack propagation, the grey-scale concept and digital image correlation. The crack propagation in ice under impact loading was described by image analysis.

I- After the impact, the ice specimen is separated into two main parts. The crack propagates in Mode I. The crack tip position is located, the crack path is observed and the crack propagation velocity is measured. The crack propagation velocity firstly increases and then keeps at a constant value. Afterwards, it decreases. It reaches $534 \pm 83 m/s$, which is about 25% of the Rayleigh wave velocity in ice $(2000 m/s)$.

II- The digital image correlation lags behind the subtracting grey scale directly in evaluating the crack propagation.

We have tried to use the displacement field extracted by DIC to calculate the J-integrals. However, due to the bad image quality the displacement field is not accurate enough to evaluate the stress intensity factor when the crack is propagating. A numerical method is needed to evaluate the crack propagation and will be introduced in the next chapter.

Chapter 4

Numerical study on crack propagation

This chapter introduces the numerical method to assess dynamic crack propagation criteria. The eXtended Finite Element Method(XFEM) is used to simulate the fracture processes. In the simulation, a crack is represented by two level sets, SIFs are evaluated by volume integrals. When the simulation fits the experiment, the crack initiation toughness and the crack growth toughness can be evaluated from the simulation results. The factors that influence the fracture toughness are found, and the relationship between the crack growth toughness and crack propagation velocity is established.

Contents

4.1 Introduction

As the digital image correlation was not able to evaluate the stress intensity factor due to the quality of the image, the speckles on the specimen and the illumination condition. Numerical simulations were used to access the dynamic crack criteria of propagation as a complement.

Because of the advantages on analysing the crack propagation problem, the extended finite element method was chosen to simulate the crack propagation.

The simulation was conducted by CAST3M software with a 2D model. The specimen with the input and output bars of SHPB set-up was simulated. But only the specimen was meshed.

The stress intensity factor of ice under impact loading was estimated when the simulation fitted the experiment. The crack initiation and growth toughness were evaluated according to the synchronization of the signals and images from experiments and the results from simulation. The influence factors such as crack propagation velocity, the rate of increase of stress intensity factor were discussed.

4.2 Extended finite element method

4.2.1 Advantages of XFEM in crack problem

The extended finite element method(XFEM) was chosen to simulate the test process because it has a lot of advantages on analysing crack propagation problem compared to the other numerical methods. First, the crack surface and crack front are completely independent of the mesh and therefore remeshing is not needed when the crack propagates. Second, the crack surface is constructed in terms of nodal values by additional basis functions especially combined with level sets, instead of being located on element edges, which simplifies the model. Furthermore, the singular stress field in the vicinity of crack tip is solved with enrichment functions, and the requirement of refinement is reduced [Belytschko et al., 2009].

4.2.2 Basic XFEM approximation

Considering a finite element model of a homogeneous, elastic cracked body is shown in Fig.4.1. The set of all nodes in the classical finite element mesh is denoted by S, the set of nodes of elements around the crack tip is denoted by S_C and indicated by the circled nodes, the set of nodes of elements cut by the crack but except S_C is denoted by S_H and indicated by the squares. Nodes in S_C and S_H served as tip enriched and step enriched nodes, respectively [Moës et al., 1999].

The approximation of the XFEM displacement field at time t is expressed in Eq.4.1. The first item is a classical finite element approximation, the others are enrichment approximation. $N_i(x)$ is the shape function associated with node i. $b_j(t)$ are the nodal degrees of freedom corresponding to

the step function $H(\psi(x,t))$. $B_l(r,\theta)$ is used to define the span fields of the near-tip asymptotic and the $a_k^l(t)$ are corresponding nodal degrees of freedom. The crack is represented by two level sets, and $\psi(x,t)$ has opposite signs on the two sides of the crack [Moës et al., 1999][Stolarska et al., 2001].

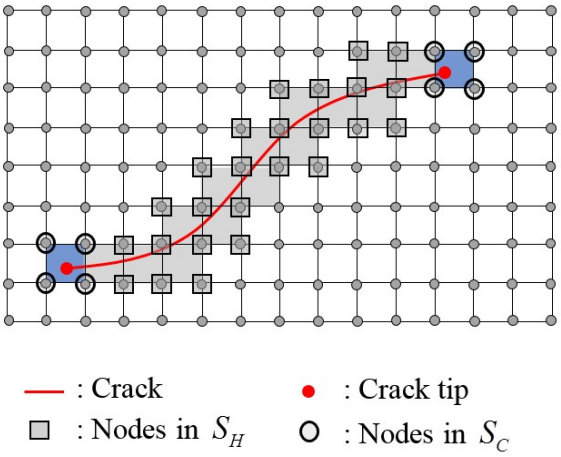

FIGURE 4.1: Enrichment to the classical finite element approximation

$$u^h(x,t) = \sum_{i\in I} u_i N_i(x) + \sum_{j\in S_H} b_j(t) N_j(x) H(\psi(x,t)) + \sum_j \sum_{k\in S_C} N_k(x) \Big(\sum_{l=1}^{4} a_k^l(t) B_l(r,\theta)\Big) \tag{4.1}$$

where $H()$ is the Heaviside step function given by Eq. 4.2. The discontinuity is defined as a crack.

$$H(f) = \begin{cases} 1, & f > 0 \\ 0, & \text{otherwise} \end{cases} \tag{4.2}$$

The branch function is defined by Eq. 4.3

$$B_l(r,\theta) = \sqrt{r}sin\frac{\theta}{2}, \sqrt{r}cos\frac{\theta}{2}, \sqrt{r}sin\frac{\theta}{2}sin\theta, \sqrt{r}cos\frac{\theta}{2}sin\theta \tag{4.3}$$

where(r,θ) is a polar co-ordinate system with its origin at the crack tip and $\theta = 0$ tangent to the crack at its tip. The above functions span the asymptotic crack tip solution of elasto-statics, and $\sqrt{r}sing\frac{\theta}{2}$ takes into account the discontinuity across the crack face.

The direction in which the crack will propagate from its current tip, θ_c, is obtained using the maximum hoop stress criteria [Dolbow and Belytschko, 1999]. The angle θ_c depends on the stress intensity factors, K_I and K_{II}, and is given by

$$\theta_c = 2\arctan\frac{1}{4}\left(\frac{K_I}{K_{II}} \pm \sqrt{\left(\frac{K_I}{K_{II}}\right)^2 + 8}\right), -\pi < \theta_c < \pi \tag{4.4}$$

4.2.3 Description of the crack by level set

The level set method (LSM) is a numerical technique developed by Osher and Sethian [Osher and Sethian, 1988] to track the motion of interfaces. In this method, an interface is modelled by a continuous function defined for each point of the space which gives the distance from the considered point to this interface. The interface is directed and distance will be counted positively or negatively according to which side of the interface lies to the point of interest [Pommier et al., 2013].

The level set method coupled with the extended finite element method to model crack growth is reported by Stolarska for the first time in two-dimensions [Stolarska et al., 2001]. Then Moës developed it into three-dimensions [Moës et al., 2002].

A level set separates a space into two zones, a positive and a negative one. For describing a crack, two level sets are needed as shown in Fig.4.2. One level set denoted as ψ (the green solid line) separates the space into two zones, could be taken as a crack path and its expansion along tangent direction. The other level set denoted as ϕ (the blue dotted line) defines the crack front surface which is perpendicular to the first one. The intersection of two level sets is the crack tip (the red point).

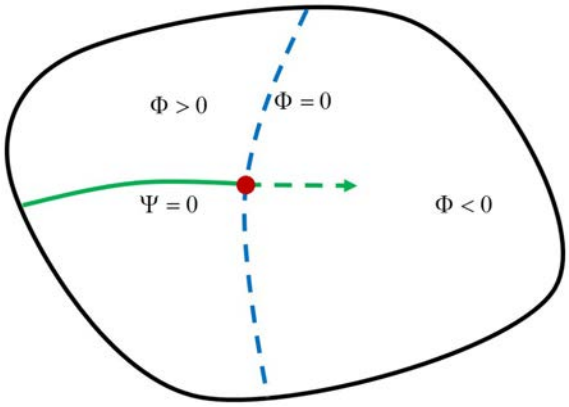

FIGURE 4.2: Crack path presented by two level sets

4.2.4 Evaluation of the stress intensity factors

J-integral were extracted by the volume integrals, as introduced in Section3.4.3, then converted to the stress intensity factor. In CAST3M, it can be realised by *GTHETA* function.

4.3 Simulation of experiment

The simulation was conducted by CAST3M software. The level set was realized by PSI-PHI function which describes the local frame of the crack. The volume integral was provided by *GTHETA* function. The procedure is illustrated in Fig.4.3. An example will be given to illustrate the simulation process.

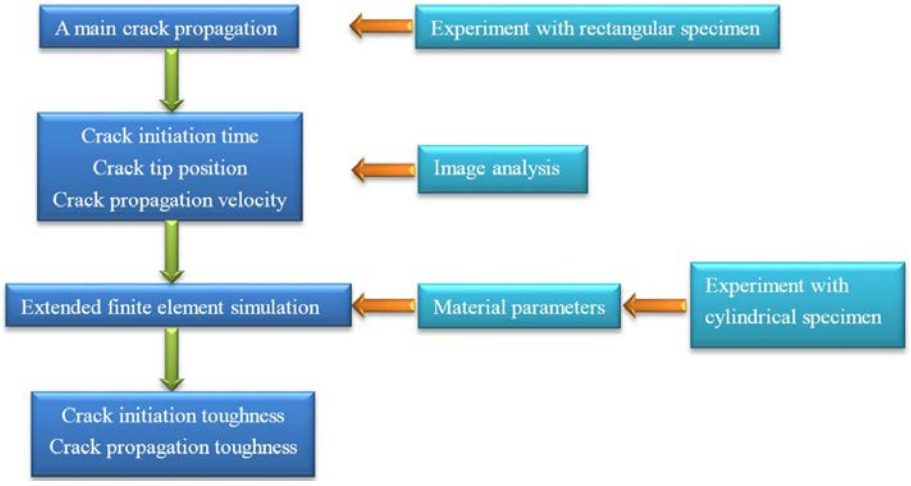

FIGURE 4.3: Methodology to access crack propagation

4.3.1 Model

A numerical simulation was established as a 2D model shown in Fig.4.4. The specimen with the input and output bars of SHPB setup were simulated. But only the specimen was meshed. The bars were simulated with impedance boundary conditions to reduce the computational time. At each node on the specimen-bar interface, the stress and velocity were assumed by Eq.4.5. This was working only at the beginning before the wave reflected at the ends of the bars. The validity of the impedance condition has been checked by Grégoire et al [Grégoire et al., 2007].

The impact velocity was obtained from experiments by Eq. 4.6, and simplified as shown in Fig.4.5.

$$\begin{cases} \sigma \cdot n = -z(v - v_{impact} \cdot n)n \;\; input\ bar \\ \sigma \cdot n = -z(v \cdot n)n \;\; output\ bar \\ z = \rho^{bar} c^{bar} \end{cases} \tag{4.5}$$

$$V_{impact} = C_0 \varepsilon_i(t) \tag{4.6}$$

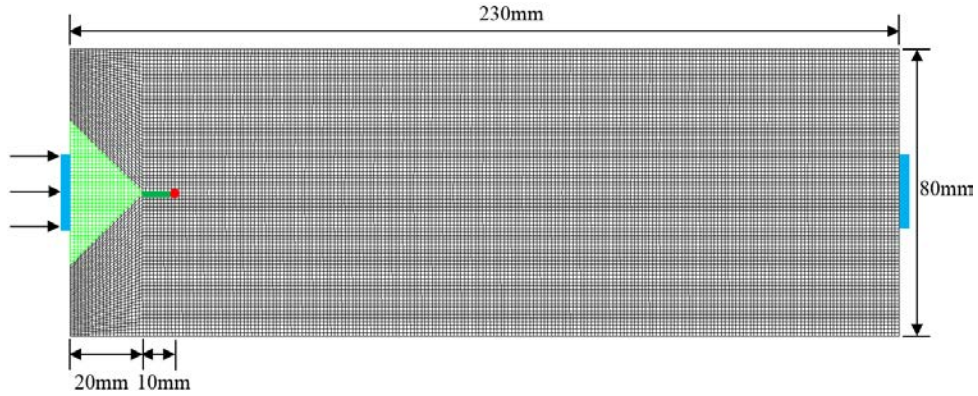

(a) Rectangular ice specimen with wedge and pre-crack

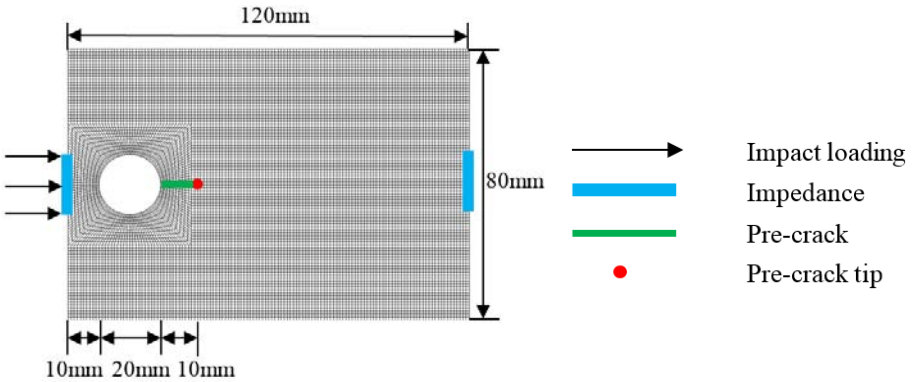

(b) Rectangular ice specimen with hole and pre-crack (c)

FIGURE 4.4: Two types of XFEM numerical simulation models

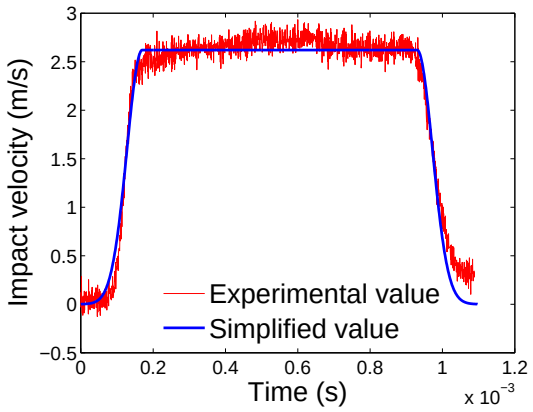

FIGURE 4.5: Impact velocity used in the simulation evaluated by experimental incident signal

4.3.2 Algorithm

The discrete equation is as below.

$$M\frac{u^{n+1}-2u^n+u^{n-1}}{\Delta t^2}+K\frac{u^{n+1}+2u^n+u^{n-1}}{4}=F^n \tag{4.7}$$

Where M and K are the mass and the stiffness matrices. u^n is the displacement at time step t^n. F^n is the vector of external forces at time step t^n. Then the displacement at time step t^{n+1} is calculated.

$$(\frac{M}{\Delta t^2}+\frac{K}{4})u^{n+1}=F^n+2(\frac{M}{\Delta t^2}-\frac{K}{4})u^n-(\frac{M}{\Delta t^2}+\frac{K}{4})u^{n-1} \tag{4.8}$$

Node j is one of the nodes on the interface between input bar and the specimen. And the external force on node j is as below :

$$\sigma_j=\rho C v_0-\rho C\Sigma v_j\varphi_j \tag{4.9}$$

where, φ_j is the shape function. Then, external forces can be expressed by all the nodes on the interface.

$$F_i=\int_i \sigma\varphi_j=\int_i \rho C(v_0-\sum v_j\varphi_j)\varphi_i=\rho C v_0\int_i \varphi_j-\sum v_j\rho C\int_i \varphi_j\varphi_i \tag{4.10}$$

Φ_i is defined as

$$\Phi_i=\rho C v_0\int_i \varphi_i \tag{4.11}$$

K_{imped} is defined as

$$K_{imped}=\rho C\int_i \varphi_j\varphi_i \tag{4.12}$$

v_j is expressed by

$$v_j=\frac{u^{n+1}-u^{n+1}}{2\Delta t} \tag{4.13}$$

Then the displacement at time step t^{n+1} is converted into

$$(\frac{M}{\Delta t^2}+\frac{K}{4}+\frac{K_{imped}}{2\Delta t})u^{n+1}=F^n+2(\frac{M}{\Delta t^2}-\frac{K}{4})u^n-(\frac{M}{\Delta t^2}+\frac{K}{4}-\frac{K_{imped}}{2\Delta t})u^{n-1} \quad (4.14)$$

4.3.3 Determination of numerical parameters

To perform the numerical simulation of the experiments, we need to know the mechanical behaviour of ice. As it behaves like a very brittle material we limit our investigation to the Young's modulus under impact. Mechanical properties used in simulations are listed in Tab.4.1. Some values are collected from literatures, and others are measured experimentally as discussed previously.

Mechanical properties	Nylon	Ice
Density (kg/m^3)	1100	900
Dynamic Young's modulus (GPa)	3.6[Karimzada and Maigre, 2000]	4.0
Poisson's ratio	0.41 [Karimzada and Maigre, 2000]	0.3[Petrovic, 2003]
Velocity of longitudinal waves (m/s)	1600	

TABLE 4.1: Mechanical properties of ice and Nylon used in the simulation

4.3.4 Evaluation of crack initiation toughness

The crack initiation toughness of ice under impact was estimated when the simulation fitted the experiment. From experiments, the impact velocity was measured from the gauges, and the crack initiation time was estimated from image analysis.

First, assuming the crack did not propagate during the loading process. A stress intensity factor history at the pre-crack tip was calculated as show in Fig.4.11.

After, the stress intensity factor curve needed to be connected with the experimental signal by making the impact velocity in the simulation coincide with the incident signal from the experiment. The beginning time of impact velocity in the input signal was determined noted as black line.

Since the incident signal was collected from the gauge glued in the middle of the input bar, whereas the impact velocity acted on the specimen directly in the simulation as shown in Fig.4.7.

The wave needed to propagate half length of the input bar from the gauge to the specimen. The impact velocity needed to be shifted. The synchronization between the signal, and numerical results was established with translating impact velocity and SIF history by time $\Delta t1=\frac{L_B}{2C_0}$, where C_0 is the longitudinal wave velocity in Nylon and L_B is the length of the input bar as shown in Fig.4.8.

After, the crack initiation time was estimated from image analysis. The crack initiation time

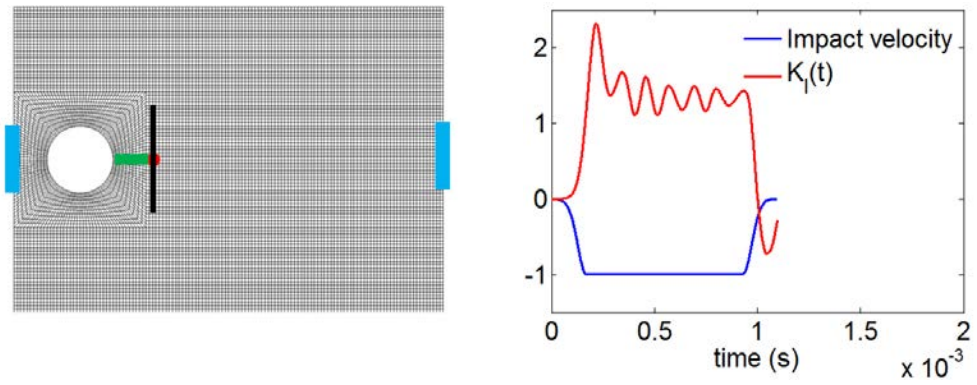

(a) Crack without propagation

(b) Stress intensity factor and corresponding impact velocity

FIGURE 4.6: Numerical stress intensity factor at pre-crack tip without propagation

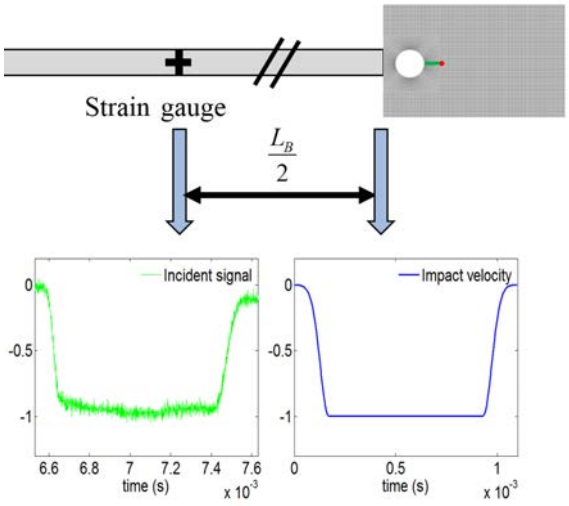

FIGURE 4.7: Position of incident signal and impact loading

was determined by the crack length and the crack propagation velocity in this interval. Therefore the translation time $\Delta t2$ was the duration from the beginning of the camera recording to a visible crack appearance. The black bold vertical line presents the crack initiation time as shown in Fig.4.9.

Finally , the synchronization among the signal, image, and numerical results were established. The crack initiation toughness was the intersection point of the stress intensity factor history and the crack initiation time.

The Young's modulus in the simulation was $4Gpa$ according to the experimental results. $3GPa$ and $5GPa$ was also checked. The stress intensity factor history at the pre-crack tip position is shown in Fig.4.10. The crack initiation toughness is $217.7kPa\cdot\sqrt{m}$, $233.2kPa\cdot\sqrt{m}$, $235.3kPa\cdot\sqrt{m}$

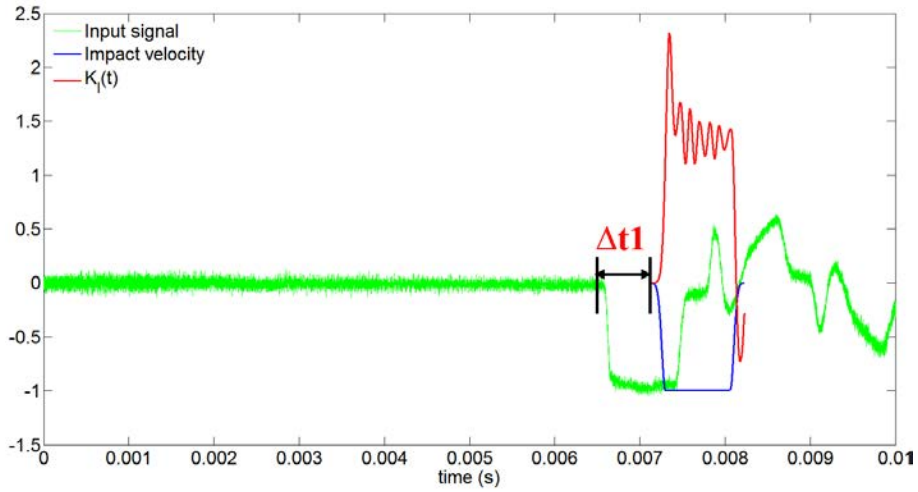

FIGURE 4.8: Translation between incident signal in experiment and impact velocity in simulation, $\Delta t1 = \dfrac{L_B}{2C_0}$

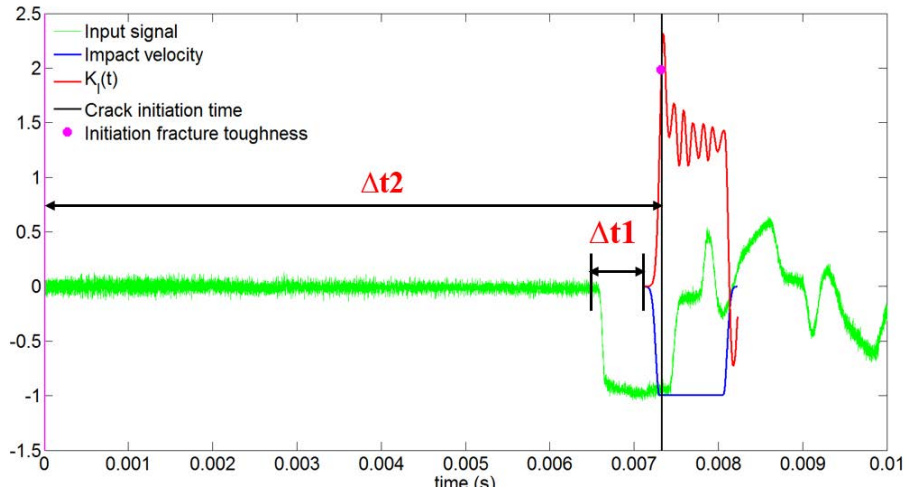

FIGURE 4.9: Crack initiation toughness estimated by the synchronizing experimental signals, images and numerical results, $\Delta t2$ crack initiation time

with the dynamic Young's modulus $3GPa$, $4GPa$, $5GPa$. The dispersion could be accepted even there was an experimental error in measuring the dynamic Young's modulus.

4.3.5 Evaluation of crack growth toughness

Once a crack initiated in ice under impact, to estimate the crack growth toughness the crack propagation velocity must be taken into account.

In simulations, once the stress intensity factor at the pre-crack tip was larger than crack initia-

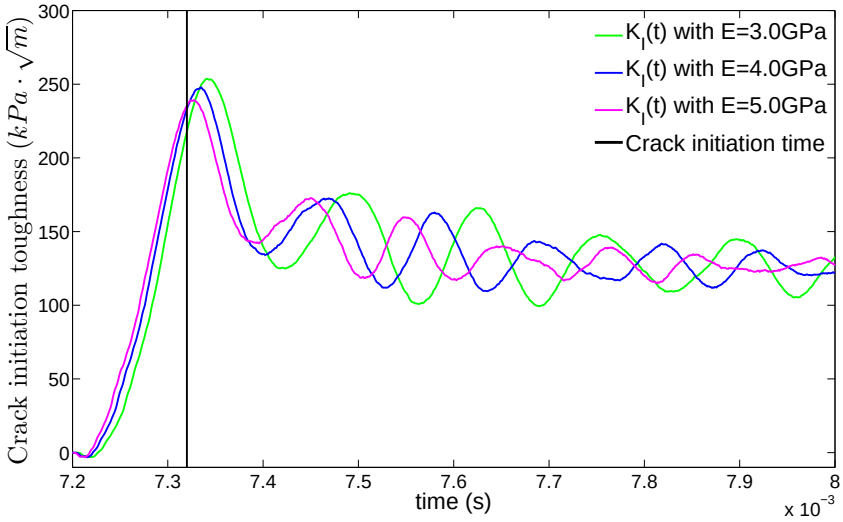

FIGURE 4.10: Crack initiation toughness estimated with different Young's modulus

tion toughness, the crack started to propagate.

The crack length of each section was measured from the image based on the experiment as shown in Fig.4.11a, and also obtained the velocity by previous image analysis. The time step used in the simulation was not the same with the interval time. So the crack propagation velocity used in the simulation is an equivalent value as shown in Fig.4.11b. The crack growth path was pre-defined and divided into sections as shown in Fig.4.11c.

Then we calculated the stress intensity factors at the end of each section in the interval considered as the crack growth toughness.

One typical stress intensity factor history is shown in Fig.4.12.

4.4 Numerical results

4.4.1 Crack initiation toughness

The crack initiation toughness is estimated to be $204 \pm 13 kPa \cdot \sqrt{m}$. The related experimental conditions are listed in Tab.4.2. The dynamic value is in the range of $50 \sim 400 kPa \cdot \sqrt{m}$ as reported under quasi-static loading [Liu and Miller, 1979][Bentley et al., 1989] [Dempsey, 1991] [Petrovic, 2003]. As noted before, the crack initiation time is estimated by the crack length and the crack propagation velocity in the onset interval. The onset crack length can be measured from images, but the onset crack propagation velocity can be identified only roughly. It could caused the crack initiation toughness scattered across the interval. It is why the toughness identified from the previous image and the next image is also plotted in FIG.4.13.

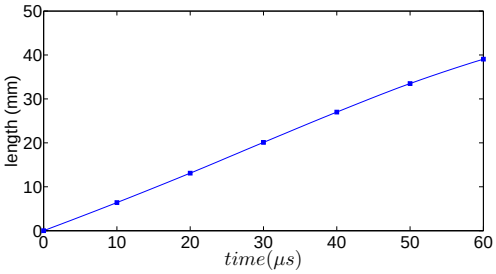

(a) Crack length from experiment

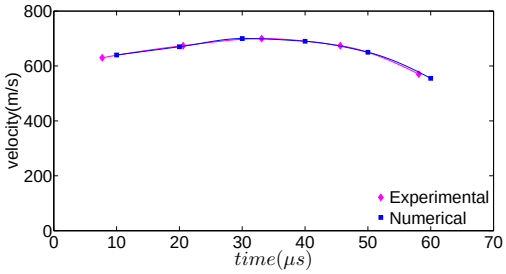

(b) Crack propagation velocity

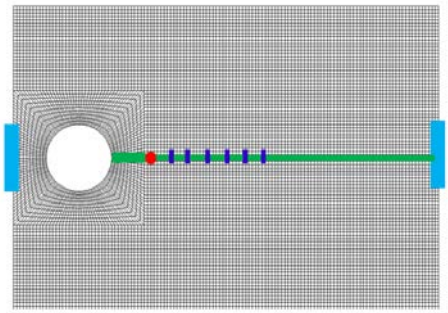

(c) Pre-defined Crack path

FIGURE 4.11: Crack path divided according to the experimental results

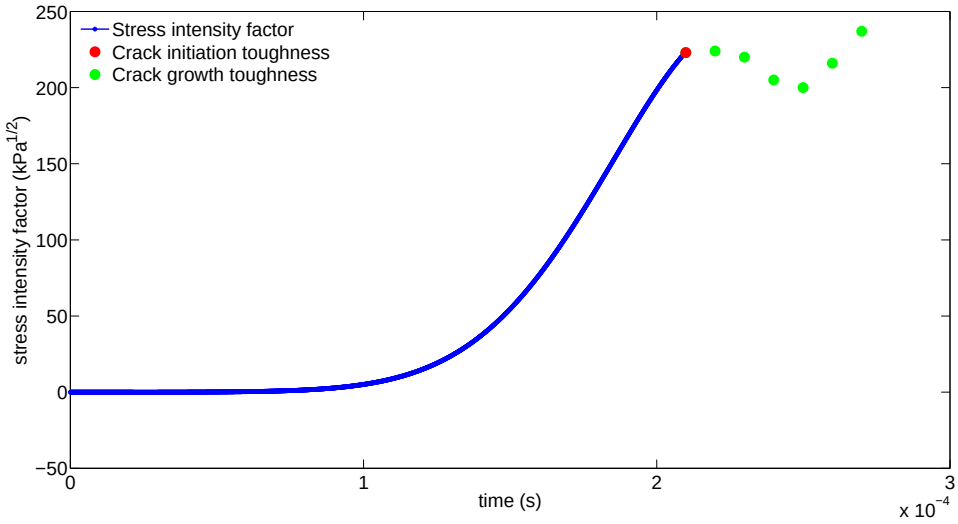

FIGURE 4.12: Stress intensity factor history from numerical simulation

Number	2014052701	2014052702	2014053005	2014053006	2014053004
Interval (μs)	27.0	27.0	12.5	12.5	12.5
Toughness $kPa \cdot \sqrt{m}$	219	190	198	210	201

TABLE 4.2: Crack initiation toughness of ice

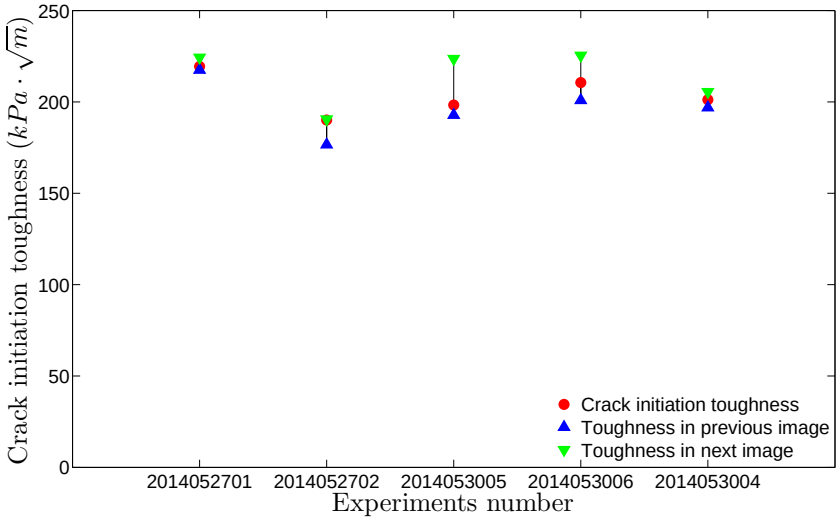

FIGURE 4.13: Dispersive range of crack initiation toughness

4.4.2 Fracture toughness history

The fracture toughness history over time from 3 groups of experiments is plotted in Fig.4.14. At time zero the crack initiates, the stress intensity factor is $204 \pm 13 kPa \cdot \sqrt{m}$. Next the crack growth toughness is $208 \pm 48 kPa \cdot \sqrt{m}$ which is more scattered than the crack initiation toughness.

The crack initiates when the loading still increases before it reaches plateau. Therefore, the loading rate is taken into account when we assess the fracture behaviour. The loading rate is represented by the increase rate of the initial dynamic stress intensity factor $\dot{K}_I$ also reported in the legend of Fig.4.14. When $\dot{K}_I$ is above $2 \times 10^6 kPa \cdot \sqrt{m}/s$, (red curves for C type specimens) then the crack growth toughness increases over time. When $\dot{K}_I$ ranges form $5 \times 10^5 kPa \cdot \sqrt{m}/s$ to $1.5 \times 10^6 kPa \cdot \sqrt{m}/s$ then the crack growth toughness is close to the initiation toughness. When $\dot{K}_I$ is lower than $5 \times 10^5 kPa \cdot \sqrt{m}/s$, the crack growth toughness decreases.

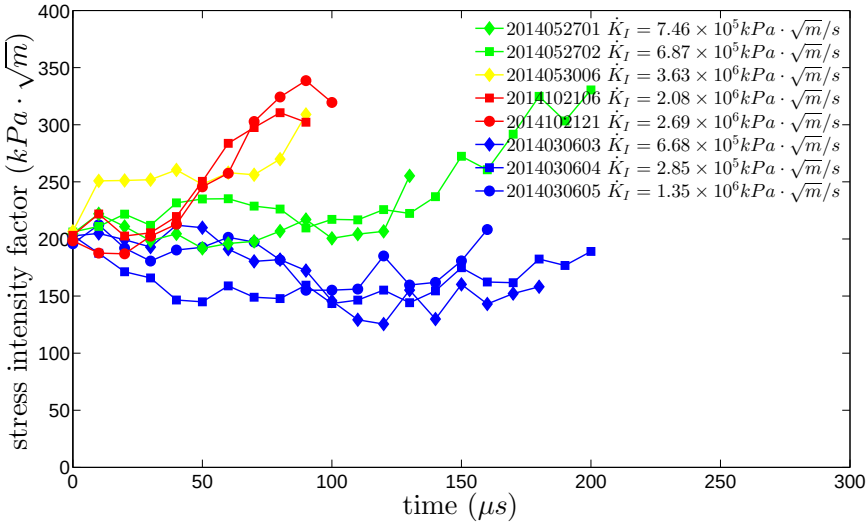

FIGURE 4.14: Fracture toughness history of ice in simulation depending on increase rate of initial dynamic stress intensity factor

4.4.3 Crack growth toughness and propagation velocity

When the crack grows, the crack propagation velocity should be taken into account. The crack growth toughness versus the crack propagation velocity is plotted in Fig.4.15. From this data, it is possible to obtain the fitted curves, as reported by Freund et al[Freund, 1998], showing that the crack growth fracture toughness is linearly associated with the crack propagation velocity. Despite experiment 2014053006, the fitted curves belonging to each group are paralleled to a first approximation.

4.5 Conclusion and recommendations

The extended finite element method was employed to assess the dynamic crack propagation criteria in this chapter. When the simulation fitted the experiment, the crack initiation toughness and the crack growth toughness were evaluated from the simulation results. The relationship between the crack growth toughness and crack propagation velocity was established.

I- The crack initiation time was estimated by the synchronization between SHPB signals and images. Then the time corresponded with the simulation. The corresponding initiation toughness in the simulation is determined to be $204 \pm 13 kPa \cdot \sqrt{m}$.

II- With the crack propagation velocity in the previous chapter, the crack path was pre-defined and divided into sections. Then the crack growth toughness in each section is determined to

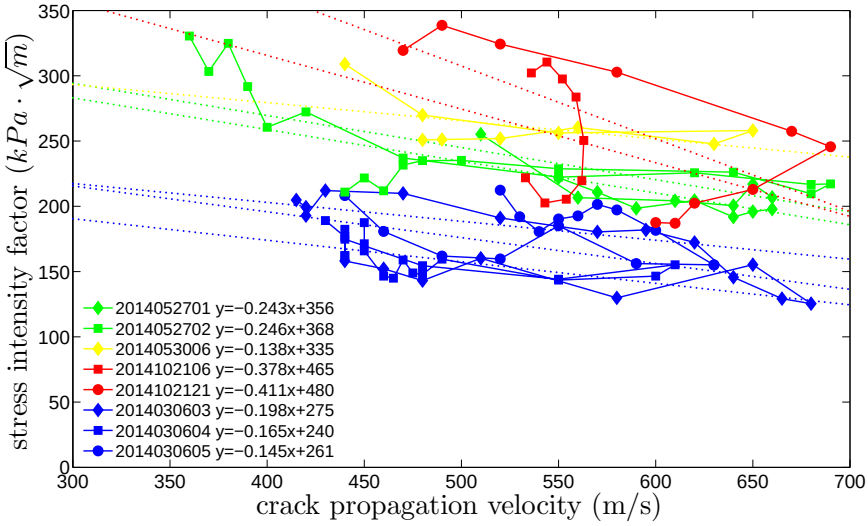

FIGURE 4.15: Crack growth toughness history versus crack propagation velocity

be $208 \pm 48 kPa \cdot \sqrt{m}$. And the crack growth fracture toughness is linearly associated with the crack propagation velocity.

III- The crack growth toughness is sensitive to the loading rate represented by the rate of increase of the initial dynamic stress intensity factor and seems independent to the temperature in the range $-15 \sim -1°C$.

In this chapter, we only introduced the crack criteria obtained by pre-defining the crack history in the simulation. We also took much time and effort to define a universal relation between the crack propagation velocity and the fracture toughness and tried to use the crack criteria to predict the crack propagation. But we did not get meaningful results consistent well with the experimental results. Of all the possible reasons one might think it is due to the defects in the specimen, it can not be taken as a homogeneous material. The growth fracture toughness is scattered along the fitted curve as shown in FIG.4.15. We can eliminate the defect effect by curve fitting to assess the crack propagation, but we can not forecast the crack propagation ignoring the defects with the criteria defined with the fitting curve.

General conclusions and prospects

Conclusions

Experimental and numerical works have been done in this study with the objective of investigating the crack propagation in ice under impact loading. A series of impact experiments with different ice specimens has been conducted using Split Pressure Hopkinson bars. The image analysis method has been employed to describe the crack propagation history. The extended finite element method has been used to simulate the experimental process. We managed to establish the methodology of investigating crack propagation in ice and find preliminary results about the dynamic fracture behaviour of ice.

I- The methodology of investigating dynamic crack propagation in ice is established by SHPB experiments, image analysis and XFEM simulation.

II- The dynamic stress-strain behaviour has been obtained from experiments with cylindrical specimens. The measured dynamic Young's modulus is about $4GPa$ which is used in the numerical simulation. The peak stress is in the range of $1.5MPa \sim 5.5MPa$.

III- The rectangular specimen is separated into two main parts after the impact. The crack propagates in Mode I. With the help of image analysis, the crack propagation history and the crack propagation velocity are obtained. The crack propagation velocity firstly increases and then keeps at a constant value. Afterwards, it decreases. It reaches $534 \pm 83 m/s$, which is about 25% of the Rayleigh wave velocity in ice $(2000 m/s)$.

IV- The crack initiation time is estimated by the synchronization between SHPB signals and images. The corresponding initiation toughness in the simulation is $204 \pm 13 kPa \cdot \sqrt{m}$. The crack path is pre-defined and divided into sections according to the crack propagation velocity. Then the crack growth toughness is determined to be $208 \pm 48 kPa \cdot \sqrt{m}$ which is linearly associated with the crack propagation velocity.

V- The crack growth toughness is sensitive to the loading rate represented by the rate of increase of the initial dynamic stress intensity factor. The dynamic behaviour of ice under impact loading seems temperature independent in the range $-15 \sim -1°C$.

Prospects

The results obtained by experiments and simulations are only a first approximation of the dynamic fracture behaviour of the ice under impact loading.

I- The experimental result in this work was dispersive, the may reason was that the quality of the specimen was not uniform. The laboratory-grown ice had avoidable defects which had influences on the results. Since the methodology was established, the dynamic crack propagation in particular ice can be investigated in the same way.

II- The future work will focus on evaluating the fracture toughness with the digital image correlation method. The results can be taken as the verification and validation of the simulation values. To attain it, two aspects need to be improved, the quality of images and the precision of the DIC algorithm.

III- The fracture toughness seems independent to the temperature in the investigated range of temperature. In order to investigate the sensitivity of the dynamic fracture behaviour of ice, the temperature needs to a larger range. Meanwhile, the experiments need to be conducted under a larger range of impact loadings.

IV- Regarding the numerical aspect, more effort should be devoted also to define a universal relation between the crack propagation velocity and the fracture toughness and also to predict the crack propagation. This is to be continued.

Appendix A

A.1 Introduction

The experimental parameters and results are summarised here briefly.

The mechanical properties of ice are sensitive to the structure of ice, the configuration of specimen, the experimental condition. The strength and Young's modulus of ice were reported in a large range in different literature. Precise values were needed for the following simulation in evaluating the fracture toughness. In order to obtain the strength and dynamic Young's modulus in the same condition with the crack propagation experiment, three groups of experiments were designed firstly :

1) A group of experiments with the cylindrical specimen of a diameter of 50mm was conducted with different impact velocity to obtain the range of strength and Young's modulus.

2) A group of experiments with the cylindrical specimen of a diameter of 50mm with confinement was conducted to investigate the confinement effect. Since the ice specimen in the crack propagation experiment was in an intermediate state between with and without confinement.

3) A group of experiments with the cylindrical specimen of a diameter of 20mm was conducted with a critical impact velocity to obtain the critical strength and Young's modulus of specimen fracture.

Then, with the purpose of investigating the crack propagation in ice under impact loading, two groups of experiments were designed :

1) A group of experiments with the rectangular specimen with a wedge and a pre-crack was conducted with different impact velocity to obtain a main crack propagation.

2) A group of experiments with the rectangular specimen with a hold and a pre-crack was conducted with different impact velocity to obtain a main crack propagation.

For the specimen with wedge, the waves transferred and reflected complicatedly on interface of the wedge and the specimen. It was hard to do signal analysis. Such a problem could be avoided with the rectangular specimens with hole. In this type specimen, the input bar impact on the specimen directly. But the stress distribution was more complex near the hole. So both types of specimens were used.

A.2 Cylindrical ice specimens

A.2.1 Cylindrical ice specimens of diameter of 50mm

Number	Diameter (mm)	Length (mm)	Pressure (KPa)	Striker velocity (m/s)
2013020801	49,1	31,9	122	15,87
2013020802	49,0	43,0	122	14,05
2013020803	48,9	44,0	122	11,82
2013020804	49,0	104,5	122	14,06
2013020805	49,2	116,9	122	16,23
2013020806	48,0	34,0	82	5,93
2013020807	48,0	47,0	81	5,94
2013020808	48,0	47,0	81	16,67
2013020809	49,0	105,0	81	21
2013030505	48,5	104,1	80	22,11
2013030506	48,1	108,5	83	23,81

TABLE A.1: Experimental parameters of cylindrical ice specimen 50mm in diameter group 1

Number	Impact velocity (m/s)	Peak stress (MPa)	Strain at peak stress	Strain rate at peak stress (s^{-1})	Strain rate maximum (s^{-1})
2013020801	5,25	7.24	0.0027	52.267	52.65
2013020802					
2013020803	4.54	4.48	0.0061	131.35	188.87
2013020804	5.49	5.59	0.0032	64.38	94.14
2013020805	6.41				
2013020806	2.22	2.48	0.0032	66.64	95.4
2013020807	3.28	3.64	0.0052	92.33	127.45
2013020808	3.89	4.62	0.0044	105.77	114.51
2013020809	5.35	7.21	0.0024	51.93	53.44
2013030505	5.98	7.01	0.0035	72.66	73.07
2013030506	5.68	7.95	0.0025	57.21	59.86

TABLE A.2: Experimental results of cylindrical ice specimen 50mm in diameter group 1

Number	Weight (g)	Diameter (mm)	Length (mm)	Density (g/mm^3)	Pressure (KPa)	Striker velocity (m/s)
2013070401	159.77	49.00	93.55	0.906	75	3.27
2013070402	160.27	49.02	95.74	0.887	76	3.60
2013070403	165.62	50.04	95.11	0.886	82	4.81
2013070404	173.59	49.59	97.46	0.923	89	5.48
2013070405	171.30	49.31	97.36	0.922	99	6.61
2013070406	126.81	49.39	73.76	0.898	85	6.69
2013070407	148.10	48.21	88.41	0.918	78	4.81
2013070408	167.69	48.88	96.50	0.927	80	5.28
2013070409	148.36	48.36	93.15	0.868	92	4.17
2013070410	172.73	49.59	96.55	0.927	99	5.24
2013070411	162.36	49.03	95.05	0.905	100	7.32
2013070413	171.31	49.62	97.21	0.912	94	6.44
2013070414	162.96	49.47	93.57	0.907	93	5.00
2013070415	166.50	49.16	94.56	0.928	94	6.05

TABLE A.3: Experimental parameters of cylindrical ice specimen 50*mm* in diameter group 2

Number	Impact velocity (m/s)	Peak stress (MPa)	Strain at peak stress	Strain rate at peak stress (s^{-1})	Strain rate maximum (s^{-1})
2013070401	1.67	1.62	0.0068	12.50	18.73
2013070402	1.91	2.29	0.0063	8.07	16.25
2013070403	2.68	2.73	0.0015	16.76	29.21
2013070404	3.12	3.42	0.0098	15.80	31.52
2013070405	3.92	4.05	0.0168	20.77	39.48
2013070406	3.69	2.93	0.0011	12.65	29.00
2013070407	3.06	2.62	0.0017	20.82	38.47
2013070408	2.30	2.05	0.0113	18.60	26.69
2013070409	3.05	3.47	0.0091	13.09	23.38
2013070410	4.33	5.40	0.0095	12.45	28.57
2013070411	3.84	4.69	0.0010	8.46	36.83
2013070413	3.81	4.81	0.0098	9.61	28.00
2013070414	2.82	2.74	0.0122	20.02	31.33
2013070415	3.54	4.13	0.0113	14.12	25.19

TABLE A.4: Experimental results of cylindrical ice specimen 50*mm* in diameter group 2

A.2.2 Cylindrical ice specimens of diameter of 50mm with confinement

Number	Weight (g)	Diameter (mm)	Length (mm)	Density (g/mm^3)	Pressure (KPa)	Striker velocity (m/s)
2013071901	161.49	49.51	92.91	0.903	81	4.72
2013071902	154.89	48.97	89.98	0.914	99	6.14
2013071903	153.63	48.95	89.92	0.908	78	3.94
2013071904	150.52	49.22	89.25	0.887	108	7.28
2013071905	161.79	49.46	92.52	0.911	91	5.47
2013071906	162.88	49.56	93.48	0.904	72	1.66
2013071907	151.67	49.40	87.10	0.909	75	2.42
2013071908	165.97	49.42	94.18	0.919	84	4.90
2013071909	157.22	49.33	89.93	0.915	75	3.07
2013071910	155.93	49.13	90.07	0.914	120	8.79
2013071911	165.84	48.92	96.69	0.913	121	8.36
2013071912	161.88	49.28	93.58	0.907	89	6.25
2013071913	159.70	49.34	91.61	0.912	80	4.90
2013071914	160.76	49.32	92.15	0.914	83	3.40
2013071915	160.24	49.39	91.34	0.916	85	3.97

TABLE A.5: Experimental parameters of cylindrical ice specimen 50*mm* in diameter with confinement

Number	Impact velocity (m/s)	Peak stress (MPa)	Strain at peak stress	Strain rate at peak stress (s^{-1})	Strain rate maximum (s^{-1})
2013071901	2.59	1.40	0.0133	35.27	40.70
2013071902	3.51	3.58	0.0192	20.18	50.93
2013071903	2.10	1.76	0.0047	18.50	23.51
2013071904	4.25	4.70	0.0216	23.07	65.93
2013071905	3.12	1.47	0.0299	40.28	50.06
2013071906					
2013071907	1.08	1.28	0.0063	19.10	21.09
2013071908	2.75	2.55	0.0134	20.50	30.21
2013071909	1.56	1.67	0.0039	9.26	15.30
2013071910	5.19	4.82	0.0319	36.64	81.56
2013071911	4.89	4.13	0.0308	39.99	74.47
2013071912	2.73	2.67	0.0051	18.25	28.16
2013071913	1.73	2.11	0.0174	24.68	33.03
2013071914	2.13	2.01	0.0079	16.99	26.33
2013071915	2.68	2.66	0.0170	17.63	39.70

TABLE A.6: Experimental results of cylindrical ice specimen 50mm in diameter with confinement

A.2.3 Cylindrical ice specimens of diameter of 20mm

Number	Temperature °C	Diameter (mm)	Length (mm)	Pressure (kPa)	Striker velocity (m/s)
2014053012	-1	20	40	100	6.90
2014053013	-1	20	50	95	2.94
2014053014	-1	20	51	95	3.45
2014053015	-1	20	45	95	3.11

TABLE A.7: Experimental parameter of cylindrical ice specimen 20*mm* in diameter

Number	Impact velocity (m/s)	Peak stress (MPa)	Strain at peak stress	Strain rate at peak stress (s^{-1})	Strain rate maximum (s^{-1})
2014053012	1.43	1.34	0.0015	28.40	62.75
2014053013	0.56	0.64	0.0064	16.85	19.90
2014053014	0.52	0.94	0.0054	6.90	15.79
2014053015	0.60	0.48	0.0060	17.27	18.53

TABLE A.8: Experimental results of cylindrical ice specimen 20*mm* in diameter

A.3 Rectangular ice specimens with a wedge and pre-crack

Number	Temperature (°C)	Pressure (kPa)	Striker velocity (m/s)
2014022801	-7	70	9.96
2014022802	-7	60	7.42
2014022803	-7	60	7.62
2014022804	-1	60	6.45
2014022805	-1	60	6.50

TABLE A.9: Experimental parameters of rectangular ice specimen with a wedge and pre-crack Group 1

Number	Resolution	Exposure(μs)	Interval (μs)	Frame rate
2014022801	640*400	29.53	38.46	26003
2014022802	512*320	14.41	25.63	39013
2014022803	512*320	14.41	25.63	39013
2014022804	512*256	14.74	20.40	49026
2014022805	512*256	14.74	20.40	49026

TABLE A.10: Image parameters of rectangular ice specimen with a wedge and pre-crack Group 1

Number	Temperature ($^\circ$C)	Pressure (kPa)	Striker velocity (m/s)	Impact velocity (m/s)
2014030501	-7	60	6.50	4.19
2014030502	-7	60	7.41	3.85
2014030503	-7	60	7.34	3.92
2014030504	-7	60	8.36	4.91
2014030505	-7	50	5.71	1.88

TABLE A.11: Experimental parameters of rectangular ice specimen with a wedge and pre-crack Group 2

Number	Resolution	Exposure(μs)	Interval (μs)	Frame rate
2014030501	512*344	14.56	27.01	37016
2014030502	512*344	14.56	27.01	37016
2014030503	512*344	14.56	27.01	37016
2014030504	512*344	14.56	27.01	37016
2014030505	512*344	14.56	27.01	37016

TABLE A.12: Image parameters of rectangular ice specimen with a wedge and pre-crack Group 2

Number	Temperature ($^\circ$C)	Pressure (kPa)	Striker velocity (m/s)	Impact velocity (m/s)
2014030601	-1	60	6.02	1.87
2014030602	-1	60	7.34	2.82
2014030603	-1	60	8.06	2.27
2014030604	-1	60	6.90	1.89
2014030605	-1	60	5.98	1.51
2014030606	-1	60	8.77	4.03

TABLE A.13: Experimental parameters of rectangular ice specimen with a wedge and pre-crack Group 3

Number	Resolution	Exposure(μs)	Interval (μs)	Frame rate
2014030601	512*344	14.56	27.01	37016
2014030602	512*344	14.56	27.01	37016
2014030603	512*344	14.56	27.01	37016
2014030604	512*344	14.56	27.01	37016
2014030605	512*344	14.56	27.01	37016
2014030606	512*344	14.56	27.01	37016

TABLE A.14: Image parameters of rectangular ice specimen with a wedge and pre-crack Group 3

A.4 Rectangular ice specimens with a hole and pre-crack

A.4.1 Rectangular ice specimens with a hole and pre-crack of length of 230mm

Number	Temperature ($^\circ$C)	Pressure (kPa)	Striker velocity (m/s)	Impact velocity (m/s)	Dimensions (mm^3)
2014052701	-8	60	5.68	3.66	225*90*35
2014052702	-1	60	5.06	3.49	223*90*30
2014052703	-1	60	7.08	5.38	178*90*28
2014053003	-1	100	4.63	1.40	123*90*29
2014053004	-1	120	8.53	2.68	123*90*29
2014053005	-1	120	8.99	2.86	118*90*27
2014053006	-1	120	8.65	2.87	129*90*29
2014053007	-1	110	6.62	2.04	168*90*24
2014053008	-1	110	6.68	2.10	160*90*40
2014053009	-1	120	8.90	2.79	230*90*40
2014053010	-1	130	10.57	3.29	230*90*40
2014053011	-1	140	10.80	2.34	230*90*40

TABLE A.15: Experimental parameters of rectangular ice specimen with a hole and pre-crack Group 1

Number	Resolution	Exposure(μs)	Interval (μs)	Frame rate	State
2014052701	512*344	25.68	27.01	37016	break
2014052702	512*344	25.68	27.01	37016	break
2014052703	512*192	18.66	20.00	50000	not
2014053003	384*192	14.56	12.50	80000	break
2014053004	384*192	14.56	12.50	80000	break
2014053005	384*192	14.56	12.50	80000	break
2014053006	384*192	14.56	12.50	80000	break
2014053007	384*192	14.56	12.50	80000	break
2014053008	384*192	14.56	12.50	80000	break
2014053009	384*192	14.56	12.50	80000	not
2014053010	384*192	14.56	12.50	80000	break
2014053011	384*192	14.56	12.50	80000	break

TABLE A.16: Image parameters of rectangular ice specimen with a hole and pre-crack Group 1

A.4.2 Rectangular ice specimens with a hole and pre-crack of length of 120mm

Number	Temperature °C	Pressure (kPa)	Striker velocity (m/s)	Impact velocity (m/s)
2014102001	-5	100	5.38	
2014102002	-5	90	5.32	2.74
2014102003	-5	70	2.81	1.24
2014102004	-10	80	4.27	1.95
2014102005	-10	75	3.42	1.58
2014102006	-10	80	4.20	1.99
2014102007	-10	85	4.42	2.07
2014102008	-10	95		2.50

TABLE A.17: Experimental parameters of rectangular ice specimen with a hole and pre-crack Group 2

Number	Resolution	Exposure(μs)	Interval (μs)	Frame rate	State
2014102001	512*320	4.53	25.63	39013	break
2014102002	512*320	4.53	25.63	39013	break
2014102003	464*280	8.94	25.10	45003	not
2014102004	464*280	8.94	25.10	45003	break
2014102005	368*280	8.57	18.18	55016	not
2014102006	368*280	8.57	18.18	55016	not
2014102007	368*280	8.57	18.18	55016	not
2014102008	368*280	8.57	18.18	55016	break

TABLE A.18: Image parameters of rectangular ice specimen with a hole and pre-crack Group 2

Number	Temperature °C	Pressure (kPa)	Striker velocity (m/s)	Impact velocity (m/s)
2014102101	-5	85	4.81	2.40
2014102102	-15	85	4.81	2.11
2014102103	-15	90	4.81	2.11
2014102104	-15	95	5.10	2.13
2014102105	-15	95	5.38	2.21
2014102106	-15	100	5.49	2.60
2014102107	-15	100	5.88	2.06
2014102108	-15	100	6.10	2.01
2014102109	-15	100	5.49	1.98
2014102110	-10	110	5.49	2.01
2014102111	-15	100	6.25	1.97
2014102112	-15	100	5.68	2.00
2014102113	-15	95	7.04	1.95
2014102114	-15	100	6.17	1.95
2014102115	-15	100	5.95	1.96
2014102116	-15	100	5.95	2.03
2014102117	-15	100	6.10	2.01
2014102118	-15	100	6.02	2.06
2014102119	-15	100	5.88	2.09
2014102120	-15	100	6.17	2.06

TABLE A.19: Experimental parameters of rectangular ice specimen with a hole and pre-crack Group 3

Number	Temperature °C	Pressure (kPa)	Striker velocity (m/s)	Impact velocity (m/s)
2014102121	-15	100	7.46	3.77
2014102122	-15	100	6.02	1.98
2014102123	-15	100	6.25	2.01
2014102124	-15	100	6.17	2.03
2014102125	-15	100	6.17	2.06
2014102126	-15	110	7.35	1.98
2014102127	-15	100	6.17	2.01
2014102128	-15	100	6.41	2.00
2014102129	-15	105	8.06	1.95
2014102130	-15	100	6.10	2.00
2014102131	-15	105	6.25	2.10
2014102132	-15	105	7.25	1.95
2014102133	-15	105	6.67	1.98
2014102134	-15	105	6.67	

TABLE A.20: Experimental parameters of rectangular ice specimen with a hole and pre-crack Group 4

Number	Resolution	Exposure(μs)	Interval (μs)	Frame rate	State
2014102101	512*320	4.53	25.63	30913	break
2014102102	432*320	8.94	25.10	39835	not
2014102103	432*320	8.94	25.10	39835	not
2014102104	432*320	8.94	25.10	39835	break
2014102105	656*320	8.50	39.31	25439	not
2014102106	656*320	8.50	39.31	25439	break
2014102107	656*320	8.50	39.31	25439	break
2014102108	512*256	8.56	20.40	49026	break
2014102109	512*256	8.56	20.40	49026	not
2014102110	512*256	8.56	20.40	49026	break
2014102111	512*256	8.56	20.40	49026	break
2014102112	512*256	8.56	20.40	49026	break
2014102113	512*256	8.56	20.40	49026	not
2014102114	512*256	8.56	20.40	49026	break
2014102115	512*256	8.56	20.40	49026	break
2014102116	512*256	8.56	20.40	49026	break
2014102117	512*256	8.56	20.40	49026	break
2014102118	512*256	8.56	20.40	49026	break
2014102119	512*256	8.56	20.40	49026	break
2014102120	512*256	8.56	20.40	49026	not

TABLE A.21: Image parameters of rectangular ice specimen with a hole and pre-crack Group 3

Number	Resolution	Exposure(μs)	Interval (μs)	Frame rate	State
2014102121	512*256	8.56	20.40	49026	break
2014102122	512*256	8.56	20.40	49026	break
2014102123	512*256	8.56	20.40	49026	break
2014102124	512*256	8.56	20.40	49026	break
2014102125	512*256	8.56	20.40	49026	not
2014102126	512*256	8.56	20.40	49026	break
2014102127	512*256	8.56	20.40	49026	break
2014102128	512*256	8.56	20.40	49026	not
2014102129	512*256	8.56	20.40	49026	break
2014102130	512*256	8.56	20.40	49026	not
2014102131	512*256	8.56	20.40	49026	break
2014102132	512*256	8.56	20.40	49026	break
2014102133	512*256	8.56	20.40	49026	break
2014102134	512*256	8.56	20.40	49026	break

TABLE A.22: Image parameters of rectangular ice specimen with a hole and pre-crack Group 4

Biblography

[BABUŠKA and MELENK, 1997] BABUŠKA, I. and MELENK, J. (1997). The partition of unity method. *International Journal for Numerical Methods in Engineering*, 40(4) :727–758.

[Barenblatt, 1962] Barenblatt, G. I. (1962). The mathematical theory of equilibrium cracks in brittle fracture. *Advances in applied mechanics*, 7(1) :55–129.

[Belytschko et al., 2003] Belytschko, T., Chen, H., Xu, J., and Zi, G. (2003). Dynamic crack propagation based on loss of hyperbolicity and a new discontinuous enrichment. *International Journal for Numerical Methods in Engineering*, 58(12) :1873–1905.

[Belytschko et al., 2009] Belytschko, T., Gracie, R., and Ventura, G. (2009). A review of extended/generalized finite element methods for material modeling. *Modelling and Simulation in Materials Science and Engineering*, 17(4) :043001.

[Belytschko et al., 1996] Belytschko, T., Krongauz, Y., Organ, D., Fleming, M., and Krysl, P. (1996). Meshless methods : an overview and recent developments. *Computer methods in applied mechanics and engineering*, 139(1) :3–47.

[Belytschko et al., 1995a] Belytschko, T., Lu, Y., and Gu, L. (1995a). Crack propagation by element-free galerkin methods. *Engineering Fracture Mechanics*, 51(2) :295–315.

[Belytschko et al., 1995b] Belytschko, T., Lu, Y., Gu, L., and Tabbara, M. (1995b). Element-free galerkin methods for static and dynamic fracture. *International Journal of Solids and Structures*, 32(17) :2547–2570.

[Belytschko et al., 2000] Belytschko, T., Organ, D., and Gerlach, C. (2000). Element-free galerkin methods for dynamic fracture in concrete. *Computer Methods in Applied Mechanics and Engineering*, 187(3) :385–399.

[Belytschko and Tabbara, 1996] Belytschko, T. and Tabbara, M. (1996). Dynamic fracture using element-free galerkin methods. *International Journal for Numerical Methods in Engineering*, 39(6) :923–938.

[Bentley et al., 1989] Bentley, D., Dempsey, J., Sodhi, D., and Wei, Y. (1989). Fracture toughness of columnar freshwater ice from large scale dcb tests. *Cold regions science and technology*, 17(1) :7–20.

[Bluhm, 1969] Bluhm, J. (1969). Fracture arrest, v, l–63. *Fracture. Academic Press, New York*.

[Broberg, 1960] Broberg, K. B. (1960). The propagation of a brittle crack. *Arkiv Fysik*, 18(2) :159–192.

[Bui and Zhang, 2013] Bui, T. Q. and Zhang, C. (2013). Analysis of generalized dynamic intensity factors of cracked magnetoelectroelastic solids by x-fem. *Finite Elements in Analysis and Design*, 69 :19–36.

[Chamis et al., 1994] Chamis, C., Murthy, P., Singhal, S., and Reddy, E. (1994). Ice-impact analysis of blades. In *AGARD CONFERENCE PROCEEDINGS AGARD CP*, pages 23–23. DTIC Document.

[Cherepanov, 1967] Cherepanov, G. (1967). The propagation of cracks in a continuous medium. *Journal of Applied Mathematics and Mechanics*, 31(3) :503–512.

[Chu et al., 1985] Chu, T., Ranson, W., and Sutton, M. (1985). Applications of digital-image-correlation techniques to experimental mechanics. *Experimental mechanics*, 25(3) :232–244.

[Combescure et al., 2011] Combescure, A., Chuzel-Marmot, Y., and Fabis, J. (2011). Experimental study of high-velocity impact and fracture of ice. *International Journal of Solids and Structures*, 48(20) :2779–2790.

[Davies, 1948] Davies, R. (1948). A critical study of the hopkinson pressure bar. *Philosophical Transactions of the Royal Society of London A : Mathematical, Physical and Engineering Sciences*, 240(821) :375–457.

[Dempsey, 1991] Dempsey, J. P. (1991). The fracture toughness of ice. In *Ice-Structure Interaction*, pages 109–145. Springer.

[Dolbow and Belytschko, 1999] Dolbow, J. and Belytschko, T. (1999). A finite element method for crack growth without remeshing. *Int. J. Numer. Meth. Eng*, 46(1) :131–150.

[Duarte et al., 2001] Duarte, C., Hamzeh, O., Liszka, T., and Tworzydlo, W. (2001). A generalized finite element method for the simulation of three-dimensional dynamic crack propagation. *Computer Methods in Applied Mechanics and Engineering*, 190(15) :2227–2262.

[Dugdale, 1960] Dugdale, D. (1960). Yielding of steel sheets containing slits. *Journal of the Mechanics and Physics of Solids*, 8(2) :100–104.

[Dutta et al., 2004] Dutta, P. K., Cole, D. M., Schulson, E. M., and Sodhi, D. S. (2004). A fracture study of ice under high strain rate loading. *International Journal of Offshore and Polar Engineering*, 14 :182–188.

[Fasanella et al., 2006] Fasanella, E. L., Boitnott, R. L., and Kellas, S. (2006). Test and analysis correlation of high speed impacts of ice cylinders.

[Fischer et al., 1995] Fischer, M. P., Alley, R. B., and Engelder, T. (1995). Fracture toughness of ice and firn determined from the modified ring test. *Journal of glaciology*, 41(138) :383–394.

[Fleming et al., 1997] Fleming, M., Chu, Y., Moran, B., Belytschko, T., Lu, Y., and Gu, L. (1997). Enriched element-free galerkin methods for crack tip fields. *International journal for numerical methods in engineering*, 40(8) :1483–1504.

[Fletcher, 2009] Fletcher, N. H. (2009). The chemical physics of ice. *The Chemical Physics of Ice, by NH Fletcher, Cambridge, UK : Cambridge University Press, 2009*, 1.

[Freund, 1998] Freund, L. B. (1998). *Dynamic fracture mechanics*. Cambridge university press.

[Gagnon, 2003] Gagnon, R. (2003). High-speed video analysis of fracture propagation in a thick-edge-loaded freshwater ice sheet. *Canadian journal of physics*, 81(1-2) :261–269.

[Grégoire et al., 2007] Grégoire, D., Maigre, H., Rethore, J., and Combescure, A. (2007). Dynamic crack propagation under mixed-mode loading–comparison between experiments and x-fem simulations. *International Journal of Solids and Structures*, 44(20) :6517–6534.

[Griffith, 1921] Griffith, A. A. (1921). The phenomena of rupture and flow in solids. *Philosophical transactions of the royal society of london. Series A, containing papers of a mathematical or physical character*, pages 163–198.

[Haynes, 1978] Haynes, F. D. (1978). Effect of temperature on the strength of snow-ice. Technical report, DTIC Document.

[Hopkinson, 1914] Hopkinson, B. (1914). A method of measuring the pressure produced in the detonation of high explosives or by the impact of bullets. *Philosophical Transactions of the Royal Society of London. Series A, Containing Papers of a Mathematical or Physical Character*, pages 437–456.

[Inglis, 1913] Inglis, C. E. (1913). Stresses in a plate due to the presence of cracks and sharp corners. *Trans. Inst. Naval Architects*, 55 :219–230.

[Irwin, 1948] Irwin, G. R. (1948). Fracture dynamics. *Fracturing of metals*, 152.

[Irwin, 1957] Irwin, G. R. (1957). Analysis of stresses and strains near the end of a crack traversing a plate. *J. App. Mech*, 24 :361–364.

[Johnson, 2006] Johnson, S. (2006). *Stephen Johnson on digital photography*. O'Reilly Media, Inc.

[Karimzada and Maigre, 2000] Karimzada, T. and Maigre, H. (2000). Modelisation of dynamic crack propagation criteria. *Le Journal de Physique IV*, 10 :Pr9–461.

[Kim and Keune, 2007] Kim, H. and Keune, J. N. (2007). Compressive strength of ice at impact strain rates. *Journal of materials science*, 42(8) :2802–2806.

[Kolsky, 1949] Kolsky, H. (1949). An investigation of the mechanical properties of materials at very high rates of loading. *Proceedings of the Physical Society. Section B*, 62(11) :676.

[Kostrov, 1966] Kostrov, B. (1966). Unsteady propagation of longitudinal shear cracks. *Journal of applied Mathematics and Mechanics*, 30(6) :1241–1248.

[Krysl and Belytschko, 1999] Krysl, P. and Belytschko, T. (1999). The element free galerkin method for dynamic propagation of arbitrary 3-d cracks. *International Journal for Numerical Methods in Engineering*, 44(6) :767–800.

[Lange and Ahrens, 1982] Lange, M. A. and Ahrens, T. J. (1982). Fragmentation of ice by low velocity impact. In *Lunar and Planetary Science Conference Proceedings*, volume 12, pages 1667–1687.

[Liu, 2005] Liu, A. F. (2005). *Mechanics and mechanisms of fracture : an introduction*. ASM International.

[Liu and Miller, 1979] Liu, H. and Miller, K. (1979). Fracture toughness of fresh-water ice. *Journal of Glaciology*, 22 :135–143.

[Lu et al., 1995] Lu, Y., Belytschko, T., and Tabbara, M. (1995). Element-free galerkin method for wave propagation and dynamic fracture. *Computer Methods in Applied Mechanics and Engineering*, 126(1) :131–153.

[Melis et al., 2009] Melis, M. E., Revilock, D. M., Pereira, M. J., and Lyle, K. H. (2009). Impact testing on reinforced carbon-carbon flat panels with ice projectiles for the space shuttle return to flight program.

[Menouillard et al., 2006] Menouillard, T., Rethore, J., Combescure, A., and Bung, H. (2006). Efficient explicit time stepping for the extended finite element method (x-fem). *International Journal for Numerical Methods in Engineering*, 68(9) :911–939.

[Meyers and Chawla, 2009] Meyers, M. A. and Chawla, K. K. (2009). *Mechanical behavior of materials*, volume 2. Cambridge university press Cambridge.

[Moës et al., 1999] Moës, N., Dolbow, J., and Belytschko, T. (1999). A finite element method for crack growth without remeshing. *International Journal for Numerical Methods in Engineering*, 46(1) :131–150.

[Moës et al., 2002] Moës, N., Gravouil, A., and Belytschko, T. (2002). Non-planar 3d crack growth by the extended finite element and level sets-part i : Mechanical model. *International Journal for Numerical Methods in Engineering*, 53(11) :2549–2568.

[Mott, 1948] Mott, N. F. (1948). Brittle fracture in mild steel plates. *Engineering*, 165 :16–18.

[Nishioka et al., 2001] Nishioka, T., Tokudome, H., and Kinoshita, M. (2001). Dynamic fracture-path prediction in impact fracture phenomena using moving finite element method based on delaunay automatic mesh generation. *International Journal of Solids and Structures*, 38(30) :5273–5301.

[Nixon and Schulson, 1988] Nixon, W. A. and Schulson, E. (1988). The fracture toughness of ice over a range of grain sizes. *Journal of Offshore Mechanics and Arctic Engineering*, 110(2) :192–196.

[Orowan, 1949] Orowan, E. (1949). Fracture and strength of solids. *Rep. Prog. Phys*, 12 :185–232.

[Ortiz et al., 2015] Ortiz, R., Deletombe, E., and Chuzel-Marmot, Y. (2015). Assessment of damage model and strain rate effects on the fragile stress/strain response of ice material. *International Journal of Impact Engineering*, 76 :126–138.

[Osher and Sethian, 1988] Osher, S. and Sethian, J. A. (1988). Fronts propagating with curvature-dependent speed : algorithms based on hamilton-jacobi formulations. *Journal of computational physics*, 79(1) :12–49.

[Pan et al., 2009] Pan, B., Qian, K., Xie, H., and Asundi, A. (2009). Two-dimensional digital image correlation for in-plane displacement and strain measurement : a review. *Measurement science and technology*, 20(6) :062001.

[Pereira et al., 2006] Pereira, J. M., Padula, S. A., Revilock, D. M., and Melis, M. E. (2006). Forces generated by high velocity impact of ice on a rigid structure.

[Peters and Ranson, 1982] Peters, W. and Ranson, W. (1982). Digital imaging techniques in experimental stress analysis. *Optical engineering*, 21(3) :213427–213427.

[Petrenko and Gluschenkov, 1996] Petrenko, V. F. and Gluschenkov, O. (1996). Crack velocities in freshwater and saline ice. *Journal of Geophysical Research : Solid Earth*, 101(B5) :11541–11551.

[Petrovic, 2003] Petrovic, J. (2003). Review mechanical properties of ice and snow. *Journal of materials science*, 38(1) :1–6.

[Pommier et al., 2013] Pommier, S., Gravouil, A., Moes, N., and Combescure, A. (2013). *Extended finite element method for crack propagation*. John Wiley & Sons.

[Raju and Shivakumar, 1990] Raju, I. and Shivakumar, K. (1990). An equivalent domain integral method in the two-dimensional analysis of mixed mode crack problems. *Engineering Fracture Mechanics*, 37(4) :707–725.

[Ravi-Chandar, 2004a] Ravi-Chandar, K. (2004a). *Dynamic fracture*. Elsevier.

[Ravi-Chandar, 2004b] Ravi-Chandar, K. (2004b). *Dynamic fracture*. Elsevier.

[Reddy et al., 1991] Reddy, E., Abumeri, G., Chamis, C. C., and Murthy, P. (1991). Analysis of aircraft engine blade subject to ice impact.

[Rethore et al., 2004] Rethore, J., Gravouil, A., and Combescure, A. (2004). A stable numerical scheme for the finite element simulation of dynamic crack propagation with remeshing. *Computer methods in applied mechanics and engineering*, 193(42) :4493–4510.

[Réthoré et al., 2005] Réthoré, J., Gravouil, A., and Combescure, A. (2005). An energy-conserving scheme for dynamic crack growth using the extended finite element method. *International Journal for Numerical Methods in Engineering*, 63 :631–659.

[Rice, 1968] Rice, J. R. (1968). A path independent integral and the approximate analysis of strain concentration by notches and cracks. *Journal of applied mechanics*, 35(2) :379–386.

[Roux et al., 2009] Roux, S., Réthoré, J., and Hild, F. (2009). Digital image correlation and fracture : an advanced technique for estimating stress intensity factors of 2d and 3d cracks. *Journal of Physics D : Applied Physics*, 42(21) :214004.

[Schulson et al., 1989] Schulson, E., Baker, I., Robertson, C., Bolon, R., and Harnimon, R. (1989). Fractography of ice. *Journal of materials science letters*, 8(10) :1193–1194.

[Schulson, 1999] Schulson, E. M. (1999). The structure and mechanical behavior of ice. *Journal of the Minerals, Metals and Materials Society*, 51 :21–27.

[Schulson, 2001] Schulson, E. M. (2001). Brittle failure of ice. *Engineering Fracture Mechanics*, 68(17) :1839–1887.

[Schulson et al., 1984] Schulson, E. M., Lim, P., and Lee, R. (1984). A brittle to ductile transition in ice under tension. *Philosophical Magazine A*, 49(3) :353–363.

[Shazly et al., 2009] Shazly, M., Prakash, V., and Lerch, B. A. (2009). High strain-rate behavior of ice under uniaxial compression. *International Journal of Solids and Structures*, 46(6) :1499–1515.

[Standard et al., 2004] Standard, A. et al. (2004). Annual book of astm standards. *American Society for Testing and Materials Annual, Philadelphia, PA, USA*, 4(04.08).

[Stolarska et al., 2001] Stolarska, M., Chopp, D., Moes, N., and Belytschko, T. (2001). Modelling crack growth by level sets in the extended finite element method. *Int. J. Numer. Meth. Engng*, 51 :943–960.

[Swenson and Ingraffea, 1988] Swenson, D. and Ingraffea, A. (1988). Modeling mixed-mode dynamic crack propagation nsing finite elements : theory and applications. *Computational Mechanics*, 3(6) :381–397.

[Tippmann et al., 2013] Tippmann, J. D., Kim, H., and Rhymer, J. D. (2013). Experimentally validated strain rate dependent material model for spherical ice impact simulation. *International Journal of Impact Engineering*, 57 :43–54.

[Wells, 1965] Wells, A. (1965). The application of fracture mechanics to yielding materials. In *Proceedings of the Royal Society of London A : Mathematical, Physical and Engineering Sciences*, volume 285, pages 34–45. The Royal Society.

[Westergaard, 1939] Westergaard, H. (1939). Bearing pressures and crack. *Journal of applied mechanics*.

[Wu and Prakash, 2015] Wu, X. and Prakash, V. (2015). Dynamic compressive behavior of ice at cryogenic temperatures. *Cold Regions Science and Technology*, 118 :1–13.

[Yoffe, 1951] Yoffe, E. (1951). The moving griffith crack. *Phil. Mag.*, 42 :739–751.

[Zhao, 2003] Zhao, H. (2003). Material behaviour characterisation using shpb techniques, tests and simulations. *Computers & structures*, 81(12) :1301–1310.

UNIVERSITÉ DE LYON

INSA INSTITUT NATIONAL DES SCIENCES APPLIQUÉES LYON

FOLIO ADMINISTRATIF

THESE DE L'UNIVERSITE DE LYON OPEREE AU SEIN DE L'INSA LYON

NOM : YAO DATE de SOUTENANCE : le 3 Mai 2016

Prénoms : Lan

TITRE : Experimental and Numerical Study of Dynamic Crack Propagation in Ice under Impact loading

NATURE : Doctorat Numéro d'ordre : 2016LYSEI043

Ecole doctorale : MECANIQUE, ENERGETIQUE, GENIE CIVIL, ACOUSTIQUE

Spécialité : Mécanique -Génie Mécanique - Génie Civil

RESUME :

The phenomena relating to the fracture behaviour of ice under impact loading are common in civil engineering, for offshore structures, and de-ice processes. To reduce the damage caused by ice impact and to optimize the design of structures or machines, the investigation on the dynamic fracture behaviour of ice under impact loading is needed.

This work focuses on the dynamic crack propagation in ice under impact loading. A series of impact experiments is conducted with the Split Hopkinson Pressure Bar. The temperature is controlled by a cooling chamber. The dynamic process of the ice fracture is recorded with a high speed camera and then analysed by image methods. The extended finite element method is complementary to evaluate dynamic fracture toughness at the onset and during the propagation.

The dynamic behaviour of ice under impact loading is firstly investigated with cylindrical specimen in order to obtain the dynamic stress-strain relation which will be used in later simulation.

We observed multiple cracks in the experiments on the cylindrical specimens but their study is too complicated. To better understand the crack propagation in ice, a rectangular specimen with a pre-crack is employed. By controlling the impact velocity, the specimen fractures with a main crack starting from the pre-crack. The crack propagation history and velocity are evaluated by image analysis based on grey-scale and digital image correlation. The main crack propagation velocity is identified in the range of 534±83m/s which confirms the previous results. It slightly varies during the propagation, first increases and keeps constant and then decreases.

The experimentally obtained parameters, such as impact velocity and crack propagation velocity, are used for simulations with the extended finite element method. The dynamic crack initiation toughness and dynamic crack growth toughness are determined when the simulation fits the experiments. The results indicate that the dynamic crack growth toughness is linearly associated with crack propagation velocity and seems temperature independent in the range -15 -1 °C.

MOTS-CLÉS: crack propagation, dynamic stress intensity factor, ice, split Hopkinson pressure bar, extended finite element method

Laboratoire (s) de recherche :

Directeur de thèse:	NELIAS Daniel	Professeur des Universités	INSA LYON	Directeur de thèse
	MAIGRE Hubert	Chargé de recherche	CNRS	Co-directeur de thèse

Président de jury :

Composition du jury :

NELIAS Daniel	Professeur des Universités	INSA LYON	Directeur de thèse
MAIGRE Hubert	Chargé de recherche	CNRS	Examinateur
ZHAO Han	Professeur des Universités	LMT	Rapporteur
MONTAGNAT Maurine	Chargé de recherche	CNRS	Rapporteur
DELETOMBE Eric	Maître de Recherche	ONERA	Examinateur
COMBESCURE Alain	Professeur des Universités	INSA LYON	Président